

**UNIVERSIDADE DE SÃO PAULO**  
**INSTITUTO DE QUÍMICA**  
Graduate Program in Chemistry

**EDUARDO CESAR MELO BARBOSA**

**Noble metal nanoparticles supported onto semiconducting  
oxides as catalysts for reduction reactions**

**Corrected version of the submitted thesis**  
**Versão corrigida da tese depositada**

São Paulo  
Date of submission to SPG:  
**05/09/2019**

EDUARDO CESAR MELO BARBOSA

**Nanopartículas de metais nobres suportadas em óxidos  
semicondutores como catalisadores para reações de  
redução**

*Tese apresentada ao Instituto de Química da  
Universidade de São Paulo para obtenção do  
Título de Doutor em Ciências (Química)*

*Orientador: Prof. Dr. Pedro Henrique Cury Camargo*

São Paulo  
2019

Autorizo a reprodução e divulgação total ou parcial deste trabalho, por qualquer meio convencional ou eletrônico, para fins de estudo e pesquisa, desde que citada a fonte.

Ficha Catalográfica elaborada eletronicamente pelo autor, utilizando o programa desenvolvido pela Seção Técnica de Informática do ICMC/USP e adaptado para a Divisão de Biblioteca e Documentação do Conjunto das Químicas da USP

Bibliotecária responsável pela orientação de catalogação da publicação:  
Marlene Aparecida Vieira - CRB - 8/5562

B238n      Barbosa, Eduardo Cesar Melo Barbosa  
             Nanopartículas de metais nobres suportadas em  
             óxidos semicondutores como catalisadores para reações  
             de redução / Eduardo Cesar Melo Barbosa Barbosa. -  
             São Paulo, 2019.  
             152 p.

Tese (doutorado) - Instituto de Química da  
Universidade de São Paulo. Departamento de Química  
Fundamental.  
Orientador: Camargo, Pedro Henrique Cury Camargo

1. Catálise. 2. Plasmônica. 3. Fotocatálise. 4.  
Semicondutores. 5. Eletrocatalise. I. T. II.  
Camargo, Pedro Henrique Cury Camargo, orientador.



***Dedication***

To those who believed and supported me throughout my career, especially my family.

## **Acknowledgments**

First and foremost, I would like to thank my parents, Suely and João, and my brother, Daniel for the support and for being by my side throughout my entire life, always backing me up through every step and celebrating every achievement on my career.

I would also like to thank my closest friends, with whom I continued to develop a friendship through these years of my Ph.D., to Allan, Bruna, Bruno, Fernando, Jessica Scremin, Jéssica Serafim, Neuza, Pâmela Marcela, Renan, Vanessa, and Yasmin, you made this period a lot easier by being by my side.

I want to thank Jhonatan Fiorio for his help, his patience, all the knowledge he shared with me during this period, and especially the friendship we developed through the years.

I thank my friends from the lab in Brazil, in special Eduardo Carmine, Fabiane, Isabel, Jhon, Letizia, Liliam, Luanna, Marcos, Maria, Paulo, Rafael Trivella, Thaylan, and Vitor for all the good times and all the knowledge shared. I would also like to thank all the undergraduate students that I had the opportunity of working with, Bárbara, Isabella, Livia, Luis, and Vitor. This was an experience that I will not forget.

I want to thank all our collaborators for being in direct contact with us and helping us achieve so many great scientific discoveries, not only on my projects but also on projects that I was involved through the group.

I thank professor Dr. Pedro Camargo for the entire experience as a professional, for the opportunities he gave me and all the knowledge he shared. For all the weekends spent working together or even the late-night e-mails sharing results. For all the times we sat on his office discussing results or also writing up a paper which we were sure would be the next big thing. Thank you for teaching what research is about and for making me see how it should be done.

I thank the Tsang group from the University of Oxford, especially the members that worked closely with me, Iris, Ivo, Jianwei, Tianyi, and Tuğçe, thank you for all the good times and knowledge shared, you sure helped me a lot. I would also like to thank my other colleagues from the group, which made my time in the lab more enjoyable - Bruce, Kirsty, Josh, Tim, and William.

I thank Professor Edman Tsang for the great opportunity of working with him during my time in Oxford. It was a gratifying time. I will never forget the meetings in his office where he would explain to me in a very detailed manner about several procedures and techniques, aside from all the knowledge shared about the literature. The passion that he showed towards his job always motivated me to achieve more.

I would like to thank Pablo Gonzalez Martin for the support and constant help through the writing process, the countless hours spent in the library, the numerous coffees to keep us from sleeping, not to mention the friendship, the partnership and all the great moments we spent together which undoubtedly helped a lot this past year.

Last but not least, I would like to thank my Oxford friends, in special Bárbara, Darlene, Natalia, and Vinícius, thank you for all the good times during my time in Oxford, for all the support and laughter, you helped me get through tough times and celebrate good ones, thank you.

I want to thank FAPESP for granting me a research grant in Brazil (#2015/11452-5) and in the United Kingdom (#2018/00393-6). I will always be grateful for the opportunities that this foundation gave me.

“The only true wisdom is in  
knowing you know nothing.”

*Socrates*



## RESUMO

Barbosa, E.C.M. **Nanopartículas de metais nobres suportadas em óxidos semicondutores como catalisadores para reações de redução**. 2019. 152p. Tese - Programa de Pós-Graduação em Química. Instituto de Química, Universidade de São Paulo, São Paulo.

Esta tese tem como objetivo principal contribuir para o campo da catálise empregando nanomateriais compostos de  $\text{TiO}_2$ ,  $\text{Au/TiO}_2$ ,  $\text{SiO}_2$ ,  $\text{Au/SiO}_2$ ,  $\text{Pt/TiO}_2$ ,  $\text{Fe}_2\text{O}_3$  e  $\text{Pd/Fe}_2\text{O}_3$  para reações de redução. Primeiramente,  $\text{Au/TiO}_2$  e  $\text{Au/SiO}_2$  foram explorados como catalisadores para a hidrogenação do 4-nitrofenol sob excitação plasmônica, enquanto a fonte de hidrogênio foi variada entre  $\text{H}_{2(\text{g})}$  e  $\text{BH}_{4-\text{(aq)}}$ . Essas mudanças levaram a diferentes vias de reação e descobrimos que a excitação plasmônica do Au pode levar a efeitos negativos sob algumas condições. A razão física por trás desse fenômeno foi explorada empregando-se cálculos de teoria funcional da densidade (DFT). Observamos que efeitos positivos também ocorrem na atividade catalítica plasmônica dependendo da via de reação. Esses resultados trazem informações importantes sobre nossa compreensão atual da catálise plasmônica, demonstrando-se que as vias de reação devem ser levadas em consideração para a projeção de nanocatalisadores plasmônicos. As amostras de  $\text{TiO}_2$  foram então empregadas como modelos para a deposição de nanopartículas de Pt com diferentes cargas metálica. Posteriormente, esses materiais foram suportados em carbono para a redução eletrocatalítica de oxigênio. Ao otimizar a carga de Pt na superfície do  $\text{TiO}_2$ , a atividade eletrocatalítica foi melhorada em comparação com o material comercial de Pt/C, mesmo em cargas de Pt mais baixas. A melhora nas atividades eletrocatalíticas dos materiais pode ser atribuída ao equilíbrio entre a carga de Pt e a geração de sítios reativos na superfície, como espécies oxigenadas adsorvidas. Além disso, a utilização do  $\text{TiO}_2$  como suporte permitiu melhores estabilidades em relação ao Pt/C comercial. Esses resultados podem inspirar o desenvolvimento de eletrocatalisadores para a reação de redução de oxigênio com atividades e estabilidade aprimoradas. Por fim, nanomateriais compostos de nanopartículas de Pd suportadas em óxido de ferro foram empregados como catalisadores na redução do óxido de estireno. Investigamos os efeitos de um agente de capeamento na atividade e seletividade do catalisador. Observou-se que a remoção do estabilizador polimérico nos permitiu obter uma seletividade invertida e uma

atividade mais alta do material. Isso nos dá uma visão diferente sobre o papel de um estabilizador na nanocatálise e abre a possibilidade de adaptar a seletividade. Acreditamos que os resultados aqui apresentados mostram informações importantes sobre nosso entendimento da nanocatálise por nanopartículas metálicas controladas.

**Palavras-chave:** Catálise, Plasmônica, Fotocatálise, Semicondutores, Eletrocatalise, Nanopartículas.

## ABSTRACT

Barbosa, E.C.M. **Noble metal nanoparticles supported onto semiconducting oxides as catalysts for reduction reactions.** 2019. 152p. Ph.D. Thesis - Graduate Program in Chemistry. Instituto de Química, Universidade de São Paulo, São Paulo.

This thesis has as main objective to contribute to the field of catalysis employing nanomaterials composed of  $\text{TiO}_2$ ,  $\text{Au/TiO}_2$ ,  $\text{SiO}_2$ ,  $\text{Au/SiO}_2$ ,  $\text{Pt/TiO}_2$ ,  $\text{Fe}_2\text{O}_3$ , and  $\text{Pd/Fe}_2\text{O}_3$  towards reduction reactions. Firstly,  $\text{Au/TiO}_2$  and  $\text{Au/SiO}_2$  were explored as catalysts for the hydrogenation of 4-nitrophenol under plasmonic excitation, while the hydrogen source was varied between  $\text{H}_{2(\text{g})}$  and  $\text{BH}_{4-\text{(aq)}}$ . These changes led to different reaction pathways, and we found that the plasmonic excitation of Au can lead to negative effects over the activities under some conditions. The underlying physical reason was explored using density functional theory calculations. We observed that positive versus negative effects on the plasmonic catalytic activity is reaction-pathway dependent. These results shed important insights on our current understanding of plasmonic catalysis, demonstrating reaction pathways must be taken into account for the design of plasmonic nanocatalysts. The  $\text{TiO}_2$  samples were then employed as templates for the deposition of Pt nanoparticles with different loadings. Subsequently, these materials were supported onto carbon for the electrocatalytic reduction of oxygen. By optimizing the loading of Pt at the  $\text{TiO}_2$  surface, the electrocatalytic activity towards the activity of them could be improved compared to the commercial Pt/C material, even at lower Pt loadings. The enhancement in activities could be assigned to the balance between Pt loading and generation of reactive surface sites, such as adsorbed oxygenated species. Moreover, the utilization of  $\text{TiO}_2$  as support enabled improved stabilities relative to commercial Pt/C. These results may inspire the development of electrocatalysts for the oxygen reduction reaction with improved activities and stabilities. Lastly, nanomaterials composed of Pd nanoparticles supported onto iron oxide were employed as catalysts on the reduction of styrene oxide. We investigated the effects of a capping agent onto the activity and selectivity of the catalyst. It was observed that the removal of the polymeric stabilizer enabled us to achieve an inverted selectivity and a higher activity of the material. This gives us a different view of the role of a stabilizer in nanocatalysis and opens up the possibility of

tailoring the selectivity. We believe that the results presented herein shed important insights into our understanding of nanocatalysis by controlled metal nanoparticles.

**Keywords:** Catalysis, Plasmonics, Photocatalysis, Semiconductors, Electrocatalysis, Nanoparticles.

## SUMMARY

Section 1 – General Introduction .....	14
Chapter 1 – Nanomaterials for catalytic applications.....	15
1.1 – Motivation .....	15
1.2 – Metallic Nanomaterials.....	15
1.3 – Catalytic properties: applications in nanocatalysis.....	17
1.4 – Optical properties: applications in plasmonic nanocatalysis .....	19
1.5 – Metallic nanoparticles supported onto semiconducting oxides .....	23
1.6 – Metallic nanoparticles as catalysts for reduction reactions .....	26
1.6.1 – Hydrogenation reactions.....	26
1.6.2 – Oxygen reduction reaction.....	29
1.7 – References .....	31
Chapter 2 – Nanomaterials for catalytic applications.....	42
2.1 – General objectives .....	42
2.2 – Specific goals.....	42
Section 2 – Metallic nanoparticles supported on semiconductor oxides towards reduction reactions.....	43
Chapter 3 – Gold nanospheres supported on Titania: The dark side of photocatalytic hydrogenations.....	44
3.1 – Introduction .....	44
3.2 – Experimental Section.....	47
3.3 – Results and Discussion .....	53
3.4 – Conclusions .....	71
3.5 – References .....	72
Chapter 4 – Platinum nanoparticles supported on Titania: An improved electrocatalyst towards the oxygen reduction reaction .....	44
4.1 – Introduction .....	80
4.2 – Experimental Section.....	82
4.3 – Results and Discussion .....	87
4.4 – Conclusions .....	106
4.5 – References .....	107
Chapter 5 – Shape controlled Pd/Fe <sub>2</sub> O <sub>3</sub> towards the selective hydrogenation of styrene epoxide.....	80
5.1 – Introduction .....	114
5.2 – Experimental Section.....	116
5.3 – Results and Discussion .....	120
5.4 – Conclusions .....	136

5.5 – References .....	137
Section 3 – Conclusions and perspectives .....	141
Chapter 6 – Final remarks .....	142
Academic curriculum vitae.....	144

## **Section 1 – General Introduction**

## Chapter 1 – Nanomaterials for catalytic applications

### 1.1 – Motivation

Significant economic investment has been put into researching materials for their catalytic properties.<sup>1</sup> The search for compounds that can provide a better yield or enhance benchmark catalysts is of great importance for various fields, such as the chemical and pharmaceutical industry, green energy production, environmentally friendly chemistry, and of course, science itself.<sup>2</sup> Since catalysis has been present in our daily lives for years, the generation of chemicals and materials via catalysis has played a central role for our astonishing society development.<sup>3</sup>

Several classes of materials can be employed as catalysts, from enzymes to single-atoms.<sup>4–6</sup> Each catalyst has its advantages and disadvantages, which leads to a large number of combinations and thus many different ways of producing certain chemicals. In this chapter, we aim at exploring the use of nanomaterials as catalysts. We will discuss and exploit their properties along with their applications targeting catalytic reduction reactions.

### 1.2 – Metallic Nanomaterials

The basic definition of a nanomaterial dictates that they attain, at least in one of their dimensions, sizes between 1 and 100 nm.<sup>7</sup> These materials are typically employed due to their vast array of properties that differ from their bulk analogs.<sup>8–11</sup> One of their critical features is their increased surface area that is observed when going from the bulk to the nanoscale. **Figure 1.1** displays a graphical example of a sphere of 1 mm being divided into smaller spheres which add up to the same volume, displaying an area enhancement of one million folds the initial value.



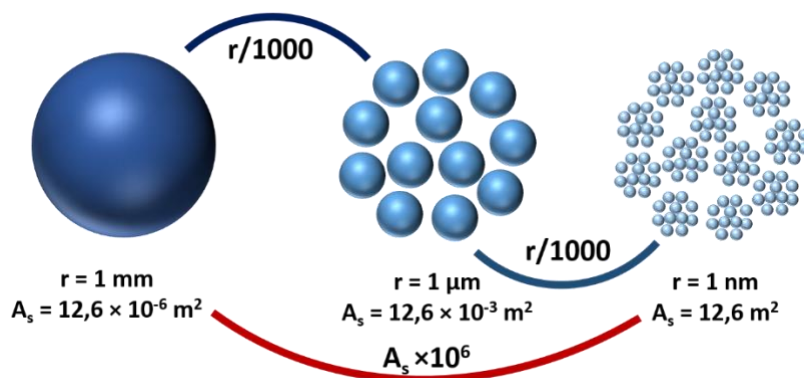


**Figure 1.1** – Graphical example of a sphere having a 1 mm radius being divided into nanospheres with 1 nm of radius. This leads to an increase in surface area corresponding to 1 million folds.

This drastically changes optical, magnetic, electronic, and catalytic properties, among others.<sup>12</sup> Due to this features, nanomaterials have been applied in many fields, including photothermal therapies,<sup>13</sup> in which nanomaterials can be activated with the use of light, drug delivery systems,<sup>14</sup> sensors,<sup>15</sup> and catalysis,<sup>16</sup> a field that harvests benefits not only from the nanomaterials sizes, but their shapes, crystalline defects, and surface interactions.

Among several classes of nanomaterials, metals deserve special attention and represent the focus of our work. Metals make up more than two-thirds of the periodic table,<sup>17</sup> and by minimizing their sizes it has been found that new properties arise, such as their optical properties and new reactivity towards several reactions.<sup>18</sup> Moreover, they display unique magnetic and electronic properties.<sup>14,19</sup> As several of their properties are dependent and therefore tunable relative to their physical and chemical features that include size, shape, and structure, the controlled synthesis of metallic nanomaterials in which these parameters can be controlled becomes of fundamental importance for the optimization of properties and the understanding of performances.<sup>20–24</sup> Achieving fine control over a nanomaterial size, shape, composition, and architecture (hollow vs. solid interiors) can be a time consuming and meticulous job, due to all the factors that could impact on its final structure and the numerous variables on which they depend.<sup>25</sup> Designing materials for the target application has been, for

a few years, the goal of many research groups. To achieve such objective, systematic studies must be performed by relating sizes, surface properties, optical properties, or even interaction between nanoparticles and supports to establish structure performance relationships.<sup>17</sup> This is, for example, fundamental for applications in nanocatalysis.

It has been established that the exposure of different surface facets in TiO<sub>2</sub> (which can be achieved via shape control) strongly influences its performance towards the photocatalytic hydrogenation of CO<sub>2</sub>.<sup>26</sup> While the {001} facet has a better activity for the CO<sub>2</sub> photocatalytic reduction to CH<sub>4</sub>, the equilibrium between {001} and {101} facets showed a higher activity due to the lower exciton recombination rates. On the other hand it is also known that semiconducting materials displaying different shapes have distinct band-gap energies and surface energies, thus changing the interaction with substrate molecules and influencing catalytic performance.<sup>27–30</sup>

### 1.3 – Catalytic properties: applications in nanocatalysis

From all the applications of metallic nanomaterials, catalysis deserves special attention as it plays a central role towards a sustainable future. Catalysis enables the use of greener reaction conditions, improved efficiencies, less energy consumption, and less generation of byproducts. It plays a central role in the production of chemical and pharmaceuticals. As over 85% of all substances produced today involve the use of catalysis, improvements in catalytic processes can lead to significant economic and environmental impacts.

Catalysis is a method of accelerating a chemical reaction through the addition of a substance which is not consumed during the process (catalyst). These substances act on reactions by providing different pathways and mechanisms by which reactants can lead to the formation of the products relative to the reaction without the catalyst, as shown in **Figure 1.2**.<sup>31–33</sup> Taking into account that the final product is the same in both cases, the Gibbs energy

involved in the reactions must be the same. Therefore, the critical factor is that the activation energy changes from one example to the other.<sup>32</sup>

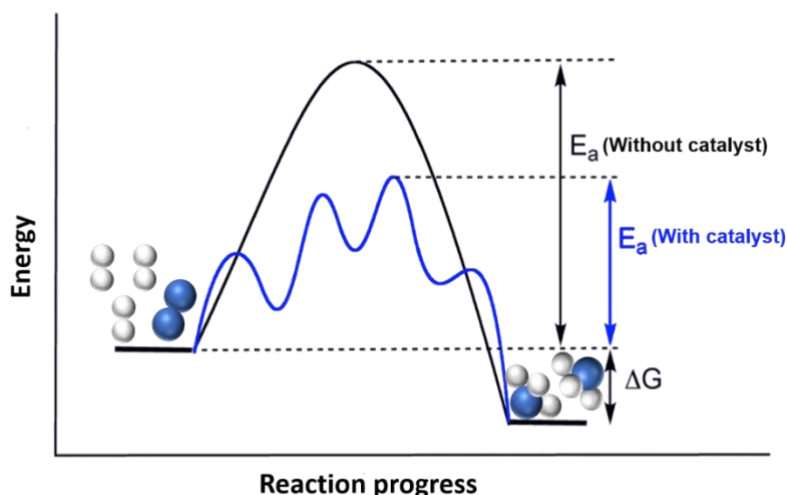


**Figure 1.2** – Progress diagram of two reactions happening in the presence of a catalyst (blue line) and in the absence of a catalyst (black line). The activation energy for the catalyzed reaction is lower than for the non-catalyzed one due to the new pathways that a catalyst can provide for the molecules to react.

Two of the main classes of catalysts are the homogeneous catalysts, which are substances that are in the same phase as the reactants, and the heterogeneous catalysts, substances in different phases from the reactants. While homogeneous catalysts are more miscible with the substrates, they are also of difficult separation/recycling. On the other hand, heterogeneous catalysts are less miscible with the substrates and due to this, they are easily separable and recyclable.<sup>32</sup> Heterogeneous catalysis accounts for about 80% of the chemical processes inside the industry, a number that clearly shows the importance of studying and understanding catalysts to an economic point of view.<sup>34</sup> Catalysts are generally evaluated on their activity, which is the percentage of reactants converted into products, on their selectivity, which is the percentage of product that is the desired compound, and their reusability.<sup>35</sup> Metallic NPs have played a central role in nanocatalysis. These materials, typically supported

in high surface area supports, act as the catalytic center and provide a specific activity and selectivity depending on their surface area, surface defects, and nature of surface facets.<sup>3</sup>

#### 1.4 – Optical properties: applications in plasmonic nanocatalysis

The fast-ongoing development of nanoscience is mostly attributed to the different properties that nanomaterials present from their bulk materials and single atoms. In this sense, metallic NPs are known to interact with light in a different manner than their bulk equivalents. Some metallic NPs, such as Au, display outstanding optical properties in the visible range as a result of their localized surface plasmon resonance (LSPR) excitation, which stands for the oscillation of free charges on the surface of a metallic nanoparticle.<sup>36</sup> **Figure 1.3** represents this phenomenon.<sup>37</sup>

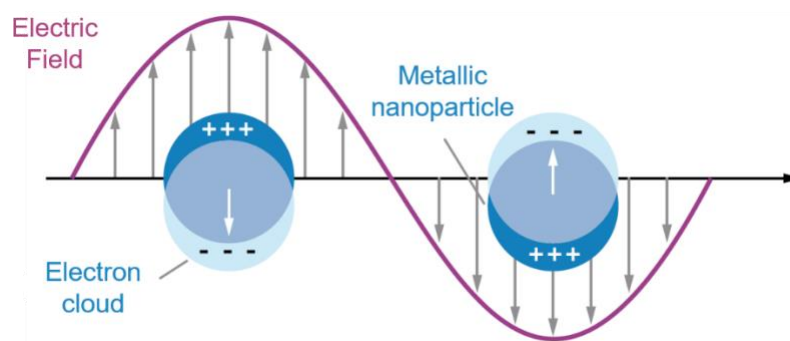


**Figure 1.3** – Graphical representation for the LSPR excitation.<sup>37</sup>

Upon electromagnetic irradiation, the oscillating electric field of light imposes a force onto the mobile electrons on the nanoparticle surface, which thus results in an induced dipole moment. To counterbalance this excitation, charge redistribution acts to provide a coulombic restoring force on the mobile electrons, consequently granting these NPs an associated resonant frequency at a specific wavelength for each material. The LSPR excitation depends on several parameters such as size, shape, composition, and dielectric constant of the

environment.<sup>38</sup> These concepts are exemplified in **Figure 1.4**. Which illustrates the effect of size, shape, composition over the extinction properties of NPs based on Ag, Au, and Cu.<sup>39</sup>

**Figure 1.4A** shows the influence of Ag nanocubes sizes onto the optical properties of these materials, as seen on the extinction spectra, the smallest cubes present their highest extinction band at around 450 nm, when their size increase, the extinction band is shifted to higher wavelengths. **Figure 1.4B** indicates the changes in optical properties of different shapes of silver nanomaterials, as seen, it is also possible to shift the extinction band onto different wavelengths through shape control.

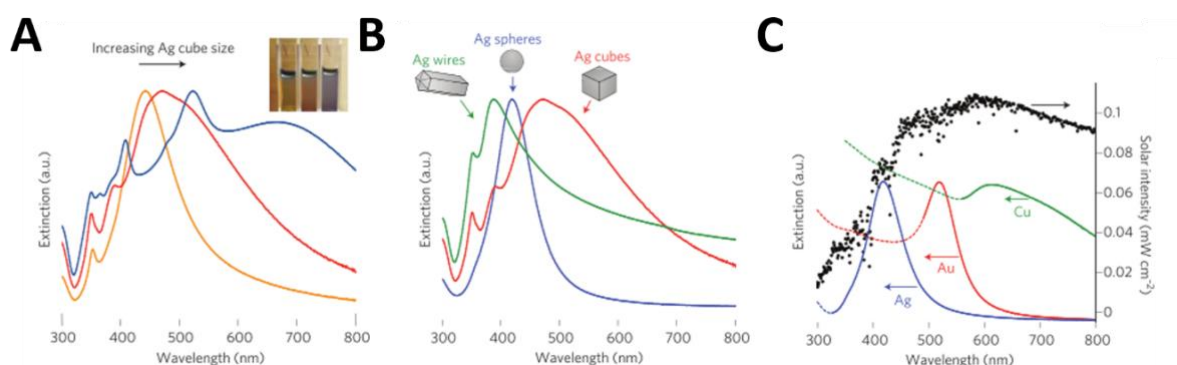


**Figure 1.4** – Different properties of plasmonic Ag NPs. (A) Extinction band changes alongside with nanocube sizes. (B) Changes in the extinction spectra of silver along with shape. (C) Extinction spectra of sub-100-nm Ag, Au and Cu NPs in blue, red and green, respectively. The solar spectrum is plotted in black as a comparison.<sup>39</sup>

Recently, it has been shown that the LSPR excitation can also be out towards the enhancement of the rates of chemical reactions. This field has been coined plasmonic catalysis. Such field is based on employing metallic nanostructures and electromagnetic waves to enhance reaction rates or even tailor the selectivity.<sup>40</sup>

It has been reported that near-field enhancements, heat generation, and LSPR excited charge carriers can contribute to plasmonic catalysis (**Figure 1.5**).<sup>41</sup> Upon light incidence, electrons from the nanoparticle surface oscillate at the same frequency as the incoming

electric field. Since each material presents a different LSPR, this oscillation is further enhanced when the incident wave matches the nanoparticle LSPR wavelength.<sup>42</sup> The incoming light is then re-emitted by the nanoparticle both by far-field scattering or concentrating it on the metallic surface. The mechanisms to accelerate and enhance reaction rates are: the temperature increase on metallic NPs caused by light excitation can be responsible for many thermoactivated reactions, **Figure 1.5A**; near optical field enhancement, **Figure 1.5B**, which can increase the photon absorption in photo-sensitive reaction; and charge-transfer phenomena, when LSPR-excited hot electrons are transferred from the plasmonic nanoparticle to a molecular reactant adsorbed to the nanoparticle, **Figure 1.5C**.<sup>41</sup>

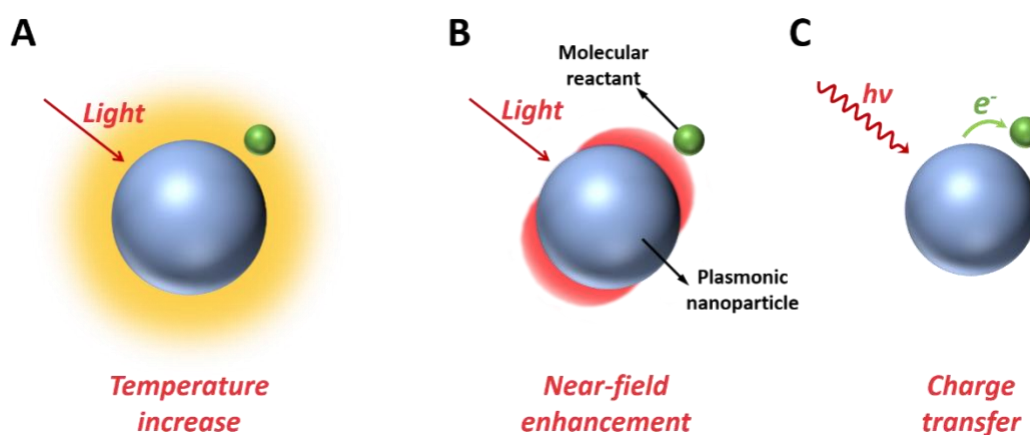


**Figure 1.5** – (A)-(C) Mechanisms originated from LSPR-excited NPs. (A) Following LSPR excitation, a temperature increase observed due to the Joule effect on the NPs. (B) Optical near-field enhancement caused by the electric dipole on the surface of the NPs. (C) Hot-electrons and holes generated via LSPR excitation and are thus transferred to nearby species.<sup>41</sup>

The events following LSPR excitation are also shown in **Figure 1.6**.<sup>43</sup> After absorbing a photon, **Figure 1.6A**, a surface electron of the metallic nanoparticle is excited to a higher energy level generating the so-called “hot electrons” and “hot holes”, **Figure 1.6B**. Such transition creates the probability of finding the excited electrons between the fermi level of

the nanoparticle ( $E_F$ ) and  $E_F + h\nu$ . After around 100 femtoseconds, these electrons lose energy via Landau Damping and through this energy redistribution are able to either migrate to adsorbed molecules or eject other electrons to them.

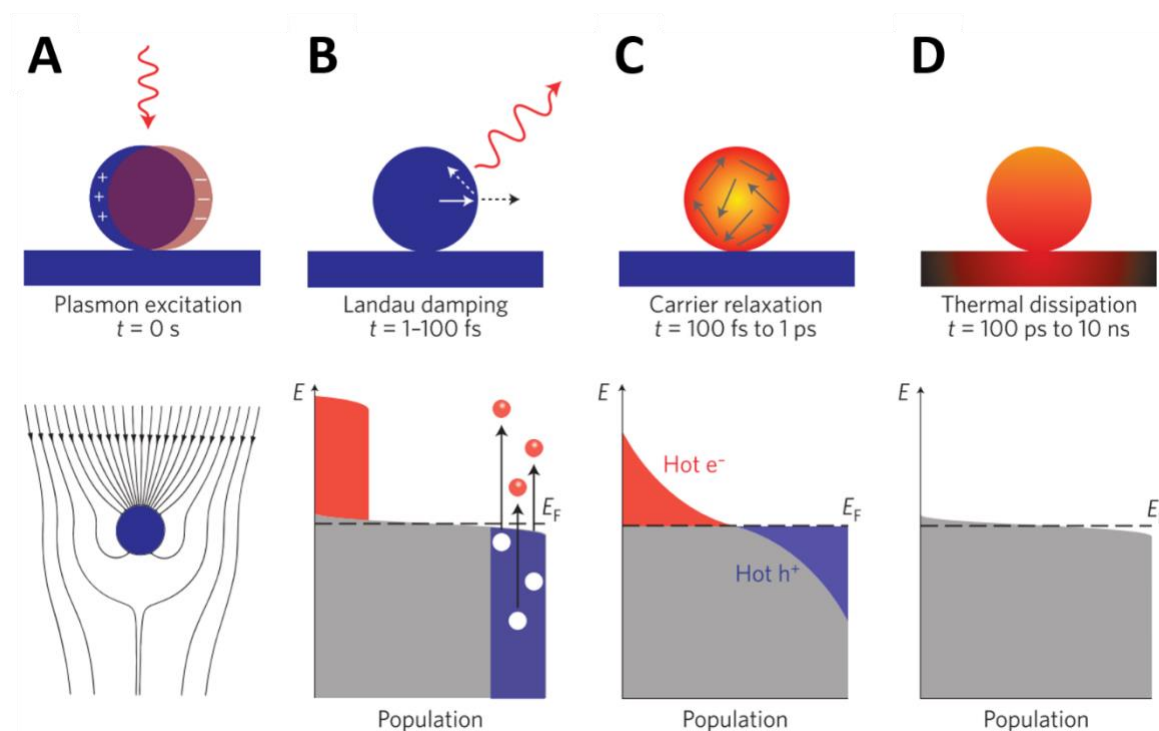


**Figure 1.6** – Photoexcitation and relaxation of metallic NPs. (A)–(D), Photoexcitation and subsequent relaxation processes following the illumination of a metal nanoparticle with a laser pulse, and characteristic timescales. (A) First, the excitation of a localized surface plasmon redirects the flow of light (Poynting vector) towards and into the nanoparticle. (B)–(D) Schematic representations of the population of the electronic states (grey) following plasmon excitation: hot electrons are represented by the red areas above the Fermi energy  $E_F$  and hot hole distributions are represented by the blue area below  $E_F$ . (B) In the first 1–100 fs following Landau damping, the athermal distribution of electron-hole pairs decays either through re-emission of photons or through carrier multiplication caused by electron-electron interactions. During this very short time interval, the hot carrier distribution is highly non-thermal. (C) The hot carriers will redistribute their energy by electron-electron scattering processes on a timescale ranging from 100 fs to 1 ps. (D) Finally, heat is transferred to the surroundings of the metallic structure on a longer timescale ranging from 100 ps to 10 ns, via thermal conduction. <sup>43</sup>

This effect could also occur by the direct population of the adsorbate electronic states through hot charge-carriers generated upon LSPR excitation. During this event, the entire system moves onto a different potential energy state, resulting in the activation of bonds and chemical reactions. These electrons will continuously redistribute their energy onto the metallic nanoparticle through electron-electron scattering for up to 1 ps, **Figure 1.6C**. A third effect from the LSPR is energy dissipation through the Joule effect, which states that when electrons flow through metal with a specific resistance, the heating power from this event is proportional to the product of its resistance and the square of the flowing current. This effect tends to produce local heating, hence increasing the NP temperature, **Figure 1.6D**. This property of plasmonic NPs has been widely used in nanomedicine, to treat cancer, gene, and drug delivery. It has also been employed on the development of photothermal motors using self-assembled Au NPs, under light incidence, these NPs are responsible for raising the local temperature, which thus generates water vapor that propels the material to the opposite side of the vapor current. Although the applications of this effect may seem limited on catalysis, these thermo-induced processes could also benefit many chemical reactions.<sup>44</sup> In this dissertation, we are interested in merging the catalytic and optical properties of Au NPs supported on semiconducting oxides to study how metal support interactions affect the catalytic performances with and without the LSPR excitation.

## **1.5 – Metallic nanoparticles supported onto semiconducting oxides**

Regarding application in catalysis, metallic NPs are usually supported onto other materials, such as oxides, to facilitate recovery, re-use, and improve catalyst stability.<sup>45,46</sup> Moreover, metal support interactions can lead to further enhancements in activity generating active sites at the metal-support interface or enabling charge transfer processes under light illumination, for example.<sup>9</sup>



There are several different ways of synthesizing hybrid metal/semiconductor nanomaterials, with both controlled and non-controlled shapes and sizes. Among the procedures, we can highlight semiconductor oxides decorated with plasmonic metal NPs, plasmonic metal core with a semiconductor shell nanostructure, Janus particles composed of plasmonic metal and oxide semiconductors, among others.<sup>47–49</sup> The synthesis of semiconductor oxides decorated with plasmonic metal NPs is usually performed by the anchoring or growth of metallic NPs on the surface of preformed semiconductor oxide.<sup>50,51</sup> Mainly three methods are employed for these syntheses, the first is by soaking the preformed oxide with a precursor solution followed by reduction with the desired reducing agent.<sup>52,53</sup> The second method is by performing the synthesis of NPs in the presence of the oxide, so the particles nucleate and grow on top of the support.<sup>54–56</sup> And the last method is the impregnation of preformed NPs onto the preformed oxide, both functionalized and not.<sup>57,58</sup> The core-shell synthesis usually employs preformed metallic nanostructures and grows the oxide onto their surface or vice-versa.<sup>59,60</sup> Their properties frequently change by varying the core shape, size, shell shape, and size.<sup>48</sup> The most explored combinations are TiO<sub>2</sub> and plasmonic metals due to the photocatalytic properties of this oxide.<sup>61,62</sup> Janus particles, on the other hand, require complex syntheses and fine control, since a complex morphology is needed to achieve the required functionality.<sup>63</sup> Au NPs are widely employed metallic nanostructures since they provide LSPR to the hybrid material. They are typically synthesized through separate growth, co-deposition or light-induced reduction. Generally, TiO<sub>2</sub>, ZnO, and magnetic iron oxides are used as semiconductors.<sup>64</sup>

Supporting metals on semiconductors can generate electron-transfer effects due to the electron structure of the atoms present on each material, which is directly related to their work function ( $\phi$ ).<sup>65</sup> A work function is the energy needed to pull an electron from the Fermi level to vacuum. When the metal work function ( $\phi_m$ ) is higher than the n-type semiconductor ( $\phi_s$ ),

as seen in **Figure 1.7A**, electrons will flow to the metal until both the metal Fermi level ( $E_{F,m}$ ) and semiconductor Fermi level ( $E_{F,s}$ ) are aligned. Thus, at the metal/semiconductor interface, a double layer is formed with negative charges on the metal surface and positive charges on the semiconductor. Hence, the semiconductor surface will be electron-deficient when compared to the bulk semiconductor, so, this surface layer of the n-type semiconductor is called the depletion layer. On the other hand, when  $\phi_m$  is lower than  $\phi_s$ , as seen in **Figure 1.7B**, electrons will flow from the metal to the semiconductor until  $E_{F,m}$  aligns with  $E_{F,s}$ . This generates an electron filled layer at the surface of the semiconductor, called the accumulation layer. Electrons usually flow from the material with a higher work function and thus lower their Fermi energy level.

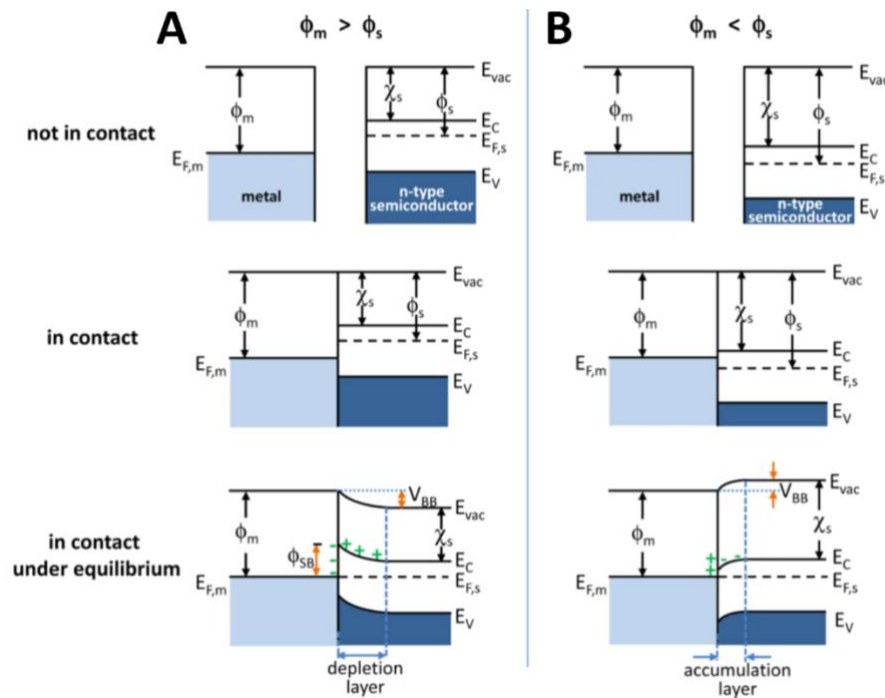


**Figure 1.7** – Band-bending effect on a metallic nanoparticle (light blue) attached to an n-type semiconductor (dark blue), (A) when the semiconductor work function ( $\phi_s$ ) is higher than the metal work function ( $\phi_m$ ), and (B) when the semiconductor work function ( $\phi_s$ ) is lower than the metal work function ( $\phi_m$ ).<sup>65</sup>

As seen in **Figure 1.7** the band bending depends on the work function of both materials, when  $\phi_m > \phi_s$ , the bands bend upwards, while when  $\phi_m < \phi_s$  they bend downwards, this could be easily explained by the electrostatic energy on the interface, for example, since on **Figure 1.7A** electrons are on the metal surface, the energy needed for an electron to migrate from the semiconductor to the metal would be higher due to repulsion from the negatively charged metal surface, this energy barrier is called the Schottky barrier. On the other hand, in **Figure 1.7B**, the metallic interface is positively charged; thus, electrons do not suffer repulsion from the metal, creating an ohmic contact.

## 1.6 – Metallic nanoparticles as catalysts for reduction reactions

### 1.6.1 – Hydrogenation reactions

Among the several different reactions that are widely employed in the industry, reduction reactions are widely applied to generate from fine chemicals to energy production and storage.<sup>66–68</sup> In the cases where hydrogen is employed as the reducing agent, the reactions can also be called catalytic hydrogenation reactions. Catalytic hydrogenation reactions were traditionally studied using metals such as Ni, Pd, Ru, and Pt due to their high activity towards these reactions, which relates to their band structure and electron distribution.<sup>69</sup> **Figure 1.8A** displays the favorability of molecular hydrogen to be split into hydrides on the surface of metals such as Au, Cu, Pt, and Ni.<sup>70</sup> When  $H_2$  approaches either the Ni or the Pt surface, the splitting of this molecule is energetically favored, and thus, hydrogenation reactions happen with ease on their surface. For both Au and Cu, this splitting is unfavored due to their d-band structure. For years Au was thought as being inactive towards hydrogenation reactions; however, it was found that in the nanoscale, its activity changes and the metal can be activated towards hydrogenations.<sup>71</sup>

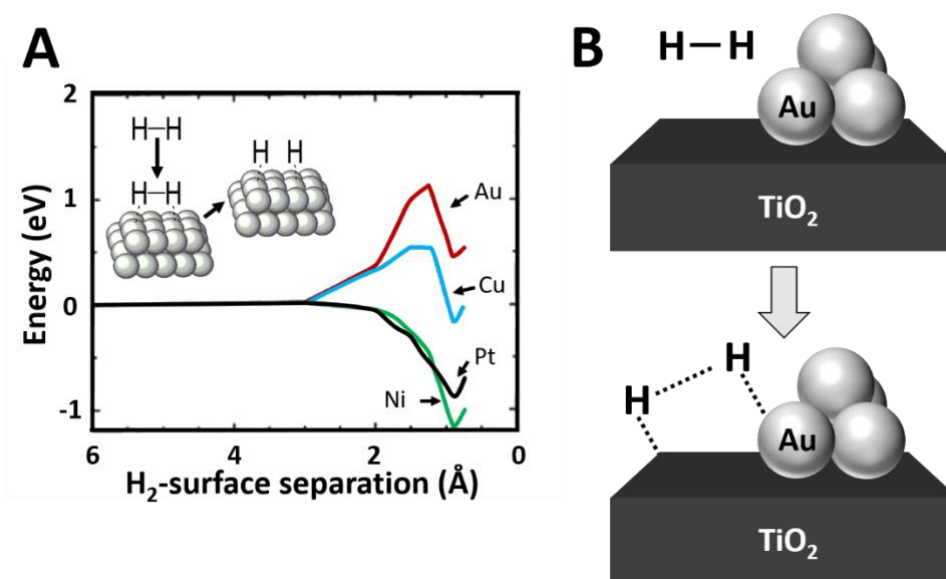


**Figure 1.8** – (A) Energy necessary to split hydrogen molecules on the surface of different metals, Pt (black line) and Ni (green line) are metals in which the splitting is favorable energetically while Au (red line) and Cu (blue line) provide some resistance towards this splitting. (B) Molecular hydrogen splitting on Au aided by a TiO<sub>2</sub> surface.<sup>70,72</sup>

Ever since, the search for more straightforward ways of activating Au materials towards these reactions has increased drastically. From the combination with different supports (**Figure 1.8B**) to the functionalization of the Au surface, or the addition of promoters, Au has now shown interesting activities and selectivities on semi-hydrogenation reactions.<sup>73,74</sup>

Some challenges faced in this field would be the lack of selectivity of some catalysts, their activities,<sup>75</sup> and the stability of catalysts, which under certain drastic conditions may change in shape, or size or even deactivate.<sup>76</sup> Moreover, by employing light-activated materials, one could provide milder reaction conditions and therefore slow down the degradation of a catalyst, which would play an essential role in a long-term application.<sup>77</sup> Finally, understanding the intrinsic factors behind the activity of a catalyst is of uttermost importance when designing materials for a specific application.<sup>78</sup>

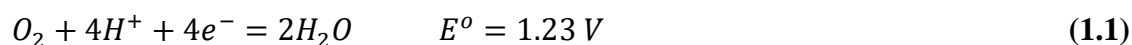
Several hydrogenation reactions are studied using metallic NPs as catalysts, since approximately 25% of the industrial processes present at least one catalytic hydrogenation step in their course.<sup>78</sup> Little progress had been made towards the industrial applications of catalysts on hydrogenation reactions, and in many cases, harmful materials are still employed.<sup>78</sup> Due to the vast number of hydrogenation reactions and the environmental benefits new catalysts could bring to the industry, in the past decade, there was a considerable number of publications and patents on the field.<sup>78</sup>

Although many reactions are of great importance, we will focus in this dissertation only on the hydrogenation of alkynes, nitroarenes, and epoxides. These are important towards the production of polymers, pharmaceuticals, fragrances, fine chemicals, among others.<sup>78,79</sup> The hydrogenation of alkynes happens through the dissociation of  $H_2$  into its atomic species that on its turn can semi-hydrogenate alkynes to alkenes or over hydrogenate them into alkanes.<sup>80,81</sup> The nitroarene hydrogenation follows a similar path, splitting hydrogen to hydrogenate the nitro onto the nitroso product, followed by the hydroxylamine one.<sup>82,83</sup> Yet the hydrogenation of epoxides can go through many different pathways, forming either the more substituted alcohol or, the less substituted one,<sup>72,84</sup> deoxygenating it and generating the alkene, or even further hydrogenating the alkene to alkane in a sequential step.<sup>85</sup> An epoxide also can undergo an isomerization process, producing the aldehyde.<sup>86,87</sup>

As mentioned, the selectivity of these reactions towards one specific product may be challenging to achieve, although by choosing the right metal or right conditions for the reaction may be helpful, tailoring surface properties and charge transfer mechanisms can improve or even manage the selectivity in these reactions.<sup>88–90</sup>

### 1.6.2 – Oxygen reduction reaction

Due to extensive investigation towards green energy production, the oxygen reduction reaction (ORR) is of high economic importance. In proton exchange membrane (PEM) fuel cells, for example, the ORR usually is responsible for the cathode, thus significantly contributing to its overall energy production. Considering the slow kinetics of this reaction, employing a catalyst is fundamental to increase total energy production. Depending on the catalyst, the ORR tends to follow a different path. Typically, the reaction follows either the 4-electron path, producing water (**Equation 1.1**) or the 2-electron path, producing hydrogen peroxide (**Equation. 1.2**).<sup>91</sup>



H<sub>2</sub>O<sub>2</sub> is known as an undesirable product responsible for damaging parts of the fuel cell and lowering the overall energy output. Therefore, decreasing or eliminating its production is beneficial to the entire process. As an efficient catalyst for water production, Pt is mostly used due to its efficiency on this reaction, which can be attributed to the strength of adsorption and desorption to the oxygenated species present in the reaction.<sup>92</sup> It also tends to have good chemical stability under the corrosive conditions where this reaction take place. However, the sluggish kinetics of ORR requires high Pt loadings in the cathode.<sup>93</sup>

Considering the price and availability of Pt, developing low-cost catalysts with enhanced activity for the ORR is a desire of many. In this context, researchers have been studying nanostructures using auxiliary metals to Pt and even Pt-free materials.<sup>94</sup> The challenges are to obtain alloys or hybrid materials with higher stability than Pt, without affecting the favorable binding energy between Pt and oxygen. Aside from this metal's

properties, the effect of low index surfaces on Pt NPs has been extensively studied in the electrocatalytic reduction of oxygen.<sup>95</sup>

The commercially available Pt/C-ETEK (10 wt.% in Carbon) is well known as the most explored in electrocatalytic applications, due to its high Platinum content and nanoparticle monodispersion on the support.<sup>96</sup> Controlling size and shape of metallic NPs is a fundamental part of catalyst evaluation since these properties are directly related to the surface of the material and therefore to its activity. Though it may seem a great fit for fuel cells, Pt/C has been known for its low stability under oxidizing environments. In the presence of oxygen, Pt NPs tend on catalyzing the autodegradation of Pt/C, converting the carbon support to CO<sub>2</sub>.<sup>97,98</sup> An alternative to overcome this challenge is to support Pt NPs onto oxides, such as TiO<sub>2</sub>, which is a low-cost transition metal oxide, with a non-toxic nature, high stability in acidic media and can present a strong metal-support interaction with Pt.<sup>99</sup> Moreover, its properties can be improved under UV illumination (band gap of about 3.2 eV), and when supported on carbon, its electron conductivity and corrosion resistance are increased. This material is also known to suppress carbon degradation, thus extending the catalyst's lifetime.<sup>100</sup>

## 1.7 – References

1. Bell, A. T. The Impact of Nanoscience on Heterogeneous Catalysis. *Science* (80-. ). **299**, 1688–1691 (2003).
2. Li, Y. & Somorjai, G. A. Nanoscale Advances in Catalysis and Energy Applications. *Nano Lett.* **10**, 2289–2295 (2010).
3. Gellman, A. J. & Shukla, N. Nanocatalysis: More than speed. *Nat. Mater.* **8**, 87–88 (2009).
4. Grunes, J., Zhu, J. & Somorjai, G. a. Catalysis and nanoscience. *Chem. Commun.* 2257 (2003). doi:10.1039/b305719b
5. Astruc, D., Lu, F. & Aranzaes, J. R. Nanoparticles as Recyclable Catalysts: The Frontier between Homogeneous and Heterogeneous Catalysis. *Angew. Chemie Int. Ed.* **44**, 7852–7872 (2005).
6. Gao, G., Jiao, Y., Wacławik, E. R. & Du, A. Single Atom (Pd/Pt) Supported on Graphitic Carbon Nitride as an Efficient Photocatalyst for Visible-Light Reduction of Carbon Dioxide. *J. Am. Chem. Soc.* **138**, 6292–6297 (2016).
7. Campelo, J. M., Luna, D., Luque, R., Marinas, J. M. & Romero, A. A. Sustainable Preparation of Supported Metal Nanoparticles and Their Applications in Catalysis. *ChemSusChem* **2**, 18–45 (2009).
8. Peng, S. *et al.* A facile synthesis of monodisperse Au nanoparticles and their catalysis of CO oxidation. *Nano Res.* **1**, 229–234 (2008).
9. Nguyen, B. H. & Nguyen, V. H. Recent advances in research on plasmonic enhancement of photocatalysis. *Adv. Nat. Sci. Nanosci. Nanotechnol.* **6**, 043001 (2015).
10. Zhang, C., Chen, B.-Q., Li, Z.-Y., Xia, Y. & Chen, Y.-G. Surface Plasmon Resonance in Bimetallic Core–Shell Nanoparticles. *J. Phys. Chem. C* **119**, 16836–16845 (2015).
11. Major, K. J., De, C. & Obare, S. O. Recent advances in the synthesis of plasmonic



- bimetallic nanoparticles. *Plasmonics* **4**, 61–78 (2009).
12. Xia, Y., Xia, X., Wang, Y. & Xie, S. Shape-controlled synthesis of metal nanocrystals. *Mrs Bull* **38**, 335–344 (2013).
  13. Au, L., Chen, J., Wang, L. V & Xia, Y. Gold nanocages for cancer imaging and therapy. in *Cancer Nanotechnology* 83–99 (Springer, 2010).
  14. Boisselier, E. & Astruc, D. Gold nanoparticles in nanomedicine: preparations, imaging, diagnostics, therapies and toxicity. *Chem. Soc. Rev.* **38**, 1759–1782 (2009).
  15. Polshettiwar, V. & Varma, R. S. Green chemistry by nano-catalysis. *Green Chem.* **12**, 743 (2010).
  16. Somorjai, G. A., Frei, H. & Park, J. Y. Advancing the frontiers in nanocatalysis, biointerfaces, and renewable energy conversion by innovations of surface techniques. *J. Am. Chem. Soc.* **131**, 16589–16605 (2009).
  17. Xia, Y., Xiong, Y., Lim, B. & Skrabalak, S. E. Shape-controlled synthesis of metal nanocrystals: Simple chemistry meets complex physics? *Angew. Chemie Int. Ed.* **48**, 60–103 (2009).
  18. Hervés, P. *et al.* Catalysis by metallic nanoparticles in aqueous solution: model reactions. *Chem. Soc. Rev.* **41**, 5577 (2012).
  19. Mayer, M. *et al.* Aqueous Gold Overgrowth of Silver Nanoparticles: Merging the Plasmonic Properties of Silver with the Functionality of Gold. *Angew. Chemie Int. Ed.* **56**, 15866–15870 (2017).
  20. Li, M. & Chen, G. Revisiting catalytic model reaction p-nitrophenol/NaBH<sub>4</sub> using metallic nanoparticles coated on polymeric spheres. *Nanoscale* **5**, 11919 (2013).
  21. Da Silva, A. G. M. *et al.* The Fault in Their Shapes: Investigating the Surface-Plasmon-Resonance-Mediated Catalytic Activities of Silver Quasi-Spheres, Cubes, Triangular Prisms, and Wires. *Langmuir* **31**, 10272–10278 (2015).

22. Feld, A. *et al.* Chemistry of Shape-Controlled Iron Oxide Nanocrystal Formation. *ACS Nano* **13**, 152–162 (2018).
23. Lim, B. *et al.* Shape-controlled synthesis of Pd nanocrystals in aqueous solutions. *Adv. Funct. Mater.* **19**, 189–200 (2009).
24. Eiden-Assmann, S., Widoniak, J. & Maret, G. Synthesis and Characterization of Porous and Nonporous Monodisperse Colloidal TiO<sub>2</sub> Particles. *Chem. Mater.* **16**, 6–11 (2004).
25. da Silva, A. G. M., Rodrigues, T. S., Haigh, S. J. & Camargo, P. H. C. Galvanic replacement reaction: recent developments for engineering metal nanostructures towards catalytic applications. *Chem. Commun.* **53**, 7135–7148 (2017).
26. Yu, J., Low, J., Xiao, W., Zhou, P. & Jaroniec, M. Enhanced Photocatalytic CO<sub>2</sub> Reduction Activity of Anatase TiO<sub>2</sub> by Coexposed {001} and {101} Facets. *J. Am. Chem. Soc.* **136**, 8839–8842 (2014).
27. Li, N. *et al.* Enhanced Photocatalytic Performance toward CO<sub>2</sub> Hydrogenation over Nanosized TiO<sub>2</sub>-Loaded Pd under UV Irradiation. *J. Phys. Chem. C* **121**, 2923–2932 (2017).
28. Li, N. *et al.* Enhanced Visible Light Photocatalytic Hydrogenation of CO<sub>2</sub> into Methane over a Pd/Ce-TiO<sub>2</sub> Nanocomposition. *J. Phys. Chem. C* **acs.jpcc.7b07298** (2017). doi:10.1021/acs.jpcc.7b07298
29. Yin, G. *et al.* Efficient Conversion of CO<sub>2</sub> to Methane Photocatalyzed by Conductive Black Titania. *ChemCatChem* 1–9 (2017). doi:10.1002/cctc.201701130
30. Zhang, L. *et al.* Direct coupling of thermo- and photo-catalytic conversion of CO<sub>2</sub>-H<sub>2</sub>O to fuels. *ChemSusChem* 1–7 (2017). doi:10.1002/cssc.201701472
31. Xia, Y., Yang, H. & Campbell, C. T. Nanoparticles for Catalysis. *Acc. Chem. Res.* **46**, 1671–1672 (2013).

32. Hagen, J. *Industrial Catalysis. Industrial Catalysis: A Practical Approach: Second Edition* (Wiley, 2005). doi:10.1002/3527607684
33. Gates, B. C. & Marks, T. J. Defragmenting Catalysis. *Angew. Chemie Int. Ed.* **51**, 11644–11645 (2012).
34. Dou, J. *et al.* Operando chemistry of catalyst surfaces during catalysis. *Chem. Soc. Rev.* **46**, 2001–2027 (2017).
35. Thomas, J. M. & Thomas, W. J. *Principles and Practice of heterogeneous catalysis*. (VCH Verlagsgesellschaft mbH, 1997).
36. Jain, P. K. & El-Sayed, M. A. Plasmonic coupling in noble metal nanostructures. *Chem. Phys. Lett.* **487**, 153–164 (2010).
37. Willets, K. A. & Van Duyne, R. P. Localized Surface Plasmon Resonance Spectroscopy and Sensing. *Annu. Rev. Phys. Chem.* **58**, 267–297 (2007).
38. Xia, Y. & Halas, N. J. Shape-Controlled Synthesis and Surface Plasmonic Properties of Metallic Nanostructures. *MRS Bull.* **30**, 338–348 (2011).
39. Linic, S., Aslam, U., Boerigter, C. & Morabito, M. Photochemical transformations on plasmonic metal nanoparticles. *Nat. Mater.* **14**, 567–576 (2015).
40. Quiroz, J. *et al.* Controlling Reaction Selectivity over Hybrid Plasmonic Nanocatalysts. *Nano Lett.* **18**, 7289–7297 (2018).
41. Baffou, G. & Quidant, R. Nanoplasmonics for chemistry. *Chem. Soc. Rev.* **43**, 3898–3907 (2014).
42. Zhang, Y. *et al.* Surface-Plasmon-Driven Hot Electron Photochemistry. *Chem. Rev.* **118**, 2927–2954 (2018).
43. Brongersma, M. L., Halas, N. J. & Nordlander, P. Plasmon-induced hot carrier science and technology. *Nat. Nanotechnol.* **10**, 25–34 (2015).
44. Baffou, G. & Quidant, R. Thermo-plasmonics: Using metallic nanostructures as nano-

- sources of heat. *Laser Photonics Rev.* **7**, 171–187 (2013).
45. Zhou, X., Qiao, J., Yang, L. & Zhang, J. A review of graphene-based nanostructural materials for both catalyst supports and metal-free catalysts in PEM fuel cell oxygen reduction reactions. *Adv. Energy Mater.* **4**, 1–25 (2014).
  46. White, R. J., Luque, R., Budarin, V. L., Clark, J. H. & MacQuarrie, D. J. Supported metal nanoparticles on porous materials. Methods and applications. *Chem. Soc. Rev.* **38**, 481–494 (2009).
  47. Jiang, R., Li, B., Fang, C. & Wang, J. Metal/Semiconductor Hybrid Nanostructures for Plasmon-Enhanced Applications. *Adv. Mater.* **26**, 5274–5309 (2014).
  48. Rahman, D. S. & Ghosh, S. K. Manipulating Electron Transfer in Hybrid ZnO–Au Nanostructures: Size of Gold Matters. *J. Phys. Chem. C* **120**, 14906–14917 (2016).
  49. Sotiriou, G. A. *et al.* Hybrid, silica-coated, Janus-like plasmonic-magnetic nanoparticles. *Chem. Mater.* **23**, 1985–1992 (2011).
  50. Naya, S. ichi & Tada, H. Dependence of the plasmonic activity of Au/TiO<sub>2</sub> for the decomposition of 2-naphthol on the crystal form of TiO<sub>2</sub> and Au particle size. *J. Catal.* **364**, 328–333 (2018).
  51. Zheng, Z. *et al.* Facile in situ synthesis of visible-light plasmonic photocatalysts M@TiO<sub>2</sub> (M = Au, Pt, Ag) and evaluation of their photocatalytic oxidation of benzene to phenol. *J. Mater. Chem.* **21**, 9079 (2011).
  52. Sampaio, M. J. *et al.* Ag-loaded ZnO materials for photocatalytic water treatment. *Chem. Eng. J.* **318**, 95–102 (2017).
  53. Bamwenda, G. R., Tsubota, S., Nakamura, T. & Haruta, M. Photoassisted hydrogen production from a water-ethanol solution: a comparison of activities of Au/TiO<sub>2</sub> and Pt/TiO<sub>2</sub>. *J. Photochem. Photobiol. A Chem.* **89**, 177–189 (1995).
  54. Damato, T. C., de Oliveira, C. C. S., Ando, R. A. & Camargo, P. H. C. A Facile

- Approach to TiO<sub>2</sub> Colloidal Spheres Decorated with Au Nanoparticles Displaying Well-Defined Sizes and Uniform Dispersion. *Langmuir* **29**, 1642–1649 (2013).
55. Chan, S. C. & Barteau, M. A. Preparation of Highly Uniform Ag / TiO<sub>2</sub> and Au / TiO<sub>2</sub> Supported Nanoparticle Catalysts by Photodeposition. *Image (Rochester, N.Y.)* **21**, 5588–5595 (2005).
  56. Wenderich, K. & Mul, G. Methods, Mechanism, and Applications of Photodeposition in Photocatalysis: A Review. *Chem. Rev.* acs.chemrev.6b00327 (2016).  
doi:10.1021/acs.chemrev.6b00327
  57. Zhong, R. Y., Sun, K. Q., Hong, Y. C. & Xu, B. Q. Impacts of organic stabilizers on catalysis of Au nanoparticles from colloidal preparation. *ACS Catal.* **4**, 3982–3993 (2014).
  58. Zheng, G. *et al.* Encapsulation of Single Plasmonic Nanoparticles within ZIF-8 and SERS Analysis of the MOF Flexibility. *Small* **12**, 3935–3943 (2016).
  59. Li, J. *et al.* Ag@Cu<sub>2</sub>O Core-Shell Nanoparticles as Visible-Light Plasmonic Photocatalysts. *ACS Catal.* **3**, 47–51 (2013).
  60. Wang, L. *et al.* Iron oxide–gold core–shell nanoparticles and thin film assembly. *J. Mater. Chem.* **15**, 1821 (2005).
  61. Xiong, Z., Zhang, L. & Zhao, X. S. One-step synthesis of metal@titania core-shell materials for visible-light photocatalysis and catalytic reduction reaction. *Chem. - A Eur. J.* **20**, 14715–14720 (2014).
  62. Wu, X.-F., Song, H.-Y., Yoon, J.-M., Yu, Y.-T. & Chen, Y.-F. Synthesis of Core–Shell Au@TiO<sub>2</sub> Nanoparticles with Truncated Wedge-Shaped Morphology and Their Photocatalytic Properties. *Langmuir* **25**, 6438–6447 (2009).
  63. Dong, R., Zhang, Q., Gao, W., Pei, A. & Ren, B. Highly Efficient Light-Driven TiO<sub>2</sub> –Au Janus Micromotors. *ACS Nano* **10**, 839–844 (2016).

64. Daniel, M. C. & Astruc, D. Gold Nanoparticles: Assembly, Supramolecular Chemistry, Quantum-Size-Related Properties, and Applications Toward Biology, Catalysis, and Nanotechnology. *Chem. Rev.* **104**, 293–346 (2004).
65. Zhang, Z. & Yates, J. T. Band Bending in Semiconductors: Chemical and Physical Consequences at Surfaces and Interfaces. *Chem. Rev.* **112**, 5520–5551 (2012).
66. Álvarez, A. *et al.* Challenges in the Greener Production of Formates/Formic Acid, Methanol, and DME by Heterogeneously Catalyzed CO<sub>2</sub>Hydrogenation Processes. *Chem. Rev.* **117**, 9804–9838 (2017).
67. Blaser, H., Indolese, A., Schnyder, A., Steiner, H. & Studer, M. Supported palladium catalysts for fine chemicals synthesis. *J. Mol. Catal. A Chem.* **173**, 3–18 (2001).
68. Blaser, H., Malan, C., Pugin, B., Spindler, F. & Studer, M. Selective Hydrogenation for Fine Chemicals : Recent Trends and New Developments. *Adv. Synth. Catal.* **345**, 103–151 (2003).
69. Crampton, A. S. *et al.* Ethylene hydrogenation on supported Ni, Pd and Pt nanoparticles: Catalyst activity, deactivation and the d-band model. *J. Catal.* **333**, 51–58 (2016).
70. Hammer, B. & Norskov, J. K. Why gold is the noblest of all the metals. *Nature* **376**, 238–240 (1995).
71. Zhang, Y., Cui, X., Shi, F. & Deng, Y. Nano-Gold Catalysis in Fine Chemical Synthesis. *Chem. Rev.* **112**, 2467–2505 (2012).
72. Kominami, H. *et al.* Photocatalytic chemoselective reduction of epoxides to alkenes along with formation of ketones in alcoholic suspensions of silver-loaded titanium(iv) oxide at room temperature without the use of reducing gases. *Chem. Commun.* **50**, 4558 (2014).
73. Fiorio, J. L. *et al.* Accessing Frustrated Lewis Pair Chemistry through Robust

- Gold@N-Doped Carbon for Selective Hydrogenation of Alkynes. *ACS Catal.* **8**, 3516–3524 (2018).
74. Fiorio, J. L., López, N. & Rossi, L. M. Gold–Ligand-Catalyzed Selective Hydrogenation of Alkynes into cis -Alkenes via H<sub>2</sub> Heterolytic Activation by Frustrated Lewis Pairs. *ACS Catal.* **7**, 2973–2980 (2017).
  75. Corma, A. & Serna, P. Chemoselective Hydrogenation of Nitro Compounds with Supported Gold Catalysts. *Science (80-. )*. **313**, 332–334 (2006).
  76. Narayanan, R. & El-Sayed, M. A. Catalysis with Transition Metal Nanoparticles in Colloidal Solution: Nanoparticle Shape Dependence and Stability. *J. Phys. Chem. B* **109**, 12663–12676 (2005).
  77. Xu, L., Huang, W.-Q., Wang, L.-L., Huang, G.-F. & Peng, P. Mechanism of Superior Visible-Light Photocatalytic Activity and Stability of Hybrid Ag<sub>3</sub>PO<sub>4</sub>/Graphene Nanocomposite. *J. Phys. Chem. C* **118**, 12972–12979 (2014).
  78. Vilé, G., Albani, D., Almora-Barrios, N., López, N. & Pérez-Ramírez, J. Advances in the Design of Nanostructured Catalysts for Selective Hydrogenation. *ChemCatChem* **8**, 21–33 (2016).
  79. Shil, A. K., Sharma, D., Guha, N. R. & Das, P. Solid supported Pd (0): an efficient recyclable heterogeneous catalyst for chemoselective reduction of nitroarenes q. *Tetrahedron Lett.* **53**, 4858–4861 (2012).
  80. Segura, Y., López, N. & Pérez-Ramírez, J. Origin of the superior hydrogenation selectivity of gold nanoparticles in alkyne + alkene mixtures: Triple- versus double-bond activation. *J. Catal.* **247**, 383–386 (2007).
  81. García-Mota, M., Bridier, B., Pérez-Ramírez, J. & López, N. Interplay between carbon monoxide, hydrides, and carbides in selective alkyne hydrogenation on palladium. *J. Catal.* **273**, 92–102 (2010).

82. Aditya, T., Pal, A. & Pal, T. Nitroarene reduction: a trusted model reaction to test nanoparticle catalysts. *Chem. Commun.* **51**, 9410–9431 (2015).
83. Fountoulaki, S. *et al.* Mechanistic Studies of the Reduction of Nitroarenes by NaBH<sub>4</sub> or Hydrosilanes Catalyzed by Supported Gold Nanoparticles. *ACS Catal.* **4**, 3504–3511 (2014).
84. Kirm, I. *et al.* Preparation of 2-phenylethanol by catalytic selective hydrogenation of styrene oxide using palladium catalysts. *J. Mol. Catal. A Chem.* **239**, 215–221 (2005).
85. Noujima, A., Mitsudome, T., Mizugaki, T., Jitsukawa, K. & Kaneda, K. Selective Deoxygenation of Epoxides to Alkenes with Molecular Hydrogen Using a Hydrotalcite-Supported Gold Catalyst: A Concerted Effect between Gold Nanoparticles and Basic Sites on a Support. *Angew. Chemie Int. Ed.* **50**, 2986–2989 (2011).
86. Suda, K., Kikkawa, T., Nakajima, S. & Takanami, T. Highly Regio- and Stereoselective Rearrangement of Epoxides to Aldehydes Catalyzed by High-Valent Metalloporphyrin Complex, Cr(TPP)OTf. *J. Am. Chem. Soc.* **126**, 9554–9555 (2004).
87. Vyas, D. J., Larionov, E., Besnard, C., Guénée, L. & Mazet, C. Isomerization of Terminal Epoxides by a [Pd–H] Catalyst: A Combined Experimental and Theoretical Mechanistic Study. *J. Am. Chem. Soc.* **135**, 6177–6183 (2013).
88. Marimuthu, A., Zhang, J. & Linic, S. Tuning selectivity in propylene epoxidation by plasmon mediated photo-switching of Cu oxidation state. *Science (80-. ).* **339**, 1590–1593 (2013).
89. Kumar, P. V. & Norris, D. J. Tailoring Energy Transfer from Hot Electrons to Adsorbate Vibrations for Plasmon-Enhanced Catalysis. *ACS Catal.* **7**, 8343–8350 (2017).
90. Zhou, J.-H. *et al.* Characterization of surface oxygen complexes on carbon nanofibers



- by TPD, XPS and FT-IR. *Carbon N. Y.* **45**, 785–796 (2007).
91. Shimizu, K., Sepunaru, L. & Compton, R. G. Innovative catalyst design for the oxygen reduction reaction for fuel cells. *Chem. Sci.* **7**, 3364–3369 (2016).
92. Huang, Z.-F. *et al.* Design of Efficient Bifunctional Oxygen Reduction/Evolution Electrocatalyst: Recent Advances and Perspectives. *Adv. Energy Mater.* **7**, 1700544 (2017).
93. Sui, S. *et al.* A comprehensive review of Pt electrocatalysts for the oxygen reduction reaction: Nanostructure, activity, mechanism and carbon support in PEM fuel cells. *J. Mater. Chem. A* **5**, 1808–1825 (2017).
94. Nie, Y., Li, L. & Wei, Z. Recent advancements in Pt and Pt-free catalysts for oxygen reduction reaction. *Chem. Soc. Rev.* **44**, 2168–2201 (2015).
95. Wang, C., Daimon, H., Onodera, T., Koda, T. & Sun, S. A General Approach to the Size- and Shape-Controlled Synthesis of Platinum Nanoparticles and Their Catalytic Reduction of Oxygen. *Angew. Chemie Int. Ed.* **47**, 3588–3591 (2008).
96. Lewera, A., Timperman, L., Roguska, A. & Alonso-Vante, N. Metal–Support Interactions between Nanosized Pt and Metal Oxides (WO<sub>3</sub> and TiO<sub>2</sub>) Studied Using X-ray Photoelectron Spectroscopy. *J. Phys. Chem. C* **115**, 20153–20159 (2011).
97. Ruiz-Camacho, B., Martínez-Álvarez, O., Rodríguez-Santoyo, H. H. & Granados-Alejo, V. Pt/C and Pt/TiO<sub>2</sub>–C electrocatalysts prepared by chemical vapor deposition with high tolerance to alcohols in oxygen reduction reaction. *J. Electroanal. Chem.* **725**, 19–24 (2014).
98. Ruiz Camacho, B., Morais, C., Valenzuela, M. A. & Alonso-Vante, N. Enhancing oxygen reduction reaction activity and stability of platinum via oxide-carbon composites. *Catal. Today* **202**, 36–43 (2013).
99. Shanmugam, S. & Gedanken, A. Synthesis and Electrochemical Oxygen Reduction of

- Platinum Nanoparticles Supported on Mesoporous TiO<sub>2</sub>. *J. Phys. Chem. C* **113**, 18707–18712 (2009).
100. Huang, K., Sasaki, K., Adzic, R. R. & Xing, Y. Increasing Pt oxygen reduction reaction activity and durability with a carbon-doped TiO<sub>2</sub> nanocoating catalyst support. *J. Mater. Chem.* **22**, 16824 (2012).

## **Chapter 2 – Objectives of this work**

### **2.1 – General objectives**

This dissertation focuses on understanding of hydrogenation reactions with controlled nanomaterials composed of noble metals (Au, Pd or Pt) and semiconducting oxides (TiO<sub>2</sub> and Fe<sub>2</sub>O<sub>3</sub>). We aim at expanding the understanding about catalysts on the plasmonic hydrogenation of 4-nitrophenol and phenylacetylene, hydrogenation of styrene oxide, and on the electrocatalytic reduction of oxygen.

### **2.2 – Specific goals**

1) Studying the influence of changing the hydrogen source in a nitroarene hydrogenation reaction employing Au/TiO<sub>2</sub> as catalyst. In this case, we want to evaluate the influence of visible light onto the hydrogenation of both 4-nitrophenol and phenylacetylene, focusing on the plasmonic electron transfer within our samples and how they affect activities.

2) Verifying the influence of Pt coverage on TiO<sub>2</sub> samples towards the electrochemically activated reduction of oxygen. Here, we will investigate the influence of the NPs coverage and metal-support interactions over catalytic activities and stabilities, benchmarking those properties against the commercial Pt-based electrocatalysts.

3) Study Pd/Fe<sub>2</sub>O<sub>3</sub> nanomaterials composed of Pd NPs supported on Fe<sub>2</sub>O<sub>3</sub> microcubes over the hydrogenation of styrene epoxide. We will explore the effect of surfactant species over conversion, selectivity, and reusability.

**Section 2 – Metallic nanoparticles supported on  
semiconductor oxides towards reduction  
reactions**

## **Chapter 3 – Gold nanospheres supported on Titania: The dark side of photocatalytic hydrogenations**

### **3.1 – Introduction**

This chapter can be found on the journal Chemistry – A European Journal.<sup>1</sup>

Photocatalytic conversions mediated or enhanced by the localized surface plasmon resonance (LSPR) excitation in plasmonic NPs, the so-called plasmonic catalysis, have emerged as a relatively new frontier in heterogeneous catalysis.<sup>2–5</sup> In this case, gold (Au) and silver (Ag) nanoparticles (NPs), which support LSPR excitation in the visible and near-infrared range, are usually employed as catalysts.<sup>4,6–8</sup> The utilization of copper (Cu) and aluminum (Al) NPs as catalysts has also received attention.<sup>9–12</sup> Plasmonic nanocatalysis has become attractive towards the development of more environmentally friendly processes, as it enables the utilization of visible/solar light as a green energy input to drive and control a variety of transformations.<sup>4,13–17</sup> In fact, Ag and Au NPs as well as their hybrids with metal-oxides and graphene-based materials have been investigated as plasmonic catalysts, in which significant enhancements have been reported under LSPR excitation.<sup>18–27</sup> It has been established that the LSPR excitation can contribute to the enhancement in the rate of molecular transformations by a variety of mechanisms. These include local heating by plasmon decay and charge-transfer processes (via direct and indirect mechanisms) that occur as a result of the generation of LSPR-excited hot electrons and holes.<sup>3–5,16,17</sup>

Among the important classes of molecular transformations, hydrogenation reactions play a pivotal role in several petrochemical, chemical, and pharmaceutical processes and industries.<sup>28–30</sup> Therefore, improvements in catalytic performances are expected to lead to huge economic and environmental impacts. In this context, the proper choice of metal NPs (control over their size, shape, and composition), supports, and surface ligands have been

pursued in the field of heterogeneous catalysis in order to improve the performance towards hydrogenation reactions.<sup>31–34</sup> Regarding plasmonic catalysis, the effect of light excitation on the H<sub>2</sub> and D<sub>2</sub> exchange over Au/TiO<sub>2</sub> and Au/SiO<sub>2</sub> catalysts has been reported.<sup>35,36</sup> In this example, it has been demonstrated that LSPR-excited hot electrons are able to facilitate the H<sub>2(g)</sub> splitting rate at the surface of the NPs at room temperature when these materials are excited by green light. Interestingly, Pd concave nanocubes have also been investigated as plasmonic catalysts for the hydrogenation of styrene, in which it was shown that LSPR-excited hot electrons led to a decrease in catalytic activities.<sup>37</sup> These results demonstrate that the precise identification of the mechanisms by which LSPR-excitation affects performance is imperative for the design of optimized plasmonic catalysts. Even though several reports have focused on investigating the effect of LSPR excitation over the enhancement of numerous transformations, several questions remain. For instance, for a specific type of transformation, how sensitive is the LSPR-enhanced catalytic activity to the nature of the reducing agents, metal-substrate charge transfer processes, and reaction pathways?

In this chapter we explore the effect of the LSPR excitation in Au NPs over their catalytic activities towards hydrogenation reactions as a proof-of-concept transformation. We investigated the effect of two important variables over the plasmonic catalytic performances: *i*) the occurrence of charge transfer processes between the metal NPs and the support, and *ii*) the nature of the reducing agent that enable distinct reaction pathways. Specifically, we employed the hydrogenation of 4-nitrophenol as a model transformation, BH<sub>4</sub><sup>-</sup>(aq) or H<sub>2(g)</sub> as the reducing agents and Au/TiO<sub>2</sub> or Au/SiO<sub>2</sub> NPs as catalysts. Significant enhancements in activity were found under plasmonic excitation for Au/SiO<sub>2</sub> NPs. For Au/TiO<sub>2</sub> catalysts, while plasmonic enhancements were detected when H<sub>2(g)</sub> was employed as a reducing agent, negative catalytic effects were detected due to charge-transfer of LSPR excited hot electrons from Au to TiO<sub>2</sub> when the hydrogenation took place in the presence of BH<sub>4</sub><sup>-</sup>(aq). This

directional charge transfer at the interface was further supported by density functional theory (DFT) calculations.

## 3.2 – Experimental Section

### *Chemicals and instrumentation*

HAuCl<sub>4</sub>·3H<sub>2</sub>O (hydrogen tetrachloroaurate trihydrate, 48% in gold, Sigma-Aldrich), PVP (polyvinylpyrrolidone, Sigma-Aldrich, MW 55 000 g mol<sup>-1</sup>), C<sub>2</sub>H<sub>6</sub>O<sub>2</sub> (ethylene glycol, 99.5%, Synth), C<sub>3</sub>H<sub>6</sub>O (acetone, 99.5%, Synth), C<sub>2</sub>H<sub>6</sub>O (ethanol, 95%, Synth), C<sub>2</sub>H<sub>4</sub>O<sub>2</sub> (acetic acid, 99.7%, Synth), C<sub>6</sub>H<sub>8</sub>O<sub>6</sub> (ascorbic acid, 99.0%, Sigma-Aldrich), Ti(OBu)<sub>4</sub> (titanium butoxide, 97%, Sigma-Aldrich), NaBH<sub>4</sub> (sodium borohydride, ≥ 98%, Sigma-Aldrich), C<sub>6</sub>H<sub>5</sub>O<sub>3</sub>N (4-nitrophenol, ≥ 99%, Sigma-Aldrich), C<sub>8</sub>H<sub>6</sub> (Phenylacetylene, ≥ 98%, Sigma-Aldrich) and SiO<sub>2</sub> GF 254 (Silica-gel, Merck) were used as received. All chemicals were analytical grade reagents. Deionized water (18.2 MΩ) was used throughout the experiments.

Scanning electron microscopy images were obtained using a JEOL microscope FEG-SEM JSM 6330F operated at 5 kV. SEM samples were prepared by drop-casting an aqueous suspension of the particles on a Si wafer, followed by drying under ambient conditions. Transmission electron microscopy (TEM) images were obtained using a Tecnai FEI G20 operated at 200 kV. Samples were prepared by drop casting an alcoholic suspension of each particle in a carbon coated copper grid. Size distribution profile was determined by individually measuring the size of 200 particles from TEM images. UV-Vis spectra were obtained using a Shimadzu UV-2600 UV-Vis spectrophotometer and quartz cuvettes. All products were quantified using a Shimadzu GC-2010 Plus gas chromatograph with either a Restek RTX®-Wax column or a Restek RTX®-5 column depending on what reaction was being analyzed. If needed, the products were extracted with ethyl acetate. Au percentages were determined through flame atomic absorption spectrophotometry (FAAS) using a Shimadzu AA-6300 equipment.



*Synthesis of TiO<sub>2</sub> colloidal spheres*<sup>38</sup>

Typically, 4 mL of Ti(OBu)<sub>4</sub> was added drop-wise to 90 mL of ethyleneglycol and kept under medium stirring at room temperature for 8 hours. Next, this colorless mixture was poured into 400 mL of acetone containing 5 mL of water and 2 mL of acetic acid and kept under vigorous stirring at room temperature for 2 hours and at rest for 3 hours. At this point, titanium glycolate microspheres were formed. These colloids were washed 5 times using ethanol and precipitated by centrifugation (5000 rpm per 5 min). The following step consisted on suspending these microparticles in 100 mL of deionized water and keeping it under stirring at 70 °C for 8 hours, producing TiO<sub>2</sub> spheres, which were washed several times with ethanol and water (same rotation speed and time). The final product was suspended in 500 mL of water.

*Synthesis of TiO<sub>2</sub> colloidal spheres decorated with Au NPs (Au/TiO<sub>2</sub>)*<sup>38</sup>

To decorate the support, 7.5 mL of the TiO<sub>2</sub> suspension was added to a solution containing 12 mL of water, 60 mg of ascorbic acid and 70 mg of PVP. This orange mixture was kept under stirring for 10 minutes at 90 °C and, at this point, 10 mL of 1.0 mmol L<sup>-1</sup> AuCl<sub>4</sub><sup>-</sup> was quickly added to the mixture, producing a red suspension. This reaction was stopped after 30 minutes, producing Au/TiO<sub>2</sub>. The final product was thoroughly washed with ethanol twice and water three times (5000 rpm, 5 minutes) and dried under vacuum at room temperature.

*Synthesis of SiO<sub>2</sub> with Au NPs (Au/SiO<sub>2</sub> NPs)*

In a typical procedure, Au NPs were synthesized the same way as the TiO<sub>2</sub> was decorated, although for SiO<sub>2</sub>, no interaction occurred when adding the support before the particles were formed. Thus the particles were prepared by adding 12 mL of water containing

60 mg of ascorbic acid and 70 mg of PVP to a round-bottomed flask at 90 °C. This mixture was kept under stirring for 10 minutes at 90°C, followed by the quick addition of 10 mL of 1.0 mmol L<sup>-1</sup> AuCl<sub>4</sub><sup>-</sup> to the mixture, producing a red suspension. After 30 minutes, 150 mg of commercial SiO<sub>2</sub> were added to the mixture and left 5 hours under stirring at 90°C producing Au/SiO<sub>2</sub>. The final product was thoroughly washed with ethanol and water, and dried under vacuum at room temperature. A higher mass of SiO<sub>2</sub> was added due to the low surface area of the commercial material employed on this project.

#### *Para-nitrophenol hydrogenation using NaBH<sub>4</sub>*

Hydrogenation reactions were performed in a quartz cuvette and monitored using a UV-Visible Spectrophotometer ranging from 350 nm to 500 nm. Spectra were collected every 150 seconds. A solution containing  $4.7 \times 10^{-9}$  mol Au,  $7.0 \times 10^{-8}$  mol of 4-nitrophenol and 1 mL of distilled water was prepared for each material, and at last 1 mL of a freshly prepared sodium borohydride solution containing 2.5 mg was added. To calculate the conversion of 4-nitrophenol, the change in absorption of the band at 400 nm was monitored. When using TiO<sub>2</sub> colloidal spheres as catalyst, the same amount of catalyst used in the reaction with TiO<sub>2</sub>-Au NPs was employed, 7.1 µg of TiO<sub>2</sub> or  $5.7 \times 10^{-4}$  mol, for reactions under visible light, a commercial a 4.5 W LED lamp (Golden – National Brand) was set 5 cm away from the reactor, positioned on the top of it, thus, the position and distance of the lamp onto the reaction were kept constant to minimize any oscillations on light power. The power impinging the reactor was measured using a power meter set at 532 nm (Optical Power Meter model 1830 C – Newport) and corresponded to 3.2 mW cm<sup>-2</sup>.

Control experiments were performed in order to quantify the H<sub>2</sub> formation from the proposed oxidation of H<sub>2</sub> under LSPR excitation. Typically, 25 mg of sodium borohydride was added to 40 mL of water containing either 80 µg or 400 µg Au NPs on the hybrid

materials, quantified by Flame Atomic Absorption Spectroscopy. A control experiment was performed without any catalyst in solution. The experiments lasted 1 hour and the gases produced in the reaction flask were guided through a hose to an upside-down water-filled graduated cylinder and measured using a water displacement approach, these experiments were performed in triplicate to ensure reproducibility of the results.

#### *Phenylacetylene and 4-nitrophenol hydrogenation using H<sub>2</sub>*

Catalytic hydrogenation reactions using H<sub>2</sub> were performed in Fischer-Porter glass reactors connected to an H<sub>2</sub> reservoir with a pressure regulator which kept the pressure constant. In a typical procedure, 5 mg of catalyst was added to the reactor with 2 mL of ethanol, the volume of substrate added was calculated based on the Au mass on each sample with a molar ratio Au:substrate of 1:10. The reactor was initially purged with H<sub>2</sub> five times at 2 bar and then pressurized to 6 bar of H<sub>2</sub>. All experiments were performed at 100 °C. Phenylacetylene reduction reactions were allowed to occur for 5 hours. For reactions under visible light, the same previously mentioned commercial 4.5 W LED lamp was set 5 cm away from the reactors and remained in the same position for all experiments. These experiments were performed in triplicate to ensure the significance of their results. The products were quantified using a gas chromatograph with an adequate column for each compound, an internal standard (biphenyl) was also used to determine the conversion and selectivity of the products.

In order to study the effect of H<sub>2</sub> splitting at the Au NPs surface, a control experiment was performed by supplying hydrogen to the Au/TiO<sub>2</sub> NPs hybrid material following the same conditions as previously used on catalytic hydrogenations, but without using any substrate. After 5 hours, H<sub>2</sub> was removed by N<sub>2</sub> purging and bubbling for 30 min and the reactions proceeded by adding an adequate volume of phenylacetylene as such the molar ratio

Au:Phenylacetylene was equal to 2.5, due to the lowest availability of hydrogen during the reactions. The reactions were allowed to occur for 5 hours under N<sub>2</sub> atmosphere and 100 °C.

*Kinetic assays of 4-nitrophenol or phenylacetylene hydrogenation using H<sub>2(g)</sub>*

These experiments were also performed in Fischer-Porter glass reactors connected to an H<sub>2</sub> reservoir with a pressure regulator. In a typical procedure, 10 mg of catalyst was added to the reactor with 4 mL of ethanol, the volume of substrate added was calculated based on Au's mass on the sample with a molar ratio Au:substrate of 1:10. The reactor was purged with hydrogen 5 times at 2 bar and then filled with 6 bar of H<sub>2</sub>. In order to maintain the temperature at 20 °C, a water bath was used. Aliquots were collected at specific times under N<sub>2</sub> atmosphere. For reactions under visible light, the same commercial 4.5 W LED lamp was set 5 cm away from the reactors and set in a fixed position to minimize power oscillations. The light power impinging the reactor was measured using a power meter set at 532 nm (Optical Power Meter model 1830 C – Newport) and corresponded to 3.2 mW cm<sup>-2</sup>. These experiments were performed in triplicate to ensure the significance of their results. The products were quantified using a gas chromatograph with an adequate column for each compound, an internal standard was also used to determine the conversion and selectivity of the products.

*Computational methods:*

DFT computations were performed using the Vienna ab initio simulation package (VASP). The ion-electron interaction was described through the projector-augmented wave (PAW) approach. The exchange and correlation energy were represented using the Perdew-Burke-Ernzerhof (PBE) functional of the generalized gradient approximation (GGA). The van der Waals (vdW) interaction has been taken into account through the Grimme's DFT-D3

semi-empirical method. Since the standard DFT formulation usually fails to describe strongly correlated electrons, the DFT+U method was used by introducing a Hubbard U correction with a value of 3.23 eV acting on 3d electrons of Ti. The model system is a supercell built based on four (4×4) repeated slabs of Au (111) adsorbed on five (5×5) repeated slabs (O-Ti-O trilayers) of TiO<sub>2</sub> anatase (101) with lattice parameters  $a = 10.36 \text{ \AA}$ ,  $b = 11.44 \text{ \AA}$  taken from an optimized TiO<sub>2</sub> unit cell. The bottom three layers of the TiO<sub>2</sub> slab were fixed to reflect the bulk. A vacuum space of at least 20  $\text{\AA}$  was included in the supercell to minimize the interaction between the system and its replicas resulting from the periodic boundary condition. The 4-nitrophenol or H<sub>2</sub> molecule was positioned above the Au surface. The Brillouin zone was sampled by a k-point mesh of (3×3×1) for geometry optimizations, and (6×6×2) for the density of states (DOS) calculations. A cutoff energy of 300 eV was found to be sufficient to provide convergent results. The structures were relaxed until the atomic force became smaller than 0.01 eV/ $\text{\AA}$ . All the calculations were performed using a Gaussian smearing with a width of 0.2 eV.

### 3.3 – Results and Discussion

In order to synthesize the  $\text{TiO}_2$  microspheres, a known method was employed, in which titanium tetrabutoxide was used as precursor. This precursor, due to its instability under ambient conditions, normally oxidizes in air to form titanium dioxide. Therefore, in the first stage of this synthesis, a simple ligand exchange step is performed by employing ethylene glycol as the new ligand. Yu, H. *et al.* showed that this ligand exchange tends to form chains in which Ti is seen as the metallic center, as shown on **Figure 3.1**.<sup>39</sup>

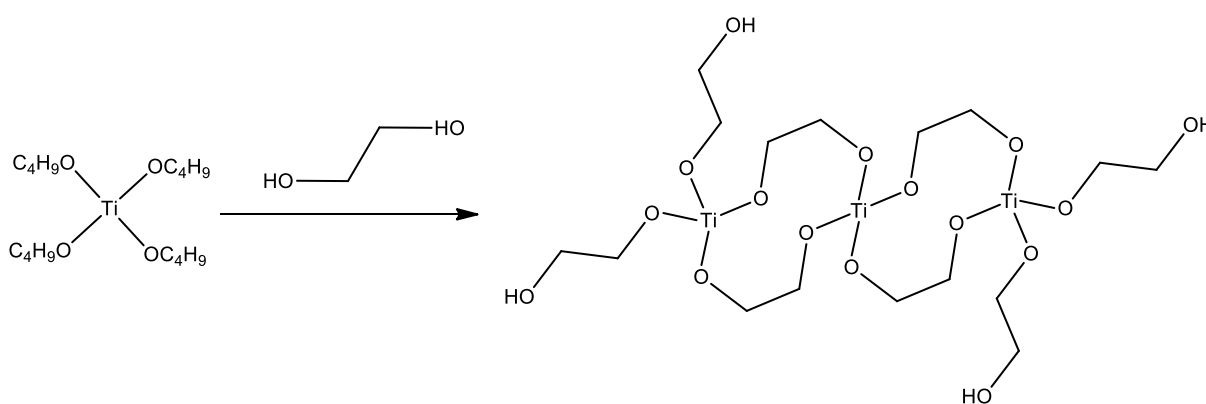


**Figure 3.1** – Representation of structure formed when the titanium alkoxide is reacted with ethylene glycol. Following this step, the structures tend on forming a whole network of titanium glycolate. Adapted from Yu, H. *et al.*

After the glycolate is formed, the next step consists on reacting this precursor with water in a controlled way to generate spherical particles, therefore, a low amount of water is used while acetone is the solvent and acetic acid is used to promote the hydrolysis. After adding the titanium glycolate to the mixture, spheres of this compound are formed, with no apparent peak on the XRD spectrum, although they already present spherical shapes.<sup>40</sup> The next step consisted on converting the titanium glycolate materials into Titanium dioxide by a simple hydrothermal treatment at  $70^\circ\text{C}$  for 8 hours, which was enough to maintain the shape although changing their crystal structure.<sup>38</sup>

A scanning electron microscopy image of the titanium dioxide microspheres can be seen on **Figure 3.2**. From SEM images, it is possible to measure several spheres and plot a histogram of size distribution which indicates that they measure  $267.8 \pm 37.8$  nm in diameter and are monodisperse. Even though their shapes are mostly spherical, on SEM images they display slightly rough surfaces which can play an important role towards surface area enhancement.

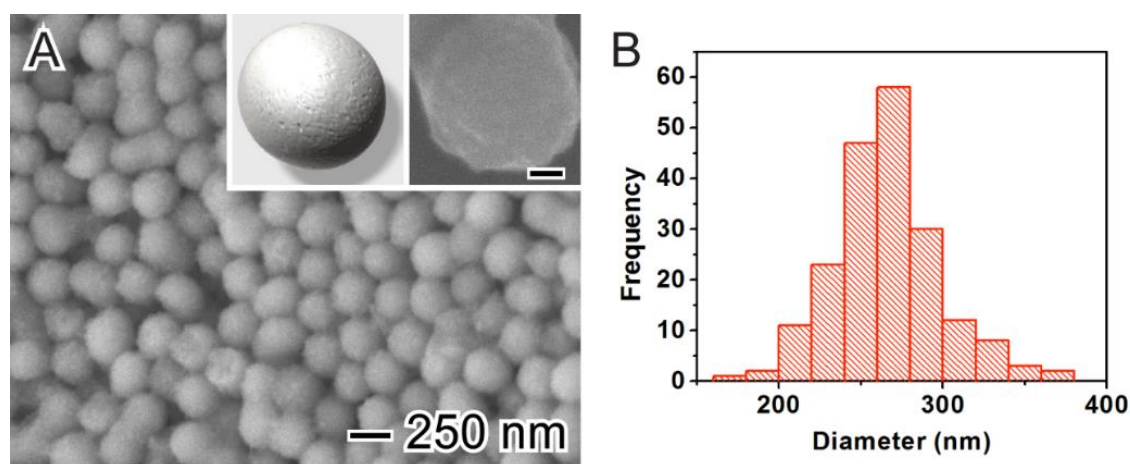


**Figure 3.2** – SEM image (A), and its histogram of size distribution (B) for the TiO<sub>2</sub> colloidal spheres. The scale bar in the inset corresponds to 50 nm.

In order to deposit Au NPs on top of the pre-synthesized microspheres, an *in-situ* reduction method was employed. In this case, the pre-formed TiO<sub>2</sub> colloidal spheres were used as seeds for the deposition of Au NPs using AuCl<sub>4</sub>-(aq) as precursor, ascorbic acid (AA) as reducing agent, polyvinylpyrrolidone (PVP) as stabilizer, and 90°C as the reaction temperature. **Figure 3.3** displays a graphical illustration of the method employed for these syntheses.<sup>38</sup> Initially, the suspension presents a milky white color, characteristic of TiO<sub>2</sub> materials. After the addition of ascorbic acid, the suspension drastically changes to an orange color, which has been assigned as the result of the oxygens from ascorbic acid bonding to the Ti<sub>4+</sub> ions on its surface. This results in a bidentate complex that allows for the resonance of electrons, granting this compound color.<sup>41</sup>

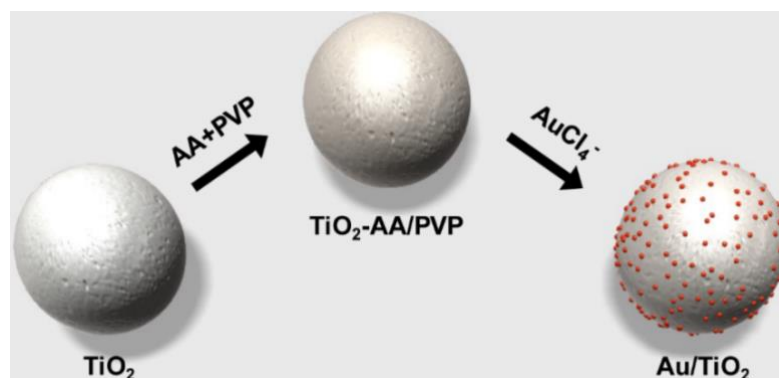


**Figure 3.3** – Schematic representation for the synthesis of  $\text{TiO}_2$  colloidal spheres and  $\text{TiO}_2$  colloidal spheres decorated with Au NPs ( $\text{Au/TiO}_2$ ). The microspheres are reacted with ascorbic acid and PVP for 10 minutes prior to the reduction of the Au precursor.

In order to verify the success of the syntheses, analysis such as electron microscopy and UV-Vis spectroscopy were employed. **Figure 3.4** depicts SEM and TEM images of the produced  $\text{Au/TiO}_2$  materials, an analogous  $\text{Au/SiO}_2$  material and their respective UV-Vis spectra. The  $\text{SiO}_2$  sample was prepared in order to compare two materials with different band structures and different surface properties. While  $\text{TiO}_2$  is a semiconductor with a surface that can participate in hydrogenation reactions,  $\text{SiO}_2$  is an insulator material considered as inert.<sup>35,36</sup>

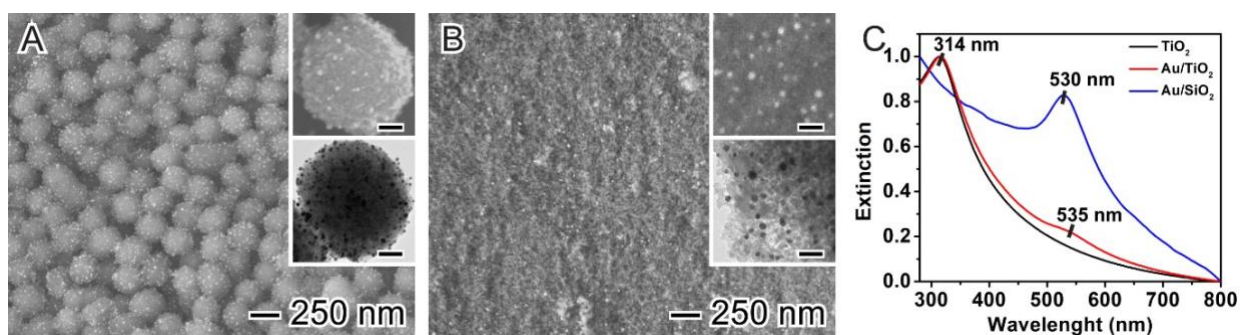


**Figure 3.4** – SEM and TEM (inset) images of Au NPs supported onto  $\text{TiO}_2$  colloidal spheres (A) and commercial  $\text{SiO}_2$  (B). The Au NPs supported on  $\text{SiO}_2$  and  $\text{TiO}_2$  measured  $13.6 \pm 2.7$  and  $9.7 \pm 2.2$  nm, respectively. The scale bars in the insets correspond to 50 nm. (B) UV-VIS extinction spectra recorded from aqueous suspensions containing  $\text{TiO}_2$ ,  $\text{Au/TiO}_2$  or  $\text{Au/SiO}_2$  materials (black, red and blue traces, respectively).



The Au NPs (**Figure 3.4A**) were monodisperse, uniformly deposited at the TiO<sub>2</sub> surface (no agglomeration) and measured  $9.7 \pm 2.2$  nm in diameter (Size distribution histogram as seen on **Figure 3.5A**). The Au/TiO<sub>2</sub> catalyst contained 12.0 wt.% Au while the Au/SiO<sub>2</sub> contained 0.8 wt.% as determined by Flame Atomic Absorption Spectroscopy (FAAS). It has been demonstrated that charge transfer between Au and TiO<sub>2</sub> can take place under LSPR excitation, in which LSPR excited hot electrons are transferred from Au to the TiO<sub>2</sub> conduction band.<sup>42–44</sup> Also, a charge transfer of photo-excited electrons from TiO<sub>2</sub> to Au can take place under UV illumination.<sup>45</sup> Therefore, this system becomes very attractive as a model plasmonic catalyst in order to investigate the effect of charge transfer between the plasmonic nanoparticle and the support over catalytic activities. As for the analogous system, the Au/SiO<sub>2</sub> catalyst by immobilization of pre-synthesized Au NPs (the histogram of size distribution is seen on **Figure 3.5B**) on commercial silica as shown in **Figure 3.4B** (SEM and TEM images). The Au NPs were  $13.6 \pm 2.7$  nm in diameter and uniformly deposited over the SiO<sub>2</sub> surface without any significant agglomeration. This material was employed as a reference as no charge transfer occurs between the support (SiO<sub>2</sub>) and the plasmonic NPs (Au) either under visible (LSPR) or UV excitation.

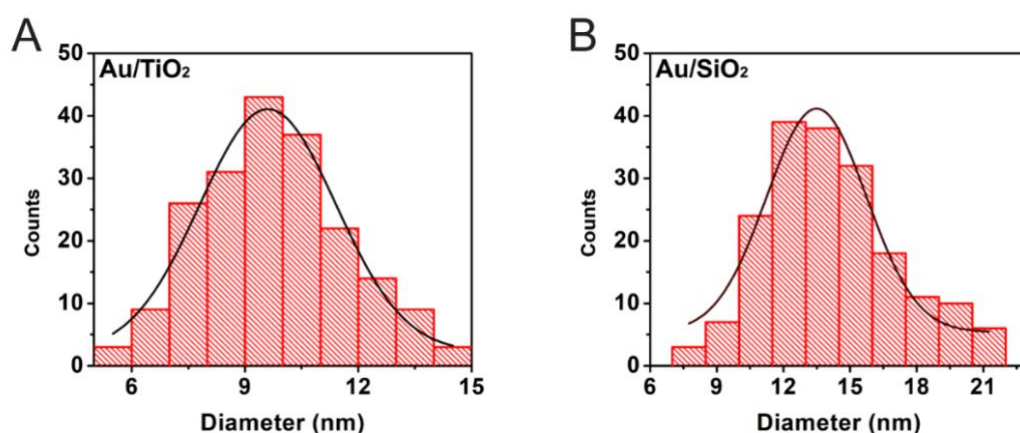


**Figure 3.5** – Histograms of size distribution for the Au NPs on the (A) Au/TiO<sub>2</sub> materials and (B) Au/SiO<sub>2</sub> materials. The average size corresponded to  $9.7 \pm 2.2$  nm and  $13.6 \pm 2.7$  nm in diameter, respectively.

The UV-VIS extinction spectra for TiO<sub>2</sub>, Au/TiO<sub>2</sub>, and Au/SiO<sub>2</sub> are shown in **Figure 3.4C**. In addition to the peak assigned to the TiO<sub>2</sub> band gap excitation (314 nm), the TiO<sub>2</sub> colloidal spheres (black trace) did not present any bands in the visible range. On the other hand, the Au/TiO<sub>2</sub> (red trace) and Au/SiO<sub>2</sub> (blue trace) displayed bands centered at 535 and 530 nm, respectively, assigned to the dipole modes of the LSPR excitation from Au NPs.<sup>46</sup>

In the next step, we aimed at studying how the LSPR excitation affected the plasmonic catalytic activities in both Au/TiO<sub>2</sub> and Au/SiO<sub>2</sub> as a function of the reaction pathway. We focused on Au/TiO<sub>2</sub> (that enables metal-support charge transfer processes) and Au/SiO<sub>2</sub> (that does not enable metal-support charge transfer processes) as catalysts. Moreover, we chose the hydrogenation of 4-nitrophenol as a model reaction and BH<sub>4</sub><sup>-</sup>(aq) ions or H<sub>2</sub>(g) as the reducing agents aiming at two different reaction pathways for reduction reactions involving metal NPs as catalysts.<sup>47,48</sup> When BH<sub>4</sub><sup>-</sup>(aq) is employed as reducing agent, H<sup>-</sup>(aq) ions are transferred from the BH<sub>4</sub><sup>-</sup>(aq) to the NPs surface (leading to the formation of M-H bonds), which contributes to the further reduction steps. The H<sup>-</sup> is transferred to substrate molecules at the nanoparticle surface, which represents the rate-limiting step according to the Langmuir–Hinshelwood model.<sup>47,49,50</sup> In the case of H<sub>2</sub>(g), the rate-limiting step represents the cleavage of molecular hydrogen leading to the formation of M-H bonds as they interact with the metal surface.<sup>51</sup>

The effect of the LSPR-excitation over the conversion of 4-nitrophenol into 4-aminophenol using BH<sub>4</sub><sup>-</sup>(aq) as reducing agent was investigated as shown in **Figure 3.6**. We employed a conventional LED lamp as our excitation source (the light intensity corresponded to 3.2 mW cm<sup>-2</sup>). The obtained conversion in the absence of LSPR excitation is shown in **Figure 3.6A**. Here, TiO<sub>2</sub> colloidal spheres (black trace), Au/TiO<sub>2</sub> (red trace), and Au/SiO<sub>2</sub> (blue trace) were investigated as catalysts. A blank reaction (green trace) is also shown. While no significant conversion was detected for the blank reaction or in the presence of TiO<sub>2</sub>, both Au/TiO<sub>2</sub> and Au/SiO<sub>2</sub> catalysts were effective towards this transformation.

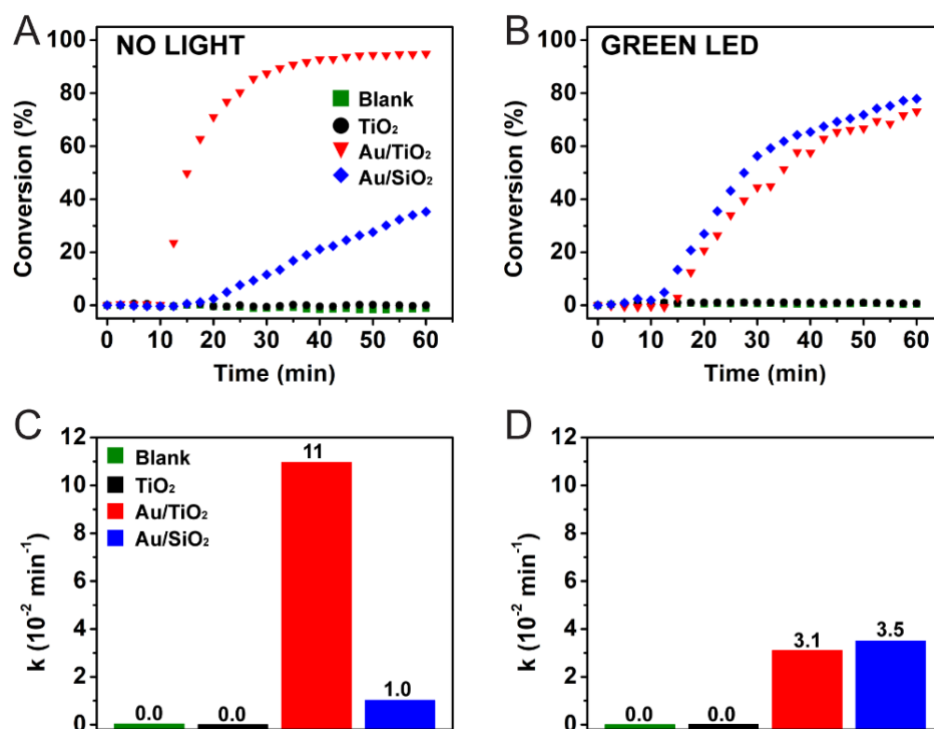


**Figure 3.6** – (A and B) conversion % as a function of time for the 4-nitrophenol hydrogenation by  $\text{BH}_4\text{-(aq)}$  catalyzed by  $\text{TiO}_2$  colloidal spheres (black trace),  $\text{Au/TiO}_2$  (red trace), and  $\text{Au/SiO}_2$  (blue trace). A blank reaction (in the absence of any catalyst) is also shown (green trace). In (A) and (B), the reaction was performed in the absence and presence of visible light excitation by a green LED, respectively. (C and D) show the pseudo-first-order rate constants ( $k$ ) obtained from (A and B), respectively.

In particular, the  $\text{Au/TiO}_2$  catalyst displayed higher conversion % relative to  $\text{Au/SiO}_2$  catalyst. After 30 min of reaction, the conversion of 4-nitrophenol reached 12 and 88 % for  $\text{Au/SiO}_2$  and  $\text{Au/TiO}_2$ , respectively. After 60 min of reaction, the reaction achieved 100 % conversion for  $\text{Au/TiO}_2$  catalyst, while 35 % conversion for  $\text{Au/SiO}_2$  NPs. It has been demonstrated that Au and Ag NPs supported on  $\text{TiO}_2$  can dissociate  $\text{H}_2$  into polar hydrogen species:  $\text{H}_{\delta^-}$  and  $\text{H}_{\delta^+}$ .<sup>52–54</sup> In our system, it is plausible that  $\text{H}_{\delta^-}$  would be formed at the Au surface (metal hydride) and  $\text{H}_{\delta^+}$  at  $\text{TiO}_2$  (bound to an oxygen atom) from  $\text{BH}_4\text{-(aq)}$ . This resulting  $\text{H}_{\delta^-}$  and  $\text{H}_{\delta^+}$  pair could improve the rate of the H transfer to polar bonds ( $\text{NO}_2$  group

in 4-nitrophenol), thus leading to higher reaction rates relative to the Au/SiO<sub>2</sub> catalysts in the absence of light excitation (in which the formation of the H<sub>δ</sub><sup>-</sup>/H<sub>δ</sub><sup>+</sup> pair is not favored).

Unexpectedly, by employing visible-light excitation with a green LED, we detected a decrease in the catalytic activities for Au/TiO<sub>2</sub> catalyst (red trace, **Figure 3.6B**) when compared to the reaction carried out in the absence of light excitation (**Figure 3.6A**). Under LSPR excitation, the conversion % corresponded to only 44 % after 30 min of reaction for Au/TiO<sub>2</sub>. After 60 min of reaction, the conversion reached 73 %. On the other hand, an opposite trend was observed for the Au/SiO<sub>2</sub> catalyst, with a significant enhancement in the conversion under visible-light illumination. In this case, the conversion reached 56 and 78 % after 30 and 60 min, respectively. These variations in catalytic activity as a function of LSPR-excitation for both Au/TiO<sub>2</sub> and Au/SiO<sub>2</sub> can be further illustrated by the pseudo-first-order rate constants ( $k$ ) calculated from **Figure 3.6A** and **B**, shown in **Figure 3.6C** and **D**, respectively. It can be observed that  $k$  varied from  $1.0 \times 10^{-2}$  to  $3.5 \times 10^{-2} \text{ min}^{-1}$  in Au/SiO<sub>2</sub> and from  $11 \times 10^{-2}$  to  $3.1 \times 10^{-2} \text{ min}^{-1}$  for Au/TiO<sub>2</sub> after LSPR excitation. This corresponds to an activity drop of about three times for Au/TiO<sub>2</sub> and an increase of about three times in activity for SiO<sub>2</sub>-Au NPs under LSPR excitation. These results indicate that, while the LSPR excitation led to a decrease in activity for the 4-nitrophenol hydrogenation using BH<sub>4</sub><sup>-</sup>(aq) as the reducing agent for Au/TiO<sub>2</sub>, an increase in activity was detected when Au/SiO<sub>2</sub> was employed as catalyst.

**Figure 3.7** depicts our proposed mechanism for the 4-nitrophenol hydrogenation by BH<sub>4</sub><sup>-</sup>(aq) based on different articles from the literature.<sup>55–58</sup>

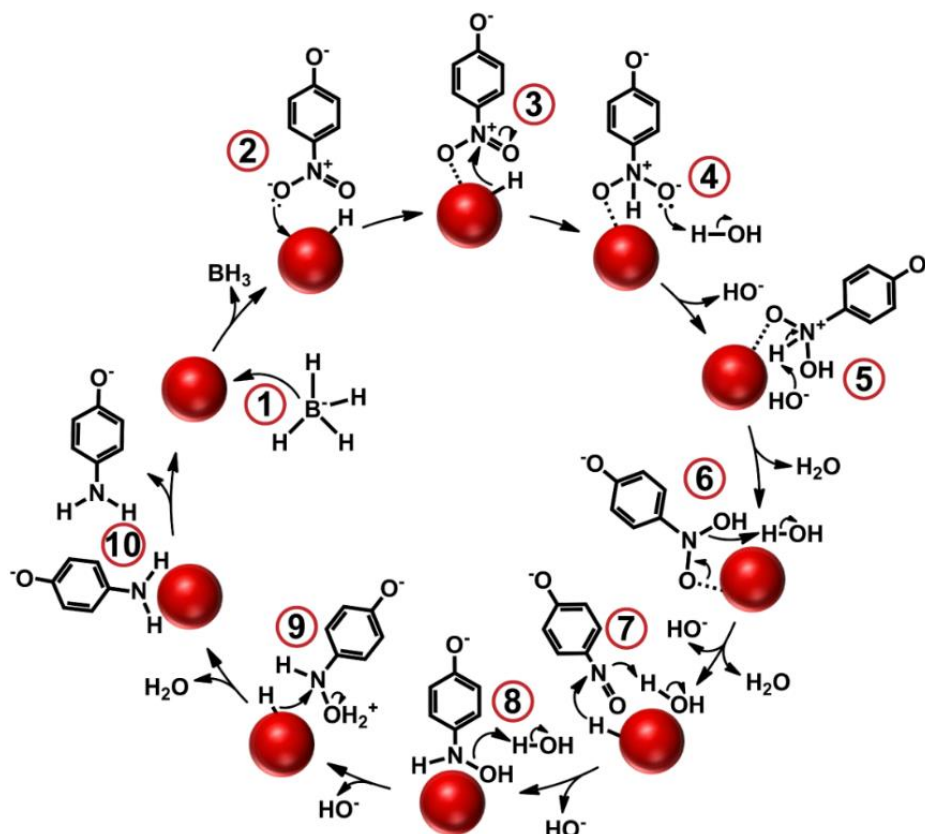


**Figure 3.7** – Proposed mechanism for the 4-nitrophenol hydrogenation by  $\text{BH}_4\text{-(aq)}$  catalyzed by metallic NPs.

**Figure 3.8A** and **B** show our proposed mechanism for the variations in activity under LSPR excitation for both Au/SiO<sub>2</sub> (**Figure 3.8A**) and Au/TiO<sub>2</sub> catalysts (**Figure 3.8B**). It is well-established that the LSPR excitation in plasmonic NPs leads to the generation of hot-electrons and holes.<sup>4,5</sup> These LSPR-excited hot-electrons can then be charge-transferred to adsorbed molecules or semiconductors in hybrids containing plasmonic NPs.<sup>59,60</sup> In Au/SiO<sub>2</sub>, no charge transfer of LSPR-excited hot electrons can take place from Au to SiO<sub>2</sub>. Therefore, the LSPR-excited hot electrons can be transferred to the lowest unoccupied adsorbate state (**Figure 3.8A**).<sup>61</sup> This leads to a formation of a transient adsorbate species (bond weakening and activation) which facilitates the transfer of H<sup>-</sup> ions at the metal surface to the adsorbate and thus accelerates the reaction. Although this mechanism has been described for several plasmonically enhanced transformations, its observation in hydrogenation remains limited.

Moreover, reports on the enhancement of the 4-nitrophenol reduction by  $\text{BH}_4^-$  under LSPR excitation have been mainly assigned to local heating due to plasmon decay.<sup>62,63</sup>

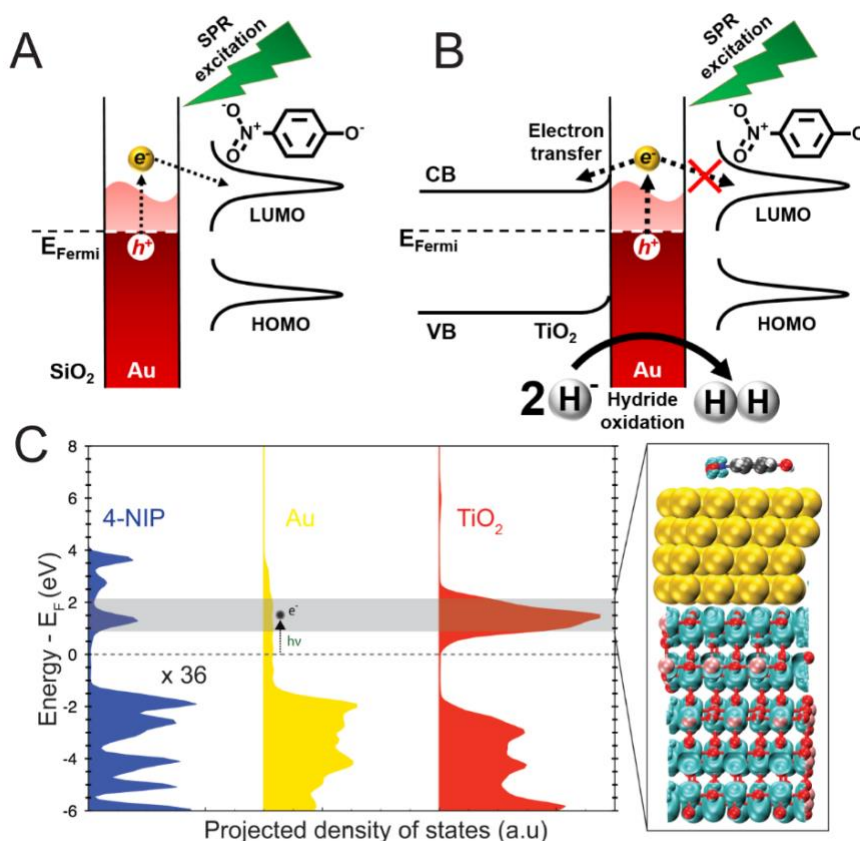


**Figure 3.8** – Detected increase in activity towards the 4-nitrophenol hydrogenation by  $\text{BH}_4^-$  (aq) catalyzed by Au/SiO<sub>2</sub> under LSPR excitation (A), and the detected decrease in activity when catalyzed by Au/TiO<sub>2</sub> under LSPR excitation (B). In Au/SiO<sub>2</sub> NPs, LSPR-excited hot electrons can be transferred to adsorbate LUMO orbitals accelerating the reaction rate. In Au/TiO<sub>2</sub>, LSPR-excited hot electrons are transferred from Au to the TiO<sub>2</sub> conduction band. The hydride species at the Au surface then get oxidized by the LSPR-generated holes, leading to the formation of H<sub>2</sub> and thus hampering the transfer of H<sup>-</sup> species from the Au surface to adsorbed 4-nitrophenolate species (rate-limiting step in the mechanism depicted in Figure 3). (C) DFT-calculated electronic structure of 4-nitrophenol adsorption on an Au/TiO<sub>2</sub> surface. Projected density of states of each component (4-nitrophenol, Au, TiO<sub>2</sub>) is shown to compare. The charge density plot shows the degenerate states of the conduction band of TiO<sub>2</sub> and the LUMO of 4-nitrophenol. The isosurface is set to  $0.12 \text{ e}/\text{\AA}^3$ .

However, we believe that this is not the case, otherwise, the same behavior would also be observed for Au/TiO<sub>2</sub>. Finally, it has been shown by theoretical simulations that plasmonic heating should not play any significant effects on our employed size, temperature, and laser intensity conditions.<sup>35</sup> In Au/TiO<sub>2</sub>, the LSPR-excited hot electrons generated at Au NPs can be transferred to the conduction band of TiO<sub>2</sub>.<sup>42–44</sup> Therefore, we propose that hot electrons are transferred from Au to TiO<sub>2</sub> following LSPR excitation and thus they do not become available for transfer to unoccupied adsorbate states (**Figure 3.8B**). **Figure 3.8C** shows the DFT-calculated electronic structure of 4-nitrophenol adsorbed on TiO<sub>2</sub>-supported Au layers. The LUMO orbital of the 4-nitrophenol molecule is located within 2 eV above the Fermi Level. The conduction band of TiO<sub>2</sub> is located at a similar energy window. Charge analysis within this energy range show states at both TiO<sub>2</sub> and the NO<sub>2</sub> group of the 4-nitrophenol. These degenerate states suggest that excited electrons in Au particles may have two interfacial charge transfer directions. The built-in electronic field at the Au/TiO<sub>2</sub> interface (**Figure 3.8B**) drives electron into TiO<sub>2</sub>, while the weak interaction between the molecule and Au hinders the electron injection into the molecular orbital.

Because of this directional electron transfer, reduction of the NO<sub>2</sub> group is thus not facilitated by the hot electrons. Instead, it is possible that the generated holes can also oxidize H<sup>-</sup> species bound at the Au NPs surface back to H<sub>2</sub>. This would lead to a decrease in the rate of the reaction as the transfer of H<sup>-</sup> species to adsorbed 4-nitrophenolate molecules represents the rate-limiting step for the 4-nitrophenol hydrogenation by BH<sub>4</sub><sup>-</sup> catalyzed by metal NPs according to the Langmuir-Hinshelwood mechanism as depicted in **Figure 3.7**.<sup>49,64</sup> In order to verify this hypothesis, we performed a control experiment in which the amount of H<sub>2(g)</sub> generated from the reaction was measured both in the absence and in the presence of visible light excitation. Interestingly, our results showed that the generation of H<sub>2</sub> from the reaction increased under green light excitation as shown in **Figure 3.9**, in agreement with the

mechanism depicted in **Figure 3.8B**. This experiment served as a tool to display any changes in hydrogen production from the interaction of borohydride with water. In the presence of a catalyst, less hydrogen is produced due to the adsorption of hydrides onto the catalyst surface.

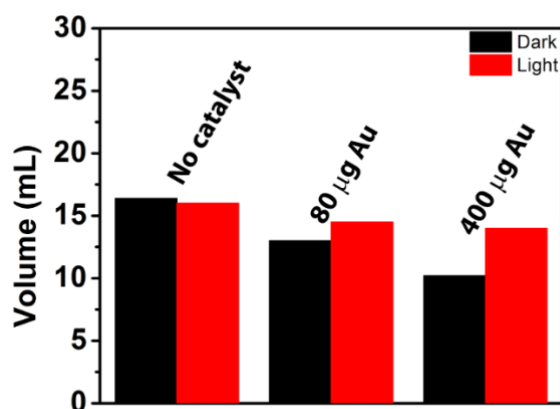


**Figure 3.9** – Volume of H<sub>2</sub>(g) produced from the addition of BH<sub>4</sub>-(aq) onto an aqueous suspension containing Au/TiO<sub>2</sub> NPs in the absence (black bars) or presence (red bars) of visible light excitation by a green LED lamp. When no catalyst is present, the volume of H<sub>2</sub>(g) is higher as a result of the adsorption of H<sup>-</sup> species at the Au surface. When the catalyst is present, the increase in the production of H<sub>2</sub>(g) is due to the oxidation of the H<sup>-</sup> species by the LSPR generated holes.

This proposed mechanism for the variation in catalytic activity following LSPR excitation in the Au/SiO<sub>2</sub> and Au/TiO<sub>2</sub> are also supported by our observations that, in Au NPs (no charge transfer to a support), p-nitrothiophenol (PNTTP) molecules can be reduced to p,p'-dimercaptoazobenzene (DMAB) under LSPR excitation due to the transfer of LSPR-excited hot electrons from Au to adsorbed PNTTP molecules. When Au/TiO<sub>2</sub> is employed as substrates, no reduction takes place as a result of the transfer of LSPR-excited hot electrons from Au to TiO<sub>2</sub>.<sup>65</sup>

We also performed the 4-nitrophenol hydrogenation using H<sub>2</sub>(g) as the reducing agent. Even though Au NPs have displayed high activities towards a myriad of reactions, relatively low activities towards hydrogenations using H<sub>2</sub>(g) as the hydrogen source have been



described.<sup>66</sup> **Figure 3.10** depicts the conversion % for the 4-nitrophenol hydrogenation by  $H_2$  employing  $TiO_2$ ,  $Au/TiO_2$ , and  $Au/SiO_2$  as catalysts (black, red, and blue traces, respectively).

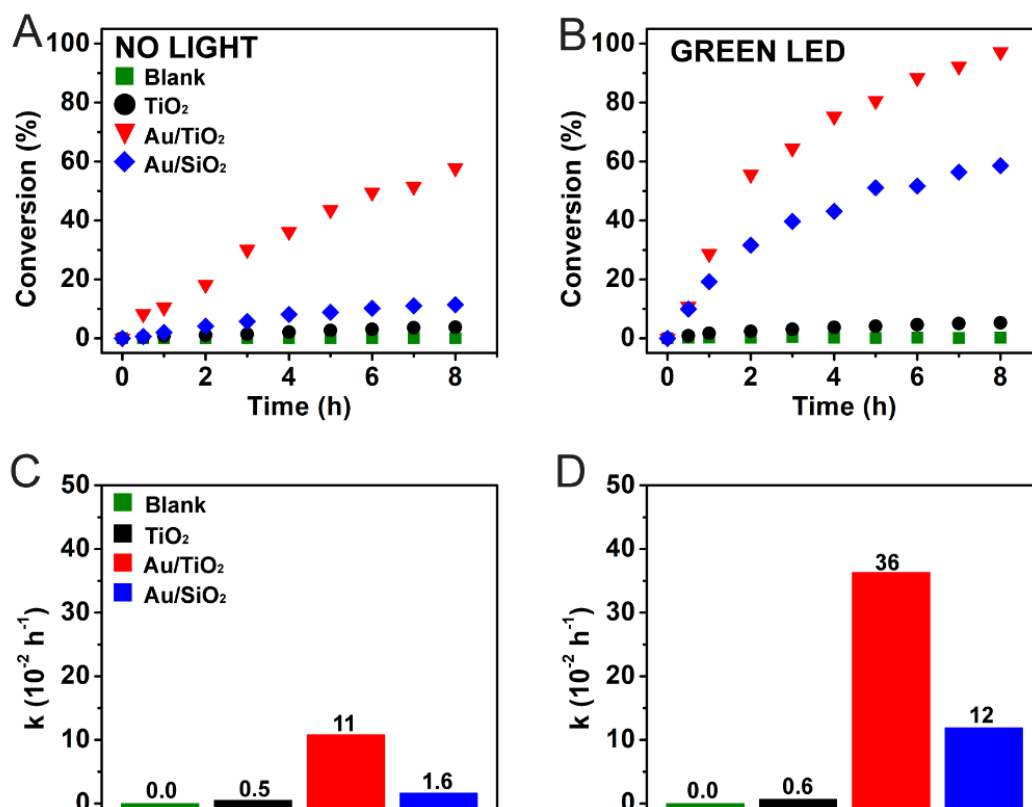


**Figure 3.10** – (A and B) conversion % as a function of time for 4-nitrophenol hydrogenation by  $H_{2(g)}$  catalyzed by  $TiO_2$  colloidal spheres (black trace),  $Au/TiO_2$  (red trace), and  $Au/SiO_2$  (blue trace). A blank reaction (in the absence of any catalyst) is also shown (green trace). In (A), the reaction was performed in the absence of visible light excitation (conventional catalysis), while in (B) the reaction was performed under a green light excitation (plasmonic catalysis). (C and D) show the pseudo-first-order rate constants ( $k$ ) obtained from (A and B), respectively.

A blank reaction is also depicted as the green trace. In the absence of LSPR-excitation (**Figure 3.10A**), no significant conversion was detected for both blank reaction and  $TiO_2$  colloidal spheres. However, the conversion percentages for  $Au/TiO_2$  were higher relative to  $Au/SiO_2$ . Specifically, after 8h, the conversion % corresponded to 58, and 11 % for  $Au/TiO_2$  and  $Au/SiO_2$ , respectively. The higher catalytic activity of the  $Au/TiO_2$  is assigned to the

promotional effect of the TiO<sub>2</sub> support as described for the reduction employing BH<sub>4</sub><sup>-</sup>(aq), in which metal support-interactions can induce the heterolytic H<sub>2</sub> cleavage into H<sup>δ-</sup>/H<sup>δ+</sup> pairs, and thus favor the reaction.<sup>29,48,53,54,67,68</sup>

The conversion % for both Au/SiO<sub>2</sub> and Au/TiO<sub>2</sub> increased when the reaction was carried out under visible light illumination (green led, **Figure 3.10B**). Specifically, the conversion after 8h of reaction corresponded to 97 and 59 % for Au/TiO<sub>2</sub> and Au/SiO<sub>2</sub>, respectively. These variations in catalytic activity can also be rationalized by analyzing the pseudo-first-order rate constants (*k*) depicted in **Figure 3.10C** and **D** that were calculated from the data shown in **Figure 3.10A** and **B**, respectively. Here, the *k* values increased from 11×10<sup>-2</sup> to 36×10<sup>-2</sup> h<sup>-1</sup> and from 1.6×10<sup>-2</sup> to 12×10<sup>-2</sup> h<sup>-1</sup> after visible light excitation (green led) for the Au/TiO<sub>2</sub> and Au/SiO<sub>2</sub>, respectively. This corresponds to an increase of about three and seven times in catalytic activity, respectively, under visible light excitation.

The mechanism for the increase of activities under LSPR excitation for the reduction of 4-nitrophenol by H<sub>2(g)</sub> is depicted in **Figure 3.11**.

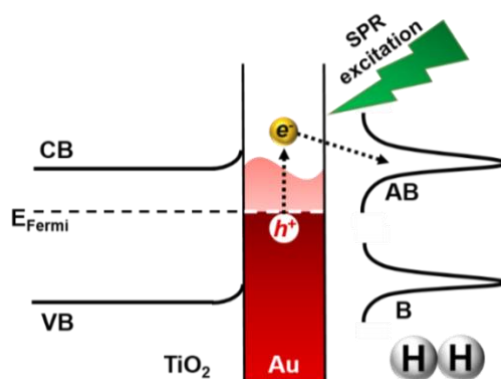


**Figure 3.11** – (A) Proposed mechanism for the detected increase in activity towards 4-nitrophenol hydrogenation by H<sub>2(g)</sub> catalyzed by Au/TiO<sub>2</sub> NPs under LSPR excitation. In this case, LSPR-excited hot electrons are transferred from Au NPs the antibonding orbital of H<sub>2</sub>. This favors the generation of hydride species at the surface and improved 4-nitrophenol hydrogenation compared to the reaction carried out in the absence of LSPR excitation.

In fact, it has been demonstrated that the LSPR excitation in Au NPs supported both on TiO<sub>2</sub> and SiO<sub>2</sub> lead to an increase in the rate of hydrogen dissociation. This phenomenon has been assigned, both experimentally and theoretically, to the transfer of LSPR-excited hot electrons from Au NPs to the H<sub>2</sub> anti-bonding orbital.<sup>35,36</sup> This aids the H<sub>2</sub> splitting at the surface and thus increase the reaction rates. It is important to note that in hydrogenations involving H<sub>2</sub>, the H<sub>2</sub> splitting at the surface is usually the rate-limiting step.<sup>47,49</sup> Another important observation is that the relative increase in the conversion percentage under LSPR excitation was observed for Au/SiO<sub>2</sub> relative to Au/TiO<sub>2</sub>. In the Au/TiO<sub>2</sub>, the presence of a Schottky barrier may also enable the transfer of LSPR-excited hot electrons to the TiO<sub>2</sub> conduction band, reducing the number of hot electrons available for transfer to the H<sub>2</sub> antibonding orbitals.

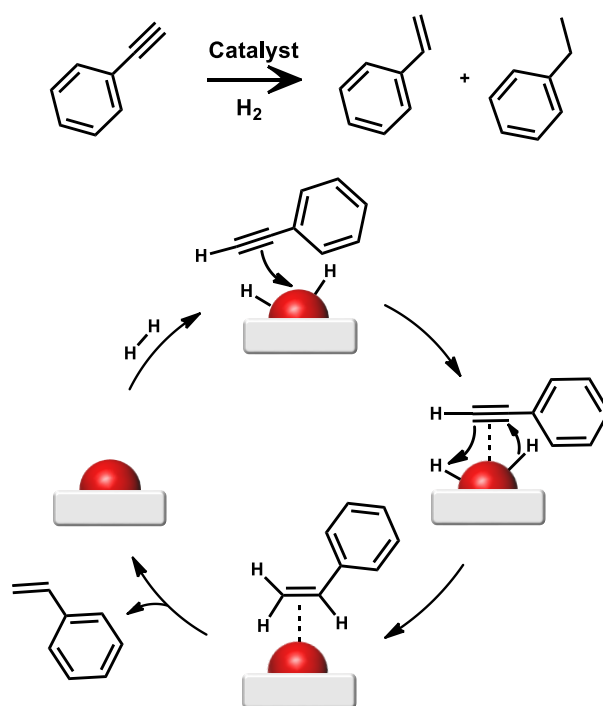


**Figure 3.12** – Hydrogenation of phenylacetylene and proposed mechanism catalyzed by Au/TiO<sub>2</sub>. This reaction could produce styrene and ethylbenzene as products, thus displaying the importance of the semi-hydrogenation of phenylacetylene and therefore the selectivity of the employed catalyst.

This principle (LSPR-enhanced hydrogenation in the presence of  $H_2$ ) can also be put to work towards achieving higher catalytic activities towards the hydrogenation of other molecules. For instance, we employed the aforementioned materials on the catalytic and photocatalytic hydrogenation of phenylacetylene using  $H_2$  as reducing agent. **Figure 3.12** shows the mechanism and possible products for this reaction.<sup>69</sup> We also evaluated the materials under LSPR excitation and compared both their activity and selectivity towards styrene. For these reactions, the same  $Au/TiO_2$ ,  $Au/SiO_2$ , and  $TiO_2$  materials were employed under 6 bar of  $H_2$  pressure at  $100^\circ C$ . **Figure 3.13** displays the results of conversion and selectivity for all three materials under no light illumination (**Figure 3.13A**) and under green light irradiation (**Figure 3.13B**). Even after properly cleaning the reactors, the blank reaction (green bar) produced a small conversion under both conditions, which could be attributed to the pressure and temperature onto the molecules, and since the conversions were both close to 1.5% and selectivities close to 54%, we can infer that it was a systematic error.

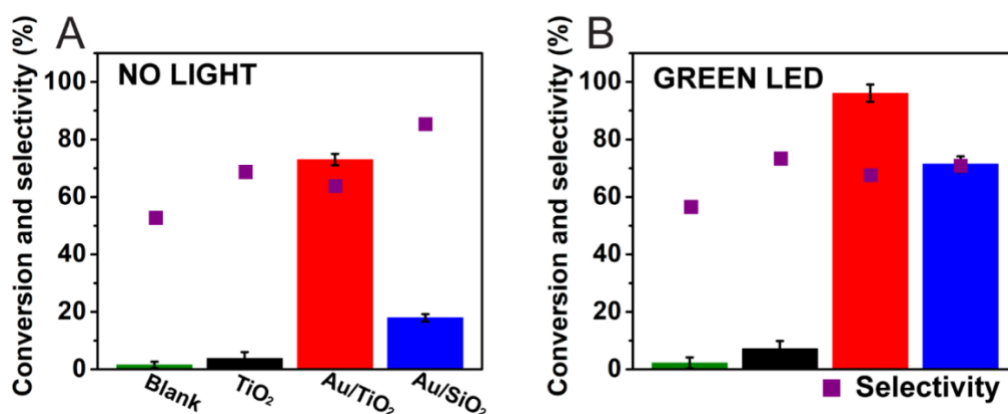


**Figure 3.13** – (A - B) conversion % after 5 hours of reaction for phenylacetylene hydrogenation under 6 bar of  $H_{2(g)}$  in ethanol at  $100^\circ C$  catalyzed by  $TiO_2$  colloidal spheres (black bar),  $Au/TiO_2$  (red bar), and  $Au/SiO_2$  (blue bar). A blank reaction (in the absence of any catalyst) is also shown (green bar). The purple squares indicate the selectivity for styrene. In (A), the reaction was performed in the absence of visible light excitation (conventional catalysis), while in (B) the reaction was performed under green light excitation from a LED lamp.

For the reaction employing  $\text{TiO}_2$  as catalyst (black bar), the increase on conversion when green light is shone is not very significant since it raises from  $4.1 \pm 2.0\%$  to  $6.8 \pm 3.1\%$ , that difference could be attributed as error. Although for the sample employing  $\text{Au/TiO}_2$  (red bar), a clear difference can be seen, with the conversion increasing from  $73.0 \pm 2.0\%$  under no light irradiation to  $96.1 \pm 3.0\%$  under green light and the selectivity suffered no significant changes ( $\approx 65\%$ ). As before mentioned, this could be attributed to the higher number of  $\text{H}_2$  molecules split under plasmonic excitation, which can thus lead to a higher conversion. As for the  $\text{Au/SiO}_2$  (blue bar), the increase was even greater, going from  $17.9 \pm 1.3\%$  under no light irradiation to  $71.4 \pm 2.7\%$  under green light, although the selectivity towards styrene decreased from  $85.3\%$  to  $70.8\%$ , a difference that could be also attributed to the higher rate of  $\text{H}_2$  splitting, which on its turn can further hydrogenate styrene to ethylbenzene if bound to active sites.

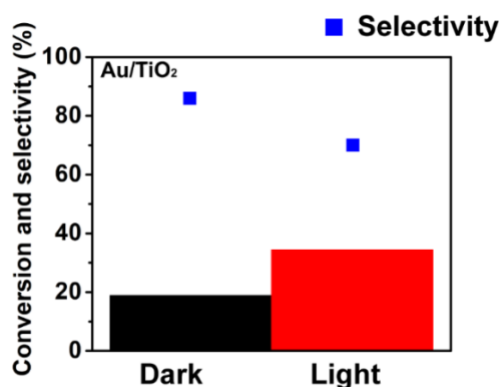


**Figure 3.14** – Conversion % of phenylacetylene for the hydrogenation reaction after pressurizing the reactor with 6 bar of  $\text{H}_{2(g)}$  for 5 hours at  $100\text{ }^{\circ}\text{C}$ , without phenylacetylene, under no visible light excitation (black bar) and under green light excitation (red bar). The blue square indicates selectivity towards styrene. The mixture was degasified with for 30 minutes and the substrate was added under  $\text{N}_2$  atmosphere. After the addition, reactions were allowed to occur for 5 hours at  $100\text{ }^{\circ}\text{C}$ .

In order to further prove that hydrogen splitting was being enhanced under plasmon excitation we performed a control experiment in which the  $\text{Au/TiO}_2$  catalyst was initially

submitted to reaction conditions without the presence of the substrate in the medium to generate adsorbed hydrogen species (Figure 3.14). For this, we employed the same reaction conditions as aforementioned, 6 bar of hydrogen, 100°C for 5 hours. Afterwards, the pressure was relieved, nitrogen was bubbled for 30 minutes to remove dissolved hydrogen and the atmosphere was then substituted to nitrogen.

This procedure proves that under green LED excitation, the system grants higher H<sub>2</sub> splitting and thus enhances hydrogenation reactions. As for selectivity, light excitation lowered the selectivity towards styrene, which could be due to the higher number of hydrides on the surface of the catalyst, which would grant the catalyst the possibility of further hydrogenating the substrates if adsorbed onto the surface.<sup>70</sup> To further illustrate the high activities and versatility of the LSPR-excitation, we also performed the reduction of 4-nitrophenol and phenylacetylene by H<sub>2(g)</sub> at room temperature employing Au/TiO<sub>2</sub> catalyst (Figure 3.15).

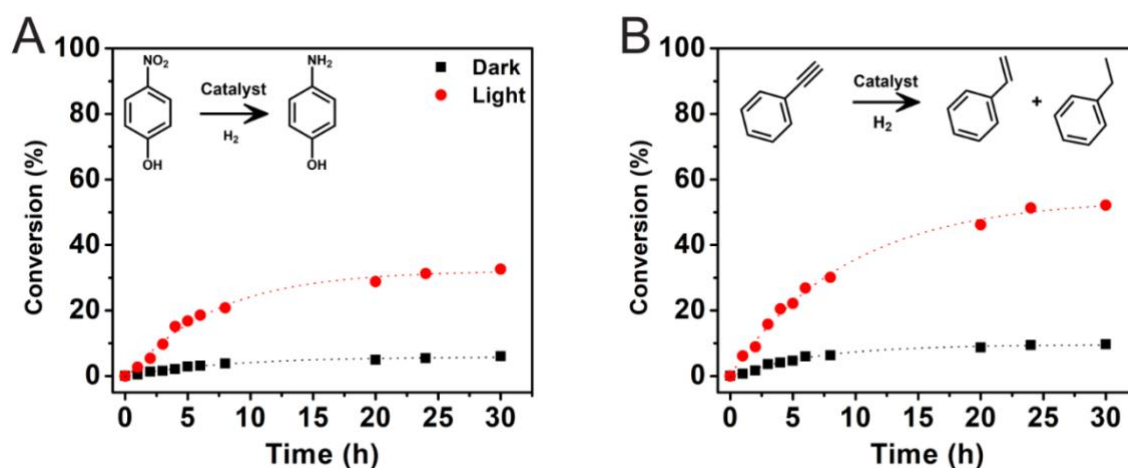


**Figure 3.15** – Conversion % as a function of time for (A) 4-nitrophenol or (B) phenylacetylene hydrogenation by H<sub>2(g)</sub> catalyzed by Au/TiO<sub>2</sub> in the absence of visible light excitation (black trace) and under light excitation by a green (red trace). Reactions performed at 20 °C.

While no conversion was detected in the absence of light excitation, significant conversions were detected under the same conditions under visible-light (green) illumination. As seen on this kinetic study, the enhancement is different depending on the substrate that employed, even though the catalyst and conditions are the same, the enhancement is further seen on alkynes (**Figure 3.15B**) than on the nitro-compound (**Figure 3.15A**), which could be related to the more complex mechanism observed for the nitro-compound (**Figure 3.7**) when compared to the alkyne reduction (**Figure 3.12**), although this would need further study to be proven.

### 3.4 – Conclusions

In summary, by employing hydrogenation reactions as a model proof-of-concept transformation, we found that the plasmonic catalytic activity displayed a reaction pathway dependent behavior. Both positive (catalytic enhancement) and negative (reaction rate suppression) could be detected under visible light illumination employing Au NPs supported on TiO<sub>2</sub> and SiO<sub>2</sub> as plasmonic catalysts. We found that both the nature of the reducing agent and the occurrence of charge-transfer processes at the interface were responsible for the detected variations in plasmonic catalytic activities. The results described herein shed important insights in the field of plasmonic catalysis, in which activity and performance can display reaction pathway dependent behavior. It is noteworthy that other types of transformations may also display a similar trend and deserve further investigation. We believe that this knowledge will pave the way for the improved design of plasmonically-enhanced and greener chemical processes.



### 3.5 – References

- 1     Barbosa ECM, Fiorio JL, Mou T, Wang B, Rossi LM, Camargo PHC. Reaction Pathway Dependence in Plasmonic Catalysis: Hydrogenation as a Model Molecular Transformation. *Chem - A Eur J* 2018; **24**: 12330–12339.
- 2     Aslam U, Chavez S, Linic S. Controlling energy flow in multimetallic nanostructures for plasmonic catalysis. *Nat Nanotechnol* 2017; **12**: 1000–1005.
- 3     Linic S, Christopher P, Ingram DB. Plasmonic-metal nanostructures for efficient conversion of solar to chemical energy. *Nat Mater* 2011; **10**: 911–921.
- 4     Linic S, Aslam U, Boerigter C, Morabito M. Photochemical transformations on plasmonic metal nanoparticles. *Nat Mater* 2015; **14**: 567–576.
- 5     Baffou G, Quidant R. Nanoplasmonics for chemistry. *Chem Soc Rev* 2014; **43**: 3898–3907.
- 6     Hao C-H, Guo X-N, Pan Y-T, Chen S, Jiao Z, Yang H *et al.* Visible-Light-Driven Selective Photocatalytic Hydrogenation of Cinnamaldehyde over Au/SiC Catalysts. *J Am Chem Soc* 2016; **138**: 9361–9364.
- 7     Ingram DB, Linic S. Water splitting on composite plasmonic-metal/semiconductor photoelectrodes: Evidence for selective plasmon-induced formation of charge carriers near the semiconductor surface. *J Am Chem Soc* 2011; **133**: 5202–5205.
- 8     Wang JL, Ando RA, Camargo PHC. Investigating the plasmon-mediated catalytic activity of agau nanoparticles as a function of composition: Are two metals better than one? *ACS Catal* 2014; **4**: 3815–3819.
- 9     Shown I, Hsu H-C, Chang Y-C, Lin C-H, Roy PK, Ganguly A *et al.* Highly Efficient Visible Light Photocatalytic Reduction of CO<sub>2</sub> to Hydrocarbon Fuels by Cu-Nanoparticle Decorated Graphene Oxide. *Nano Lett* 2014; **14**: 6097–103.
- 10    Sugawa K, Tsunenari N, Takeda H, Fujiwara S, Akiyama T, Honda J *et al.*

- Development of Plasmonic Cu<sub>2</sub>O/Cu Composite Arrays as Visible- and Near-Infrared-Light-Driven Plasmonic Photocatalysts. *Langmuir* 2017; **33**: 5685–5695.
- 11 Knight MW, King NS, Liu L, Everitt HO, Nordlander P, Halas NJ. Aluminum for plasmonics. *ACS Nano* 2014; **8**: 834–840.
  - 12 Zhou L, Zhang C, McClain MJ, Manjavacas A, Krauter CM, Tian S *et al.* Aluminum Nanocrystals as a Plasmonic Photocatalyst for Hydrogen Dissociation. *Nano Lett* 2016; **16**: 1478–1484.
  - 13 Cushing SK, Wu N. Progress and Perspectives of Plasmon-Enhanced Solar Energy Conversion. *J Phys Chem Lett* 2016; **7**: 666–675.
  - 14 Peiris S, McMurtrie J, Zhu H-Y. Metal nanoparticle photocatalysts: emerging processes for green organic synthesis. *Catal Sci Technol* 2016; **6**: 320–338.
  - 15 Kim Y, Dumett Torres D, Jain PK. Activation Energies of Plasmonic Catalysts. *Nano Lett* 2016; **16**: 3399–3407.
  - 16 Naldoni A, Riboni F, Guler U, Boltasseva A, Shalaev VM, Kildishev A V. Solar-Powered Plasmon-Enhanced Heterogeneous Catalysis. *Nanophotonics* 2016; **5**: 112–133.
  - 17 Kim M, Lin M, Son J, Xu H, Nam JM. Hot-Electron-Mediated Photochemical Reactions: Principles, Recent Advances, and Challenges. *Adv Opt Mater* 2017; **1700004**: 1–21.
  - 18 Rahman DS, Ghosh SK. Manipulating Electron Transfer in Hybrid ZnO–Au Nanostructures: Size of Gold Matters. *J Phys Chem C* 2016; **120**: 14906–14917.
  - 19 Kumar D, Lee A, Lee T, Lim M, Lim D-K. Ultrafast and Efficient Transport of Hot Plasmonic Electrons by Graphene for Pt Free, Highly Efficient Visible-Light Responsive Photocatalyst. *Nano Lett* 2016; **16**: 1760–1767.
  - 20 Hughes MD, Xu Y-J, Jenkins P, McMorn P, Landon P, Enache DI *et al.* Tunable gold

- catalysts for selective hydrocarbon oxidation under mild conditions. *Nature* 2005; **437**: 1132–1135.
- 21 Robatjazi H, Zhao H, Swearer DF, Hogan NJ, Zhou L, Alabastri A *et al.* Plasmon-induced selective carbon dioxide conversion on earth-abundant aluminum-cuprous oxide antenna-reactor nanoparticles. *Nat Commun* 2017; **8**: 27.
- 22 Shao L, Huang X, Teschner D, Zhang W. Gold Supported on Graphene Oxide: An Active and Selective Catalyst for Phenylacetylene Hydrogenations at Low Temperatures. *ACS Catal* 2014; **4**: 2369–2373.
- 23 Lim B, Wang J, Camargo PHC, Cobley CM, Kim MJ, Xia Y. Twin-Induced Growth of Palladium-Platinum Alloy Nanocrystals. *Angew Chemie Int Ed* 2009; **48**: 6304–6308.
- 24 Rodrigues TS, da Silva AGM, de Moura ABL, Freitas IG, Camargo PHC. Rational design of plasmonic catalysts: matching the surface plasmon resonance with lamp emission spectra for improved performance in AgAu nanorings. *RSC Adv* 2016; **6**: 62286–62290.
- 25 da Silva AGM, Rodrigues TS, Correia VG, Alves T V., Alves RS, Ando RA *et al.* Plasmonic Nanorattles as Next-Generation Catalysts for Surface Plasmon Resonance-Mediated Oxidations Promoted by Activated Oxygen. *Angew Chemie Int Ed* 2016; **55**: 7111–7115.
- 26 Papa L, de Freitas IC, Geonmonond RS, de Aquino CB, Pieretti JC, Domingues SH *et al.* Supports matter: unraveling the role of charge transfer in the plasmonic catalytic activity of silver nanoparticles. *J Mater Chem A* 2017; **5**: 11720–11729.
- 27 Wang J, Alves T V., Trindade FJ, de Aquino CB, Pieretti JC, Domingues SH *et al.* Theoretical Design and Experimental Realization of Quasi Single Electron Enhancement in Plasmonic Catalysis. *Angew Chemie Int Ed* 2015; **54**: 14427–14431.
- 28 Besson M, Gallezot P, Pinel C. Conversion of Biomass into Chemicals over Metal

- Catalysts. *Chem Rev* 2014; **114**: 1827–1870.
- 29 Corma A, Serna P. Chemoselective Hydrogenation of Nitro Compounds with Supported Gold Catalysts. *Science* (80- ) 2006; **313**: 332–334.
  - 30 Vilé G, Colussi S, Krumeich F, Trovarelli A, Pérez-Ramírez J. Opposite Face Sensitivity of CeO<sub>2</sub> in Hydrogenation and Oxidation Catalysis. *Angew Chemie Int Ed* 2014; **53**: 12069–12072.
  - 31 Fiorio JL, López N, Rossi LM. Gold–Ligand-Catalyzed Selective Hydrogenation of Alkynes into cis -Alkenes via H<sub>2</sub> Heterolytic Activation by Frustrated Lewis Pairs. *ACS Catal* 2017; **7**: 2973–2980.
  - 32 Wang D, Astruc D. The Golden Age of Transfer Hydrogenation. *Chem Rev* 2015; **115**: 6621–6686.
  - 33 Somorjai GA, Rioux RM. High technology catalysts towards 100% selectivity. *Catal Today* 2005; **100**: 201–215.
  - 34 Xia Y, Xiong Y, Lim B, Skrabalak SE. Shape-controlled synthesis of metal nanocrystals: Simple chemistry meets complex physics? *Angew Chemie Int Ed* 2009; **48**: 60–103.
  - 35 Mukherjee S, Libisch F, Large N, Neumann O, Brown L V, Cheng J *et al.* Hot Electrons Do the Impossible: Plasmon-Induced Dissociation of H<sub>2</sub> on Au. *Nano Lett* 2013; **13**: 240–247.
  - 36 Mukherjee S, Zhou L, Goodman AM, Large N, Ayala-Orozco C, Zhang Y *et al.* Hot-Electron-Induced Dissociation of H<sub>2</sub> on Gold Nanoparticles Supported on SiO<sub>2</sub>. *J Am Chem Soc* 2014; **136**: 64–67.
  - 37 Long R, Rao Z, Mao K, Li Y, Zhang C, Liu Q *et al.* Efficient Coupling of Solar Energy to Catalytic Hydrogenation by Using Well-Designed Palladium Nanostructures. *Angew Chemie Int Ed* 2015; **54**: 2425–2430.

- 38 Damato TC, de Oliveira CCS, Ando RA, Camargo PHC. A Facile Approach to TiO<sub>2</sub> Colloidal Spheres Decorated with Au Nanoparticles Displaying Well-Defined Sizes and Uniform Dispersion. *Langmuir* 2013; **29**: 1642–1649.
- 39 Yu HK, Eun TH, Yi GR, Yang SM. Multi-faceted titanium glycolate and titania structures from room-temperature polyol process. *J Colloid Interface Sci* 2007; **316**: 175–182.
- 40 Jiang X, Herricks T, Xia Y. Monodispersed spherical colloids of titania: Synthesis, characterization, and crystallization. *Adv Mater* 2003; **15**: 1205–1209.
- 41 Ou Y, Lin J-D, Zou H-M, Liao D-W. Effects of surface modification of TiO<sub>2</sub> with ascorbic acid on photocatalytic decolorization of an azo dye reactions and mechanisms. *J Mol Catal A Chem* 2005; **241**: 59–64.
- 42 Grätzel M. Photoelectrochemical cells. *Nature* 2001; **414**: 338–344.
- 43 Tsukamoto D, Shiraishi Y, Sugano Y, Ichikawa S, Tanaka S, Hirai T. Gold nanoparticles located at the interface of anatase/rutile TiO<sub>2</sub> particles as active plasmonic photocatalysts for aerobic oxidation. *J Am Chem Soc* 2012; **134**: 6309–6315.
- 44 Panayotov DA, Frenkel AI, Morris JR. Catalysis and Photocatalysis by Nanoscale Au/TiO<sub>2</sub>: Perspectives for Renewable Energy. *ACS Energy Lett* 2017; **2**: 1223–1231.
- 45 Dong R, Zhang Q, Gao W, Pei A, Ren B. Highly efficient light-driven TiO<sub>2</sub>-Au Janus Micromotors. *ACS Nano* 2016; **10**: 839–844.
- 46 Willets KA, Van Duyne RP. Localized Surface Plasmon Resonance Spectroscopy and Sensing. *Annu Rev Phys Chem* 2007; **58**: 267–297.
- 47 Hervés P, Pérez-Lorenzo M, Liz-Marzán LM, Dzubiella J, Lu Y, Ballauff M. Catalysis by metallic nanoparticles in aqueous solution: model reactions. *Chem Soc Rev* 2012; **41**: 5577.
- 48 Corma A, Concepción P, Serna P. A Different Reaction Pathway for the Reduction of

- Aromatic Nitro Compounds on Gold Catalysts. *Angew Chemie Int Ed* 2007; **46**: 7266–7269.
- 49 Aditya T, Pal A, Pal T. Nitroarene reduction: a trusted model reaction to test nanoparticle catalysts. *Chem Commun* 2015; **51**: 9410–9431.
- 50 Guella G, Patton B, Miotello A. Kinetic Features of the Platinum Catalyzed Hydrolysis of Sodium Borohydride from  $^{11}\text{B}$  NMR Measurements. *J Phys Chem C* 2007; **111**: 18744–18750.
- 51 Fujitani T, Nakamura I, Akita T, Okumura M, Haruta M. Hydrogen Dissociation by Gold Clusters. *Angew Chemie Int Ed* 2009; **48**: 9515–9518.
- 52 Zhang S, Huang Z-Q, Ma Y, Gao W, Li J, Cao F *et al.* Solid frustrated-Lewis-pair catalysts constructed by regulations on surface defects of porous nanorods of  $\text{CeO}_2$ . *Nat Commun* 2017; **8**: 15266.
- 53 Ren D, He L, Yu L, Ding R, Liu Y, Cao Y *et al.* An Unusual Chemoselective Hydrogenation of Quinoline Compounds Using Supported Gold Catalysts. *J Am Chem Soc* 2012; **134**: 17592–17598.
- 54 Mitsudome T, Yamamoto M, Maeno Z, Mizugaki T, Jitsukawa K, Kaneda K. One-step Synthesis of Core-Gold/Shell-Ceria Nanomaterial and Its Catalysis for Highly Selective Semihydrogenation of Alkynes. *J Am Chem Soc* 2015; **137**: 13452–13455.
- 55 Devi LB, Mandal AB. Self-assembly of Ag nanoparticles using hydroxypropyl cyclodextrin: Synthesis, characterisation and application for the catalytic reduction of p-nitrophenol. *RSC Adv* 2013; **3**: 5238–5253.
- 56 Ansar SM, Kitchens CL. Impact of Gold Nanoparticle Stabilizing Ligands on the Colloidal Catalytic Reduction of 4-Nitrophenol. *ACS Catal* 2016; **6**: 5553–5560.
- 57 Gu S, Wunder S, Lu Y, Ballauff M, Fenger R, Rademann K *et al.* Kinetic analysis of the catalytic reduction of 4-nitrophenol by metallic nanoparticles. *J Phys Chem C* 2014;

**118:** 18618–18625.

- 58 Li M, Chen G. Revisiting catalytic model reaction p-nitrophenol/NaBH<sub>4</sub> using metallic nanoparticles coated on polymeric spheres. *Nanoscale* 2013; **5**: 11919.
- 59 Boerigter C, Aslam U, Linic S. Mechanism of Charge Transfer from Plasmonic Nanostructures to Chemically Attached Materials. *ACS Nano* 2016; **10**: 6108–6115.
- 60 Brongersma ML, Halas NJ, Nordlander P. Plasmon-induced hot carrier science and technology. *Nat Nanotechnol* 2015; **10**: 25–34.
- 61 Boerigter C, Campana R, Morabito M, Linic S. Evidence and implications of direct charge excitation as the dominant mechanism in plasmon-mediated photocatalysis. *Nat Commun* 2016; **7**: 10545.
- 62 Gao S, Zhang Z, Liu K, Dong B. Direct evidence of plasmonic enhancement on catalytic reduction of 4-nitrophenol over silver nanoparticles supported on flexible fibrous networks. *Appl Catal B Environ* 2016; **188**: 245–252.
- 63 Hajfathalian M, Gilroy KD, Yaghoubzade A, Sundar A, Tan T, Hughes RA *et al.* Photocatalytic Enhancements to the Reduction of 4-Nitrophenol by Resonantly Excited Triangular Gold-Copper Nanostructures. *J Phys Chem C* 2015; **119**: 17308–17315.
- 64 Schlather AE, Manjavacas A, Lauchner A, Marangoni VS, DeSantis CJ, Nordlander P *et al.* Hot Hole Photoelectrochemistry on Au@SiO<sub>2</sub>@Au Nanoparticles. *J Phys Chem Lett* 2017; **8**: 2060–2067.
- 65 Wang J, Ando RA, Camargo PHC. Controlling the Selectivity of the Surface Plasmon Resonance Mediated Oxidation of p -Aminothiophenol on Au Nanoparticles by Charge Transfer from UV-excited TiO<sub>2</sub>. *Angew Chemie Int Ed* 2015; **54**: 6909–6912.
- 66 Stratakis M, Garcia H. Catalysis by Supported Gold Nanoparticles: Beyond Aerobic Oxidative Processes. *Chem Rev* 2012; **112**: 4469–4506.
- 67 Boronat M, Illas F, Corma A. Active Sites for H<sub>2</sub> Adsorption and Activation in

- Au/TiO<sub>2</sub> and the Role of the Support †. *J Phys Chem A* 2009; **113**: 3750–3757.
- 68 Boronat M, Concepción P, Corma A, González S, Illas F, Serna P. A molecular mechanism for the chemoselective hydrogenation of substituted nitroaromatics with nanoparticles of gold on TiO<sub>2</sub> catalysts: A cooperative effect between gold and the support. *J Am Chem Soc* 2007; **129**: 16230–16237.
- 69 Li S-S, Tao L, Wang F-Z-R, Liu Y-M, Cao Y. Heterogeneous Gold-Catalyzed Selective Semireduction of Alkynes using Formic Acid as Hydrogen Source. *Adv Synth Catal* 2016; **358**: 1410–1416.
- 70 Quiroz J, Barbosa ECM, Araujo TP, Fiorio JL, Wang YC, Zou YC *et al.* Controlling Reaction Selectivity over Hybrid Plasmonic Nanocatalysts. *Nano Lett* 2018; **18**: 7289–7297.



## **Chapter 4 – Platinum nanoparticles supported on Titania: An improved electrocatalyst towards the oxygen reduction reaction**

### **4.1 – Introduction**

This chapter can be found on the journal ACS Applied Energy Materials.<sup>1</sup>

The oxygen reduction reaction (ORR) is employed at the cathode in proton exchange membrane (PEM) fuel cells and contributes to the energy production of these devices.<sup>2,3</sup> Due to its sluggish kinetics, the ORR requires electrocatalysts based on platinum nanoparticles (Pt NPs) supported on high surface area materials.<sup>4,5</sup> However, due to the high costs and low abundance of Pt, the reduction in Pt loading or even developing Pt-free electrocatalysts represents an important challenge.<sup>6,7</sup> Recently, significant progress has been achieved in performance through the control over the Pt shape, size, composition (alloys and multimetallic systems), and structure (Pt-based nanostructures with hollow interiors).<sup>4,8</sup> Nevertheless, further understanding of the electrocatalytic enhancements are still required to meet cost/energy demands and enable the widespread application of these devices.<sup>9,10</sup>

In addition to the NPs physical and chemical parameters, the optimization over metal-support interactions can be employed to maximize electrocatalytic performance due to the generation of surface reactive sites.<sup>11–13</sup> In the context of the ORR, most supports are comprised of conductive carbon nanomaterials.<sup>7,14</sup> However, carbon supports usually corrode to form carbon dioxide, leading to the collapse and agglomeration of Pt NPs and thus the loss of activity in the longer term.<sup>15,16</sup> Therefore, the utilization of other supports is promising to improve both the stability and performances. Among the several promising materials as supports, titanium dioxide (TiO<sub>2</sub>) is resistant to corrosion, presents a low cost, is commercially available, and several protocols for the synthesis have been reported.<sup>17,18</sup> However, a major drawback is that the TiO<sub>2</sub> electrical conductivity must be enhanced to be

used as a support material. In this case, hybrid materials comprised of  $\text{TiO}_2$  and carbon have been proposed. This system combines the attractive features of both materials. Nevertheless, a deeper understanding of the effect of  $\text{TiO}_2$  as support over the detected ORR activities and stabilities is required.<sup>17,19</sup>

In this chapter, we developed electrocatalysts composed of Pt NPs supported on  $\text{TiO}_2$  microspheres, that were subsequently impregnated into conductive carbon (Vulcan) as model systems to investigate the effect of the Pt loading on  $\text{TiO}_2$  over the ORR activities and stability. The effect of Pt loading at the  $\text{TiO}_2$  surface, as well as the Pt/ $\text{TiO}_2$  loading on carbon, was investigated and benchmarked against the commercial Pt/C (E-TEK) material. We found that the loading of Pt and  $\text{TiO}_2$  played a central role over the exposure of reactive sites and thus to the ORR activities. This effect could be related to the generation of surface reactive groups, such as adsorbed oxygenated species, as a result of the optimized metal-support interactions.

## 4.2 – Experimental Section

### *Materials and Instrumentation:*

$\text{H}_2\text{PtCl}_6 \cdot 6\text{H}_2\text{O}$  (Chloroplatinic acid hexahydrate, Sigma-Aldrich), PVP (polyvinylpyrrolidone, Sigma-Aldrich, MW 55 000 g mol<sup>-1</sup>), EG (ethylene glycol, 99.5%, Synth),  $\text{C}_3\text{H}_6\text{O}$  (acetone, 99.5%, Synth),  $\text{C}_2\text{H}_4\text{O}_2$  (acetic acid, 99.7%, Vetec),  $\text{C}_6\text{H}_8\text{O}_6$  (ascorbic acid, 99.0%, Sigma-Aldrich),  $\text{Ti}(\text{OBu})_4$  (titanium butoxide, 97%, Sigma-Aldrich), Vulcan XC-72 Carbon (Cabot®),  $\text{H}_2\text{SO}_4$  (sulfuric acid, 70%, P.A. Synth), Nafion® (5 wt.%, Fluka), and Pt/C E-TEK 10 wt.% were used as received. All chemicals were analytical grade reagents and were used without further purification. Deionized water (18.2 MΩ) was used throughout the experiments.

### *Material analyses:*

Scanning electron microscopy (SEM) images were obtained using a JEOL microscope FEG-SEM JSM 6330F operated at 5 kV. The samples were prepared by drop-casting an aqueous suspension of the nanostructures on a Si wafer followed by drying under ambient conditions. Size distribution profile was determined by individually measuring the size of 200 particles from SEM images. High Resolution Transmission Electron Microscopy (HRTEM) images were obtained using a Tecnai FEI G20 operated at 200 kV. Samples were prepared by drop casting an alcoholic suspension of each particle in a carbon-coated copper grid followed by drying under ambient conditions.

The X-ray photoelectron spectroscopy (XPS) analyses were performed using a SPECSLAB II (Phoibos-Hsa 3500 150, 9 channeltrons) SPECS spectrometer, with an Al Kα source ( $E = 1486.6$  eV) working at 12 kV,  $E_{\text{pass}} = 40$  eV, with 0.2 eV energy step. The synthesized electrocatalysts were kept on stainless steel sample-holders and transported under inert atmosphere into the pre-chamber of the XPS staying under vacuum for 2 hours. The

residual pressure in the analysis chamber was of approximately  $1 \times 10^{-9}$  Torr. The binding energies (BE) of Pt 4f, Ti 2p, O 1s, and C 1s spectral peaks were adjusted using the C 1s peak as reference, placed at 284.5 eV, providing accuracy within  $\pm 0.2$  eV.

X-ray diffraction (XRD) data were obtained using a Rigaku - Miniflex equipment with  $\text{CuK}\alpha$  radiation of 1.5406 Å and the diffraction patterns were acquired in the range of  $2\theta = 10 - 80^\circ$  with a  $1^\circ \text{ min}^{-1}$  scanning speed. Pt atomic percentages were measured by inductively coupled plasma optical emission spectrometry (ICP-OES) using a Spectro Arcos equipment at IQ-USP analytical center facilities. Samples were prepared by digesting them using aqua regia at reflux for 2 hours at  $100^\circ\text{C}$ . After digestion, samples were diluted using distilled water.

*Syntheses:  $\text{TiO}_2$  colloidal spheres:*

The synthesis followed a previously reported procedure.<sup>20-22</sup> Typically,  $\text{Ti}(\text{OBu})_4$  (4 mL) were added dropwise to ethylene glycol (90 mL) and kept under vigorous stirring at room temperature for 8 hours. This mixture was then quickly poured into a mixture containing acetone (400 mL), deionized water (5 mL), and acetic acid (2 mL). Subsequently, the mixture was kept under stirring at room temperature for 2 hours followed by aging for 3 more hours. At this stage, titanium glycolate microspheres were formed. They were washed and isolated by successive rounds of centrifugation, removal of the supernatant, and re-suspension in ethanol. In the next step, deionized water (50 mL) was added to the solid material comprising titanium glycolate microspheres, the materials were re-suspended, and this mixture was kept under stirring at  $70^\circ\text{C}$  for 8 hours to produce  $\text{TiO}_2$  colloidal spheres. This material was washed and isolated by successive rounds of centrifugation, removal of the supernatant, and re-suspension with water and ethanol. The  $\text{TiO}_2$  colloidal spheres were then resuspended in deionized water (500 mL).

*Synthesis of Pt/TiO<sub>2</sub> via Pt seeded growth:*

TiO<sub>2</sub> microspheres (12 mg) suspended in deionized water (6 mL) were added to a mixture containing deionized water (12 mL), ascorbic acid (12 mg), and PVP (70 mg). This orange mixture was kept under stirring for 10 minutes at 90 °C and at this point, PtCl<sub>6</sub>2-(aq) (6 mL, 3.0 mmol L<sup>-1</sup>) was quickly added to the mixture, which after 10 minutes produced a change in color to black as a result of Pt deposition at the TiO<sub>2</sub> surface. The reaction was allowed to proceed for other 30 minutes at 90°C. This was the first reduction step, the material obtained at this stage was denoted Pt/TiO<sub>2</sub>-1, in which the number 1 refers to one Pt deposition step. A second reduction step was performed by adding more PtCl<sub>6</sub>2-(aq) solution (6 mL, 3.0 mmol L<sup>-1</sup>) to the reaction mixture obtained at the end of the first reduction step, followed by stirring at 90°C for other 30 min. Similarly, a third reduction step was carried out by adding more PtCl<sub>6</sub>2-(aq) solution (6 mL, 3.0 mmol L<sup>-1</sup>) to the reaction mixture obtained at the end of the second reduction step, followed by stirring at 90 °C for another 30 min. As described in the first deposition step, the solids that were obtained after the second and third reduction steps were denoted Pt/TiO<sub>2</sub>-2 and Pt/TiO<sub>2</sub>-3, respectively. These materials were isolated by stopping the reaction at the end of each corresponding reduction step. In all cases, the products were harvested by centrifugation, washed several times with water and ethanol, and re-suspended in water for further use. These samples were dried and weighed for ICP-OES analyses.

*Impregnation of Pt/TiO<sub>2</sub>-1, Pt/TiO<sub>2</sub>-2, and Pt/TiO<sub>2</sub>-3 onto carbon Vulcan XC-72:*

The Pt/TiO<sub>2</sub>-1, Pt/TiO<sub>2</sub>-2, and Pt/TiO<sub>2</sub>-3 materials were impregnated onto a carbon support in order to produce 10% wt. Pt/TiO<sub>2</sub>-1/C, Pt/TiO<sub>2</sub>-2/C, and Pt/TiO<sub>2</sub>-3/C on Vulcan XC-72 Carbon (Cabot®) by a wet impregnation method. Typically, Carbon (50 mg) was used

as support for the nanomaterials. The supports were added to aqueous suspensions containing 5 mg of each material and left under vigorous magnetic stirring at 110°C until dry.

*Electrochemical studies:*

The electrochemical experiments were performed at 25°C in an electrochemical three-electrode cell with H<sub>2</sub>SO<sub>4</sub> (80 mL, 0.5 mol L<sup>-1</sup>) as support electrolyte using a potentiostat/galvanostat PGSTAT model 302 N (Autolab®) coupled to a rotating ring-disk electrode accessory (Pine®) and controlled by the Nova 10.1 software. The counter electrode was a platinum rod, while an Ag/AgCl electrode (Analyzer®) was used as reference. The work electrode was a rotating ring-disk electrode consisting of a glassy carbon disk (0.196 cm<sup>2</sup>) and platinum ring (0.037 cm<sup>2</sup>) with the collection factor of 0.37. After thoroughly characterizing the catalysts, a suspension of each material was prepared in milli-Q water in order to deposit them onto the electrode. An ink was prepared using 1 mg of electrocatalyst and 1 mL of ultrapure water (Milli Q system, 18.2 mΩ cm<sup>-1</sup>) sonicated for 30 minutes. The glassy carbon disk surface was covered by a drop of 20 µL of the electrocatalytic ink and dried under N<sub>2</sub> flux. Subsequently, 20 µL of a 1:100 solution of Nafion® and ultrapure water were dropped onto the material, and then further dried under N<sub>2</sub> flux at room temperature. The electrocatalysts were then further characterized regarding their electrocatalytic properties.

For CO stripping measurements, carbon monoxide was adsorbed on a 20 mV polarized electrode, during 5 minutes, immersed in an H<sub>2</sub>SO<sub>4</sub> solution (0.5 mol L<sup>-1</sup>). Subsequently, CO was removed from the electrolyte by purging with N<sub>2</sub> for 25 minutes, and three consecutive cyclic voltammetries were run with a scan rate of 10 mV s<sup>-1</sup> within the potential range of 0.01 to 1.01 V *versus* RHE reference electrode. The electrochemical surface areas (ESA)<sup>23</sup> for CO stripping were obtained by integrating the area under each CO oxidation peaks in the first voltammetric cycle (Q<sub>co</sub>, in mC), these were then divided by the charge

needed to oxidize a CO monolayer adsorbed onto a Pt surface ( $Q_{CO} = 420 \mu C \text{ cm}^{-2}$ ). These values were then normalized by the mass of Pt on each electrode and the ECSA was obtained in  $m^2 \text{ g}^{-1}$ .

For the oxygen reduction reaction (ORR), linear scanning voltammograms were collected with a scan rate of  $0.01 \text{ V s}^{-1}$  in an ultrapure  $O_2$  saturated  $H_2SO_4$  electrolyte ( $0.5 \text{ mol L}^{-1}$ , 30 minutes of  $O_2$  purge) in the potential range between 1.21 and 0.21 V (vs RHE) in different rotation speeds ( $\omega$ ) from 100 to 2500 rpm. For experiments performed under light irradiation, a UV LED stick (UVP Pen-Ray (R) Light source) was used. All the analyses were performed in triplicate.

*Accelerated stress tests (AST):*

In order to study the stability of the electrocatalysts, the most promising catalyst (Pt/TiO<sub>2</sub>-2/C) was compared to the commercial material (Pt/C E-TEK) in accelerated stress tests. A typical test was performed in  $H_2SO_4$  ( $0.5 \text{ mol L}^{-1}$ ) as support electrolyte. An ORR polarization curve was then collected with a scan rate of  $0.01 \text{ V s}^{-1}$  in an ultrapure  $O_2$  saturated  $H_2SO_4$  electrolyte ( $0.5 \text{ mol L}^{-1}$ , 30 minutes of  $O_2$  purge) in the potential range between 1.21 and 0.21 V (vs RHE) in different rotation speeds ( $\omega$ ) from 100 to 2500 rpm. After performing the ORR, the electrolyte was switched for a fresh one and  $N_2$  was bubbled for 30 minutes before performing the cycles, 1000 cyclic voltammeteries were run with a scan rate of  $100 \text{ mV s}^{-1}$  within the potential range of 0.01 to 1.01 V versus RHE. Oxygen was once again bubbled for 30 minutes and ORR was performed in the same conditions as previously established.

### 4.3 – Results and Discussion

**Figure 4.1A** and **B** show SEM and HRTEM images of the TiO<sub>2</sub> colloidal spheres that were employed supports for the Pt/TiO<sub>2</sub> materials. The TiO<sub>2</sub> spheres displayed spherical shape and were  $267.8 \pm 37.8$  nm in diameter. Although they appear to be smooth from SEM images, HRTEM results revealed that they are comprised of TiO<sub>2</sub> nanocrystallites (around 10 nm in size). They were crystallized as anatase according to previously reported XRD and Raman data.<sup>20,24</sup>

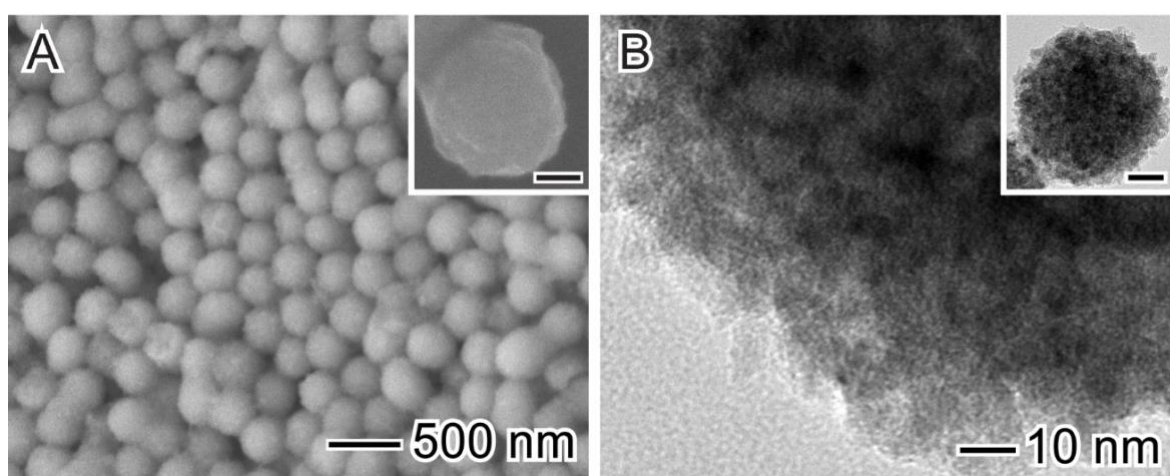


**Figure 4.1** – SEM (A) and HRTEM (B) images of TiO<sub>2</sub> colloidal spheres. They displayed spherical shape, relatively monodisperse sizes, and rough surfaces comprised of smaller (~10 nm) crystallites. The overall diameter of the TiO<sub>2</sub> colloidal spheres corresponded to  $267.8 \pm 37.8$  nm. The scale bars in the insets correspond to 100 nm (A) and 50 nm (B).

The TiO<sub>2</sub> colloidal spheres were employed as seeds for Pt deposition at their surface with controllable sizes and coverage by a facile route based on sequential deposition steps as depicted in **Figure 4.2**. This approach employed PtCl<sub>6</sub><sup>2-</sup> as the Pt precursor, ascorbic acid as a reducing agent, PVP as a stabilizer, water as the solvent, and 90°C as the reaction temperature. The loading and coverage of Pt at the surface could be controlled by performing successive deposition steps, which allows for the understanding of how these parameters affect the electrocatalytic activity of the generated materials towards the ORR. Specifically,



three Pt deposition steps were performed, which led to Pt/TiO<sub>2</sub>-1, Pt/TiO<sub>2</sub>-2, and Pt/TiO<sub>2</sub>-3 materials (obtained after one, two, and three Pt deposition steps, respectively).

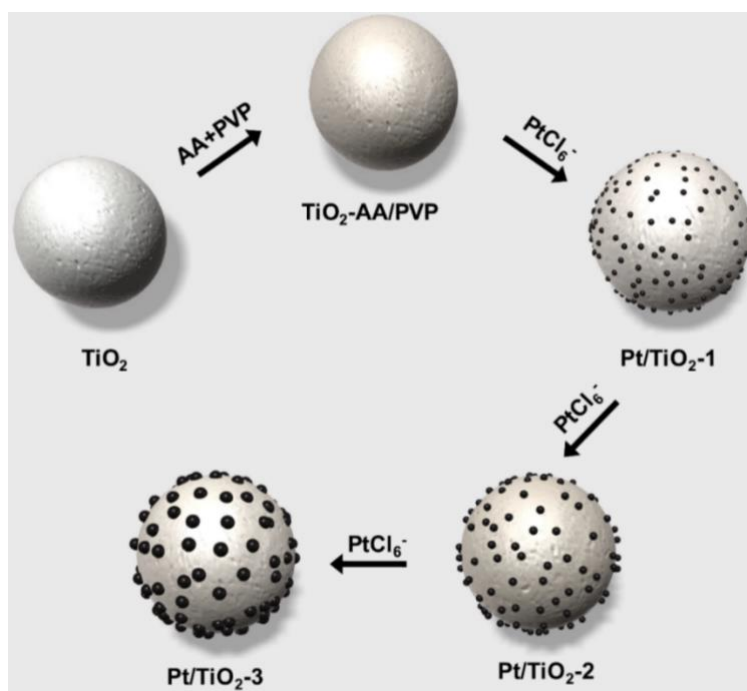


**Figure 4.2** – Scheme for the syntheses of Pt/TiO<sub>2</sub>-1, Pt/TiO<sub>2</sub>-2, and Pt/TiO<sub>2</sub>-3 materials. TiO<sub>2</sub> colloidal spheres are used as seeds for the deposition of Pt NPs using ascorbic acid as reducing agent, polyvinylpyrrolidone as stabilizer, water as solvent, and PtCl<sub>6</sub><sup>2-</sup> as the Pt precursor. The size and Pt content at the TiO<sub>2</sub> surface could be controlled by performing sequential Pt deposition steps.

SEM images for the Pt/TiO<sub>2</sub>-1, Pt/TiO<sub>2</sub>-2, and Pt/TiO<sub>2</sub>-3 materials (**Figure 4.3A-C**, respectively) indicate the efficient deposition of Pt NPs at the TiO<sub>2</sub> supports displaying a uniform surface dispersion, spherical shape, and uniform sizes. The Pt content and coverage at the TiO<sub>2</sub> surface could be tailored by performing sequential reduction steps. The ICP-OES analyses indicated the presence of 20.1, 31.0, and 38.4 wt.% of Pt in the Pt/TiO<sub>2</sub>-1, Pt/TiO<sub>2</sub>-2, and Pt/TiO<sub>2</sub>-3 samples, respectively.

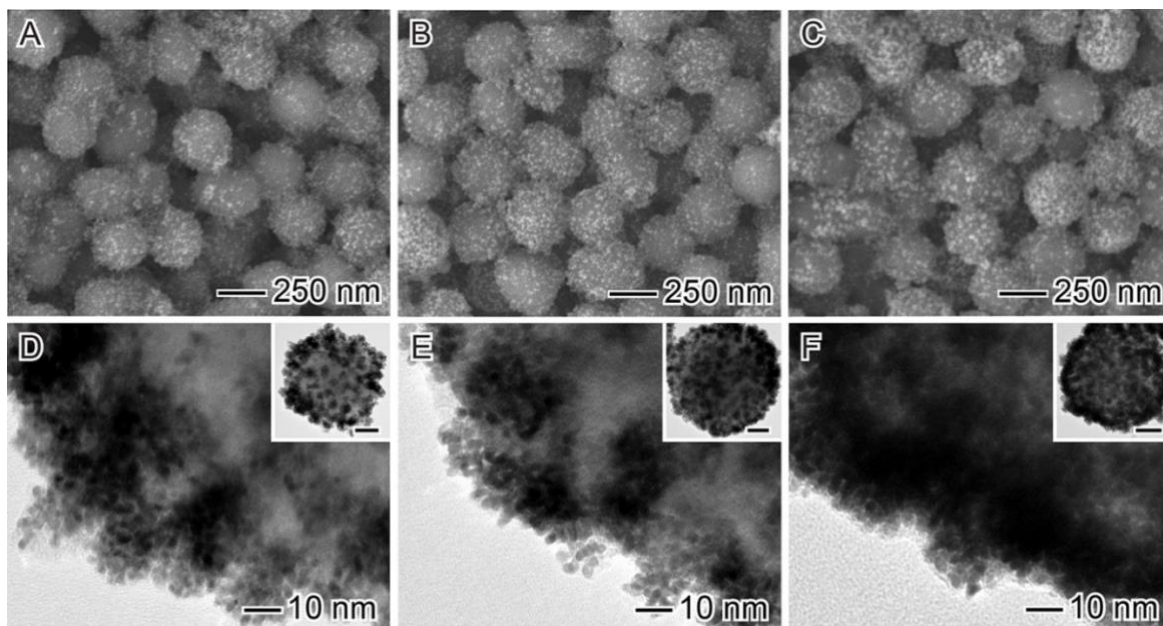


**Figure 4.3** – SEM (A-C) and TEM (D-F) images of Pt NPs supported at the surface of TiO<sub>2</sub> colloidal spheres (Pt/TiO<sub>2</sub>) after one (A, D), two (B, E), and three (C, F) deposition steps. The scale bars in the insets correspond to 50 nm.

High-Resolution Transmission Electron Microscopy (HRTEM) images for the Pt/TiO<sub>2</sub>-1, Pt/TiO<sub>2</sub>-2, and Pt/TiO<sub>2</sub>-3 samples (**Figure 4.3D-F**, respectively) revealed that the individual Pt NPs were comprised of aggregates made up of individual, smaller Pt NPs measuring about 3 nm in size (estimated based on TEM images). While a lower Pt coverage at the TiO<sub>2</sub> surface can be observed for both Pt/TiO<sub>2</sub>-1 and Pt/TiO<sub>2</sub>-2 samples (**Figure 4.3D** and **E**), the highest coverage was detected in the Pt/TiO<sub>2</sub>-3 material (**Figure 4.3F**).

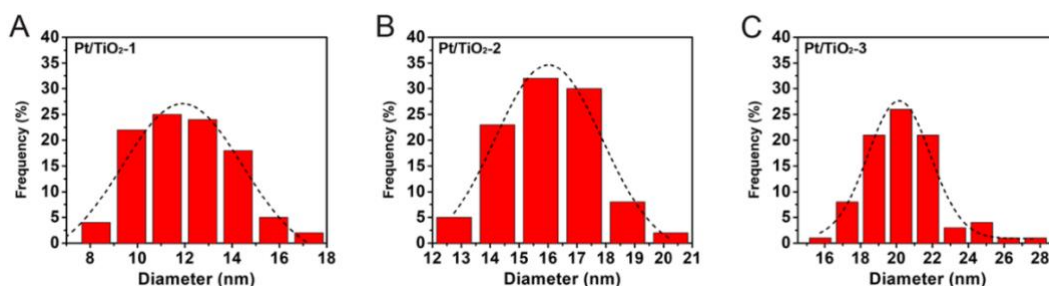


**Figure 4.4** – Pt NPs size distribution histograms for the Pt/TiO<sub>2</sub>-1/C, Pt/TiO<sub>2</sub>-2/C, and Pt/TiO<sub>2</sub>-3/C materials (A, B, and C, respectively). Here we can notice the growth of Pt nanoclusters with the addition of Pt precursor, for the Pt/TiO<sub>2</sub>-1/C sample, the nanoparticle

diameters range between  $11.9 \pm 3.0$  nm (A), while Pt/TiO<sub>2</sub>-2/C the size distribution is between  $16.0 \pm 2.2$  nm, and Pt/TiO<sub>2</sub>-3/C ranges between  $20.1 \pm 2.1$  nm.

As the addition of more Pt precursor occurred after every stage, the particles suffered a significant growth as observed on the histograms. Particles prepared with one addition of PtCl<sub>6</sub><sup>2-</sup> grew to an average cluster size of  $11.9 \pm 3.0$  nm, while two additions produced NPs with  $16.0 \pm 2.2$  nm and three additions produced particles with sizes of  $20.1 \pm 2.1$  nm. After the syntheses, the Pt/TiO<sub>2</sub>-1, Pt/TiO<sub>2</sub>-2, and Pt/TiO<sub>2</sub>-3 samples were incorporated onto Vulcan XC-72 Carbon (Cabot®) by wet impregnation, this method, employed in many fields of catalysis, is based on adding the preformed materials suspended in a solvent onto the support and letting it dry. This led to Pt/TiO<sub>2</sub>-1/C, Pt/TiO<sub>2</sub>-2/C, and Pt/TiO<sub>2</sub>-3/C materials, respectively. In all cases, the Pt/TiO<sub>2</sub> loading corresponded to 10 wt.%, reaching the overall Pt loading of 2.01, 3.10, and 3.84 wt.% for Pt/TiO<sub>2</sub>-1/C, Pt/TiO<sub>2</sub>-2/C, and Pt/TiO<sub>2</sub>-3/C, respectively.

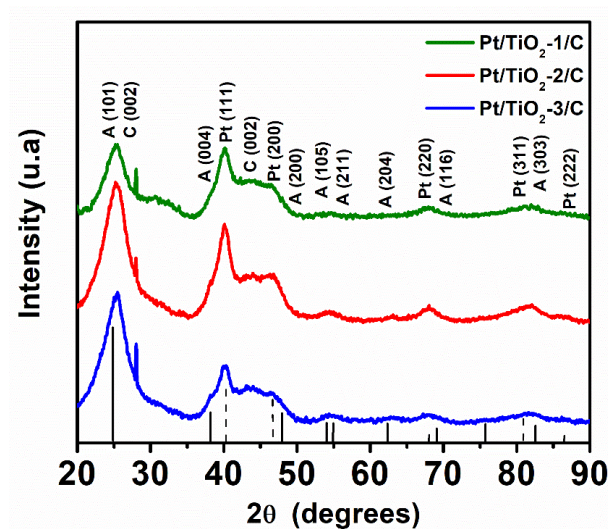


**Figure 4.5** – X-ray diffractograms for the Pt/TiO<sub>2</sub>-1/C, Pt/TiO<sub>2</sub>-2/C, and Pt/TiO<sub>2</sub>-3/C materials (green, red, and blue traces, respectively). The black solid and dashed lines indicate the JCPDF patterns used to identify the TiO<sub>2</sub> and Pt peaks (solid and dashed lines, respectively). Here, the samples presented characteristic peaks of the TiO<sub>2</sub> anatase phase, *fcc* Pt, and carbon.

**Figure 4.5** shows the XRD profiles for the Pt/TiO<sub>2</sub>-1/C, Pt/TiO<sub>2</sub>-2/C, and Pt/TiO<sub>2</sub>-3/C materials. The diffractograms show the characteristic reflections assigned to TiO<sub>2</sub> anatase, *fcc* Pt, and carbon. This indicates that our wet impregnation approach was effective for the incorporation of Pt/TiO<sub>2</sub> onto the carbon support.

In order to probe the generation of ORR reactive sites in the Pt/TiO<sub>2</sub>-3/C materials as a result of metal-support interactions, the samples were studied by XPS. **Figure 4.6A-D** shows the Ti 2p, Pt 4f, C 1s, and O 1s core level XPS spectra along with their fitting and deconvoluted curves, obtained for the Pt/TiO<sub>2</sub>-1/C, Pt/TiO<sub>2</sub>-2/C, and Pt/TiO<sub>2</sub>-3/C materials. Data for Vulcan XC-72 carbon is also shown for comparison. The corresponding XPS parameters obtained from the spectra are shown in **Table 4.1**(for Ti, Pt, and O) and **4.2** (for C).

**Table 4.1** – Binding energies and surface percentages measured by XPS.

Material	Binding energy (eV)				
	Pt 4f <sub>7/2</sub>	Ti 2p <sub>3/2</sub>	O 1s		
			O <sub>I</sub>	O <sub>II</sub>	O <sub>III</sub>
<b>Vulcan XC-72</b>	n.d.	n.d.	530.9 (11)*	533.2 (80)	536.8 (9)
<b>Pt/TiO<sub>2</sub>-1/C</b>	71.5	459.6	531.4 (34)	533.4 (58)	536.0 (8)
<b>Pt/TiO<sub>2</sub>-2/C</b>	71.5	459.6	531.4 (32)	533.3 (60)	535.9 (8)
<b>Pt/TiO<sub>2</sub>-3/C</b>	71.5	459.7	531.7 (28)	533.7 (65)	536.5 (7)

\*Species surface percentage

The Ti 2p spectrum (**Figure 4.6A**) displayed doublet peaks at 459.4 eV and 465.1 eV assigned to Ti 2p<sub>3/2</sub> and Ti 2p<sub>1/2</sub>, respectively. The splitting width between the two peaks was of 5.7 eV, indicating only the presence of Ti<sup>4+</sup> chemical state.<sup>25</sup> Ti 2p peaks were slightly shifted towards higher binding energies as compared to those in TiO<sub>2</sub>, which indicates a change in the Ti chemical environment possibly due to strong interactions with the Carbon support (such as the formation of Ti-O-C bonds).<sup>26</sup>

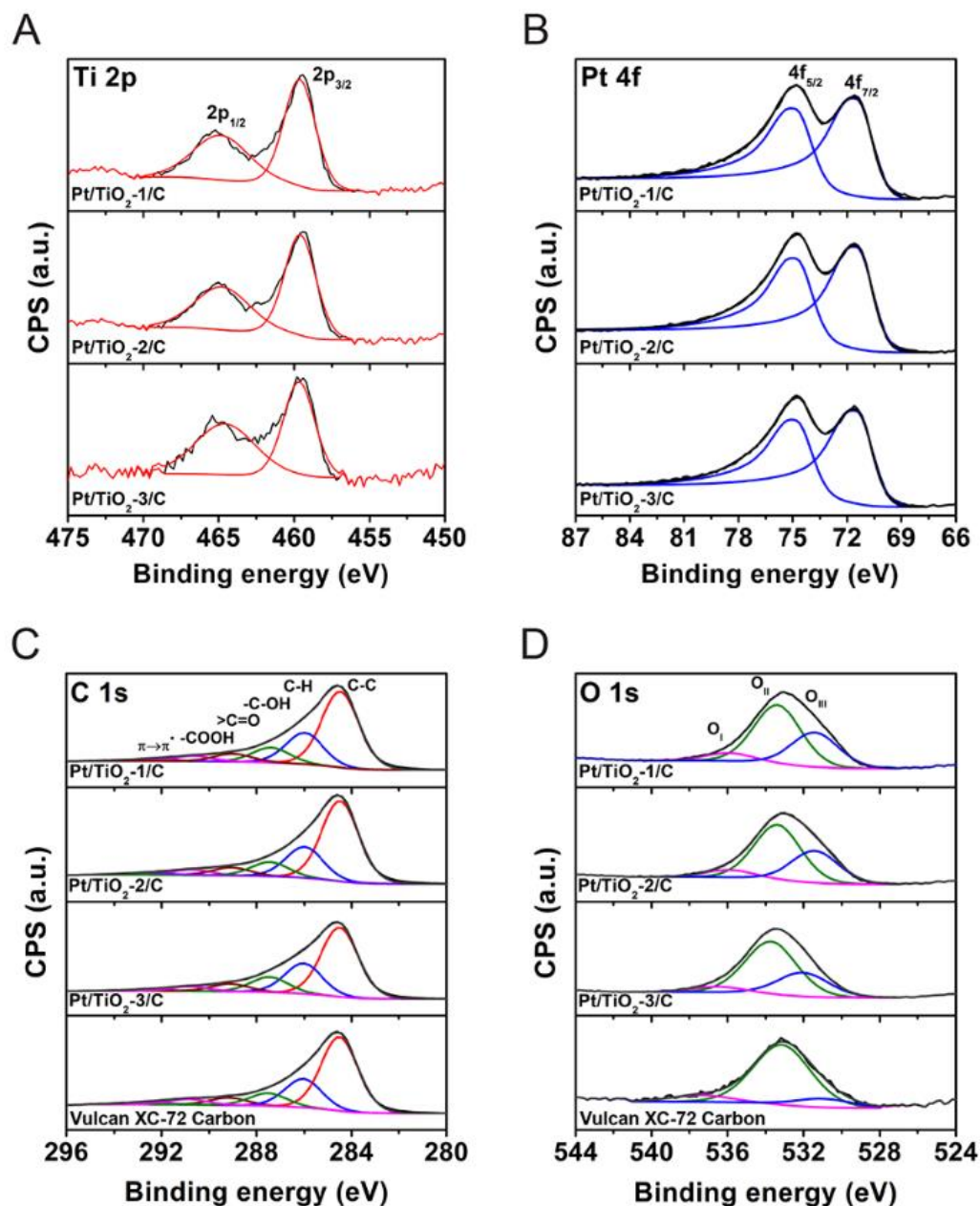


**Figure 4.6** – Deconvoluted X-ray photoelectron spectra (XPS) of the Ti 2p (A), Pt 4f (B), C 1s (C), and O 1s (D) core levels for Pt/TiO<sub>2</sub>-1/C, Pt/TiO<sub>2</sub>-2/C, Pt/TiO<sub>2</sub>-3/C, Vulcan XC-72 carbon (top to bottom traces, respectively).

As shown in **Figure 4.6B**, the Pt 4f region revealed that the 4f<sub>7/2</sub> and 4f<sub>5/2</sub> spin-orbital components have an asymmetric shape which is typical for Pt<sup>0</sup>.<sup>27,28</sup> The peaks located at 71.5 and 74.9 eV can be assigned to Pt 4f<sub>7/2</sub> and Pt 4f<sub>5/2</sub> of Pt<sup>0</sup>, respectively. The slight shift towards higher binding energy values compared to literature values (71.0 eV) is attributed to

metal-support interaction and to small Pt NPs sizes.<sup>28,29</sup> This positive shift may also suggest metal-support interactions between TiO<sub>2</sub> and Pt. This interaction can modify the electronic properties of Pt by increasing the Pt d-vacancy via electronic donation to Lewis acid centers such as Ti<sub>x+</sub> at the Pt/TiO<sub>2</sub> interface.<sup>30–32</sup>

**Table 4.2** – Binding energies, surface percentages, and oxygenated carbon/carbon ratios measured by XPS.

Material	Binding energy C 1s (eV)						Intensity (%)
	Peak I C-C	Peak II C-H (defects)	Peak III - C-OH	Peak IV >C=O	Peak V - COOH	Peak VI $\pi \rightarrow \pi^*$	I <sub>oxy</sub> /I <sub>C</sub> **
<b>Vulcan XC-72</b>	284.5 (57)*	286.0 (21)	287.5 (10)	289.2 (6)	290.8 (4)	292.8 (2)	19
<b>Pt/TiO<sub>2</sub>-1/C</b>	284.5 (55)	286.0 (23)	287.4 (10)	289.0 (6)	290.6 (4)	292.4 (2)	26
<b>Pt/TiO<sub>2</sub>-2/C</b>	284.5 (57)	286.0 (22)	287.4 (10)	289.0 (6)	290.8 (4)	292.5 (1)	25
<b>Pt/TiO<sub>2</sub>-3/C</b>	284.5 (54)	286.0 (24)	287.5 (11)	289.1 (6)	290.8 (4)	292.5 (1)	27

\* Species surface percentage

\*\*Intensity of three oxygen-containing functional groups (peaks III-V) in % of total C 1s area.

Regarding the C 1s region, it was possible to deconvolute the C 1s spectrum into six peaks (**Figure 4.6C**). The lowest binding energy and dominant peak at about 284.5 eV corresponds to the graphitic carbon phase,<sup>33</sup> while the peak at around 286.0 eV is assigned to hydrocarbons (C-H) from defects on the graphitic structure.<sup>34</sup> Three carbon-oxygen bonding structures for the –C-OH, >C=O and –COOH can also be observed at approximately 287.5, 289.2 and 290.8 eV, respectively. The subpeak located at higher than 292.8 eV is related to  $\pi \rightarrow \pi^*$  plasmonic excitation.<sup>35</sup> It is noteworthy that it has been established that acidic oxygenated species contribute to the generation of H<sub>2</sub>O<sub>2</sub> in the ORR.<sup>36,37</sup> In our case, XPS data indicate that the Pt/TiO<sub>2</sub>-2/C sample presented the lowest amount of oxygenated species on the surface (as seen on I<sub>oxy</sub>/I<sub>C</sub> depicted in **Table 3.2**). Therefore, it can be anticipated that this material would generate the lowest amount of H<sub>2</sub>O<sub>2</sub> during the reaction and lead to a

higher ORR current density relative to the other samples (Pt/TiO<sub>2</sub>-1/C and Pt/TiO<sub>2</sub>-3/C).<sup>24</sup> The O 1s core level peaks for the Pt/TiO<sub>2</sub>/C materials are shown in **Figure 4.6D**. The O 1s peaks could be deconvoluted in three peaks. The first component (O<sub>I</sub>) centered at 531 eV was attributed to the lattice oxygen in the oxides and C=O functional groups. The second and dominant component (O<sub>II</sub>) located at 533 eV was attributed to chemisorbed oxygen species (such as OH-) and functional C-O groups. The last component (O<sub>III</sub>) with BE around 536 eV were characteristic of adsorbed water.<sup>26,38</sup>

After probing the metal-support interactions and generation of reactive surface species by XPS, we investigated their electroactive areas by CO stripping as described in **Figure 4.7**.

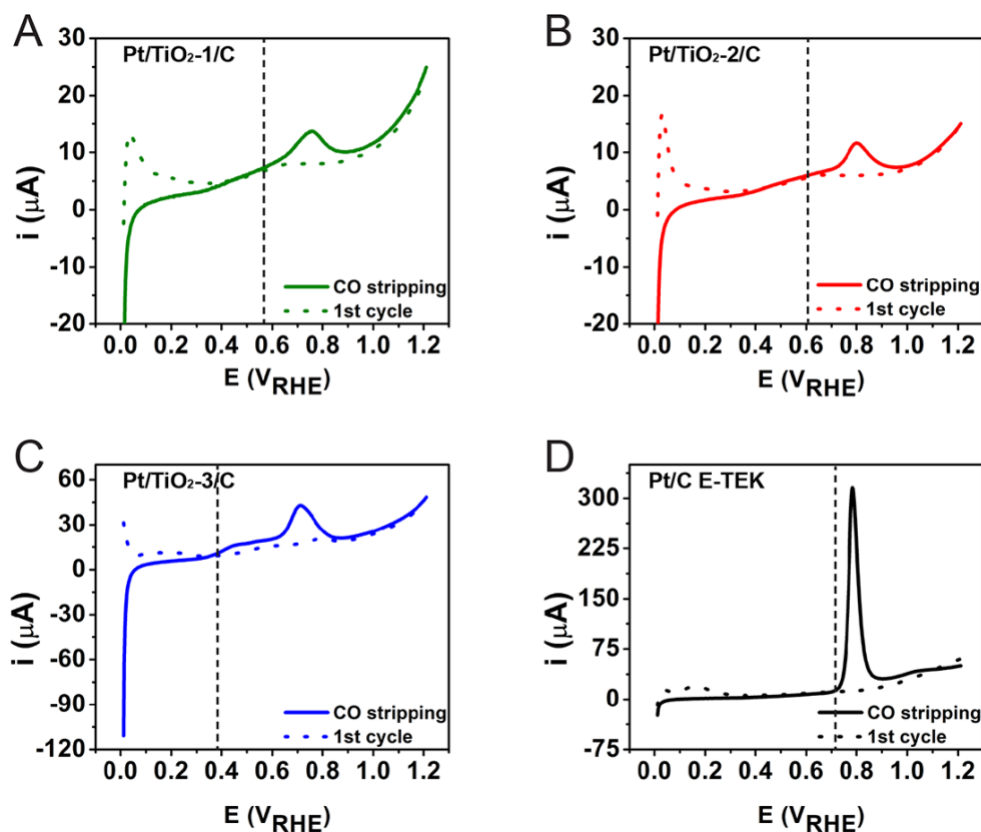


**Figure 4.7** – CO-stripping (solid trace) and subsequent cyclic voltammograms (dashed trace) for Pt/TiO<sub>2</sub>-1/C (A), Pt/TiO<sub>2</sub>-2/C (B), Pt/TiO<sub>2</sub>-3/C (C), and Pt/C E-TEK (D) registered in H<sub>2</sub>SO<sub>4</sub> 0.5 mol L<sup>-1</sup> under N<sub>2</sub> atmosphere.  $V = 10 \text{ mV s}^{-1}$ .  $T = 273\text{K}$ .



The Pt/TiO<sub>2</sub>/C materials presented lower onset potential for carbon monoxide oxidation when compared to commercial Pt/C E-TEK, a behavior related to the interaction between Pt and TiO<sub>2</sub>. This interaction (as suggested by XPS data) decreases the adsorption of CO at the metal surface facilitating the oxidation.<sup>39</sup> A main current density peak was detected between 0.76 and 0.80 V *vs* RHE (Reversible Hydrogen Electrode) for all materials, which is assigned to the CO oxidation on the Pt sites interacting with sp<sup>3</sup> disordered carbon.<sup>2,40</sup> In addition, a shoulder at lower potentials was observed (0.46 V *vs* RHE) for the Pt/TiO<sub>2</sub>-3/C, which can be assigned to the partial agglomeration of Pt NPs on the TiO<sub>2</sub> surface caused by the higher Pt coverage in this material.<sup>41</sup> The ESA (electrochemical surface area) and ECSA (electrochemical active surface area) of the materials calculated from the CO-stripping experiments are depicted in **Table 4.3**.<sup>42</sup> It can be observed that the ECSA increased with the Pt loadings, corresponding to 2.41, 9.78, and 25.2 m<sup>2</sup>g<sup>-1</sup> for Pt/TiO<sub>2</sub>-1/C, Pt/TiO<sub>2</sub>-2/C, and Pt/TiO<sub>2</sub>-3/C materials, respectively. However, it is important to note that these ECSA values were significantly lower as compared to Pt/C E-TEK (68.2 m<sup>2</sup>g<sup>-1</sup>). This is probably due to the aggregation of the Pt NPs on the TiO<sub>2</sub> surface as observed by HRTEM.

**Table 4.3** – Physicochemical parameters of electrocatalysts related to the electrochemical surface area (ESA) estimated from the CO stripping measurements.

Material	Mass of Pt on the electrode (μg)	ESA (cm <sup>2</sup> )	ECSA (m <sup>2</sup> g <sup>-1</sup> )
Pt/TiO <sub>2</sub> -1/C	1.24	0.03	2.41
Pt/TiO <sub>2</sub> -2/C	1.65	0.16	9.78
Pt/TiO <sub>2</sub> -3/C	1.92	0.48	25.2
Pt/C E-TEK	6.00	4.09	68.2

**Figure 4.8A-D** depicts the linear sweep voltammetries (LSV) for the Pt/TiO<sub>2</sub>-1/C (**Figure 4.8A**), Pt/TiO<sub>2</sub>-2/C (**Figure 4.8B**), and Pt/TiO<sub>2</sub>-3/C (**Figure 4.8C**) and Pt/C E-TEK



(**Figure 4.8D**) materials towards the ORR performed in  $O_2$  saturated  $H_2SO_4$  ( $0.5 \text{ mol L}^{-1}$ ) at different rotation rates (from 100 rpm to 2500 rpm as indicated by the colors in the inset, **Figure 4.8A**). The detected currents were normalized by the geometric surface areas of the electrodes ( $0.196 \text{ cm}^2$  for the disk and  $0.037 \text{ cm}^2$  for the ring) and presented as current densities. **Figure 4.8E-H** depicts the disk currents for the ORR, respectively, using each electrocatalyst shown in **Figure 4.8A-D**. These results show an increase in ring current density values (**Figure 4.8A-D**) on potentials lower than  $0.80 \text{ V vs RHE}$ , which indicates the conversion of  $O_2$  onto  $H_2O_2$  as detected by its oxidation on the ring electrode.<sup>43–46</sup> The values obtained for our materials, as well as for the commercial one, are in clear agreement with the literature, using the same mass of Pt and same medium as in the present work.<sup>43–46</sup>

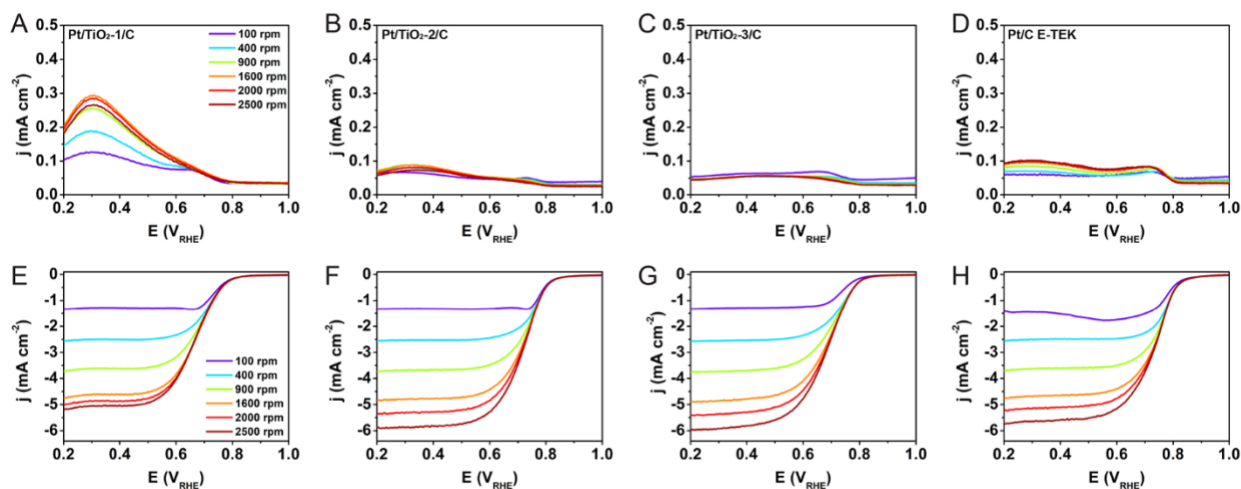


**Figure 4.8** – Rotating ring (A-D) and rotating disk (E-H) voltammograms for the ORR employing Pt/TiO<sub>2</sub>-1/C (A, E), Pt/TiO<sub>2</sub>-2/C (B, F), Pt/TiO<sub>2</sub>-3/C (C, G), and Pt/C E-TEK (D, H) as electrocatalysts. These experiments were performed in  $O_2$  saturated  $0.5 \text{ mol L}^{-1} H_2SO_4$  with a sweep rate of  $10 \text{ mVs}^{-1}$  at different rotation rates (as indicated in the insets) and  $273 \text{ K}$ .

On the other hand, the disk current density (**Figure 4.8E-H**) is lowered in potentials below  $0.81 \text{ V}$ , which indicates the formation of  $H_2O$ . Additionally, LSV of the ORR on the disk indicates a mixed kinetic-diffusion control region between potentials of  $0.90 \text{ V}$  and  $0.60$

V (vs RHE). This region is narrower under low rotations and becomes larger at higher rotations. The region between 0.60 V and lower potentials is assigned to the diffusional control region. This behavior is normally seen for Pt-based electrocatalysts.<sup>47</sup> The disk's limiting current density increased gradually with the rotation rate, as expected for a diffusional-controlled reaction.<sup>48</sup> The water production efficiency (and consequently, the number of exchanged electrons per O<sub>2</sub> molecule) was calculated using the ring current densities using **Equation 4.1** and **4.2**:<sup>49</sup>

$$p(H_2O) = 2 \times \frac{\frac{i_r}{N_c}}{i_d + \frac{i_r}{N_c}} \quad (4.1)$$

$$n = 4 \times \frac{i_d}{i_d + \frac{i_r}{N_c}} \quad (4.2)$$

Where  $N_c$  is the collection factor (experimentally determined as  $N_c = 0.37$ ),  $i_d$  is the disk current,  $i_r$  is the ring current. These values are listed in **Table 4.4**. A small amount of electrogenerated hydrogen peroxide is observed from the ring current densities presented in **Figure 4.8**. When comparing the limiting current densities of the ring and disk on the commercial material, we can see that the ring current density is about 25 times lower than the disk, confirming that these electrodes produce mainly water (low hydrogen peroxide current). Hence, the number of electrons is closer to 4.

Considering Pt as the standard electrocatalytic metal for ORR via 4 electrons and that the experimental values obtained for Pt/C E-TEK were close to the theoretical ones (3.98 electrons 98.8% water), the number of electron and water percentages were compared in the diffusional region for all materials. These values become lower when the Pt loading on TiO<sub>2</sub> increases, which could be assigned to the preferential 4-electron mechanism of Pt for the ORR. From the ring curves (**Figure 4.8E-H**), two behavior changes are also noticed at 0.70 V and 0.30 V (vs RHE), which were more significantly seen on the Pt/TiO<sub>2</sub>-1/C material. It is suggested that the ORR on the disk, and consequently the oxidation of H<sub>2</sub>O<sub>2</sub> on the ring,

occur as a function of the applied potential. Our results suggest that there are probably two mechanisms of formation of hydrogen peroxide, one at lower overpotentials and one at higher overpotentials.

**Table 4.4** – Summary of the RRDE data obtained for the ORR employing Pt/TiO<sub>2</sub>-1/C, Pt/TiO<sub>2</sub>-2/C, Pt/TiO<sub>2</sub>-3/C, and Pt/C-E TEK as electrocatalysts. *n* refers to the number of exchanged electrons and *p* the water proportion efficiency based on the ring and disk currents.<sup>49</sup>

E vs RHE	Pt/TiO <sub>2</sub> -1/C		Pt/TiO <sub>2</sub> -2/C		Pt/TiO <sub>2</sub> -3/C		Pt/C-E TEK	
	<i>n</i>	<i>p</i> (H <sub>2</sub> O) %	<i>n</i>	<i>p</i> (H <sub>2</sub> O) %	<i>n</i>	<i>p</i> (H <sub>2</sub> O) %	<i>n</i>	<i>p</i> (H <sub>2</sub> O) %
<b>0.60</b>	3.94	97.1	3.98	98.8	3.97	98.3	3.97	98.6
<b>0.50</b>	3.93	96.4	3.97	98.6	3.97	98.3	3.97	98.7
<b>0.40</b>	3.90	94.9	3.97	98.3	3.96	98.1	3.98	98.8
<b>0.30</b>	3.87	93.7	3.96	98.2	3.96	97.9	3.98	99.0
<b>0.20</b>	3.92	95.8	3.97	98.5	3.96	98.0	3.98	99.0
<b>Mean</b>	3.91	95.6	3.97	98.5	3.96	98.1	3.98	98.8

In order to better understand the reaction mechanism, Tafel curves were plotted from RDE data by the mass-transport correction of the current density measured for rotating disk electrodes and are presented in **Figure 4.9** according to **Equation 4.3**:

$$j_k = \frac{j_d^* j}{j_d - j} \quad (4.3)$$

where *j* is the experimentally measured current density, *j<sub>d</sub>* is the obtained diffusion-limited current density, and *j<sub>k</sub>* is the kinetic current density without the mass-transport effect. These values were calculated using the current density normalized by geometric area. The Tafel curves for the electrocatalysts presented two different regions, a behavior which is expected for Pt-based catalysts. At lower overpotentials, all the electrocatalysts presented slopes between -70 and -90 mV dec<sup>-1</sup>, reaching the highest value on Pt/TiO<sub>2</sub>-1/C (86.5 mV dec<sup>-1</sup>), which indicates that the mechanism of oxygen adsorption is similar to bulk Pt at 1.06 - 0.96 V

(vs RHE) potentials.<sup>15,19,50</sup> However, at higher overpotentials, there is an increase in module on the slope with the decrease of the Pt amount on the electrocatalyst from  $-124.7 \text{ mV dec}^{-1}$  (Pt/C E-TEK) to  $-135.2 \text{ mV dec}^{-1}$  (Pt/TiO<sub>2</sub>-1/C).<sup>51</sup> This observation indicates that the current densities are related to the oxygen adsorption energy on the electrocatalyst surface and that the first electron transfer is the determining step of the ORR.<sup>17</sup> These slope values were also observed for other TiO<sub>2</sub>-based electrocatalysts.<sup>15,17,51</sup> When comparing the Tafel plot for all the materials employed in this work, we can notice that the Pt/TiO<sub>2</sub>-2/C material presented a profile very similar to the Pt/C E-TEK material, even though it presents lower Pt content.

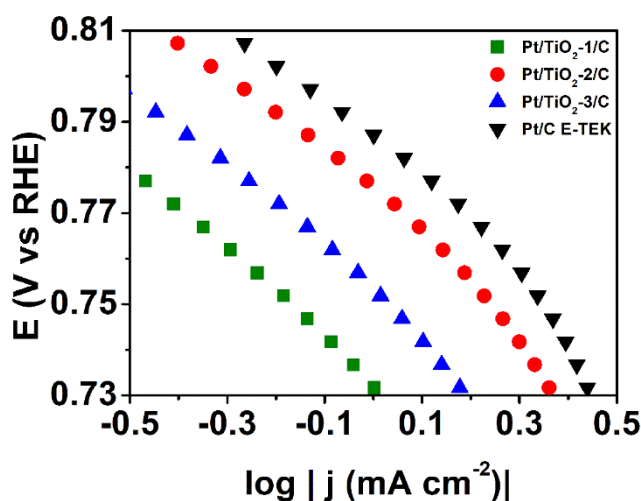


**Figure 4.9** – Tafel plots for Pt/TiO<sub>2</sub>-1/C (green trace), Pt/TiO<sub>2</sub>-2/C (red trace), Pt/TiO<sub>2</sub>-3/C (blue trace) and Pt/C E-TEK (black trace). The data was normalized by the geometric area of the electrode and calculated from their corresponding rotating disk electrode values at 1600 rpm.

Previous studies have shown that high slopes on the Tafel plot are normally associated with the rate determining step of the ORR, the O<sub>2</sub> adsorption onto the metal.<sup>52</sup> Tafel slopes normally increase on materials with lower Pt contents, which indicates that the mechanism tends to involve a 2-electron reaction. This was also observed for our materials when compared to the commercial Pt/C.<sup>53</sup> According to Shinagawa *et al.*<sup>52</sup>, the mechanism of the ORR is based on three different surface covering species, which are responsible for the

slopes on the Tafel plot. At lower overpotentials, the theoretical slopes can vary from 40 to 120 mV dec<sup>-1</sup> depending on the adsorbed species contributing to the rate determining step. As the slope lowers, it indicates there are more MOO<sup>-</sup> and MOOH species contributing to the rate-determining step of the reaction, while at higher slopes the rate determining step is governed by MOO adsorption. Hence, while the reaction on the Pt/C E-TEK catalyst is determined initially by MOO groups, the reaction also depended on the generation of MOO<sup>-</sup> and MOOH groups in the Pt/TiO<sub>2</sub>/C materials. On the other hand, at higher overpotentials, the Tafel slope is normally  $\geq 120$  mV dec<sup>-1</sup>, which indicates that the MOO and MOOH species are converting into MOO<sup>-</sup> species. Thus, the detected higher slopes show that the conversion starts in lower overpotentials or these catalysts already present a high number of MOO<sup>-</sup> species on their surface. This figure also shows that while the change in slope occurred at 0.775 V for the Pt/C E-TEK material, this change was only seen at higher overpotentials for the Pt/TiO<sub>2</sub>/C materials. Moreover, based on DFT simulations,<sup>54</sup> a strong interaction between Pt and TiO<sub>2</sub> is presumed due to the overlapping of the TiO<sub>2</sub> bonding orbitals with the Pt d-orbital. These calculations also indicate a strong interaction between Ti and Pt that could result in a negative overall net charge in this structure which could strengthen the Pt-O<sub>ads</sub> bond. Therefore, the desorption process could become slow in the high overpotential region, thus increasing the Tafel plot as observed in our data.

In order to better compare the relative ORR electrocatalytic activity of our materials, the ORR linear scanning voltammetries at 1600 rpm rotation rate were plotted as shown in **Figure 4.10A**. In addition, the electrocatalytic activity normalized by geometric mass (left-hand side) and Pt mass on the electrode (right-hand side) at 0.80 V (vs RHE) are shown in **Figure 4.10B**. The Pt/C E-TEK material presented a more positive onset potential for the ORR (0.89 V) followed by Pt/TiO<sub>2</sub>-2/C (0.88 V), Pt/TiO<sub>2</sub>-3/C (0.84 V), and Pt/TiO<sub>2</sub>-1/C (0.82 V). Here, it is important to note that the Pt/TiO<sub>2</sub>/C materials have less than half Pt

content in their composition compared to the commercial electrocatalyst. In agreement with the ORR onset potential, the number of transferred electrons follows the trend: Pt/C E-TEK > Pt/TiO<sub>2</sub>-2/C > Pt/TiO<sub>2</sub>-3/C > Pt/TiO<sub>2</sub>-1/C, indicating that the reaction is kinetically favorable in this order.

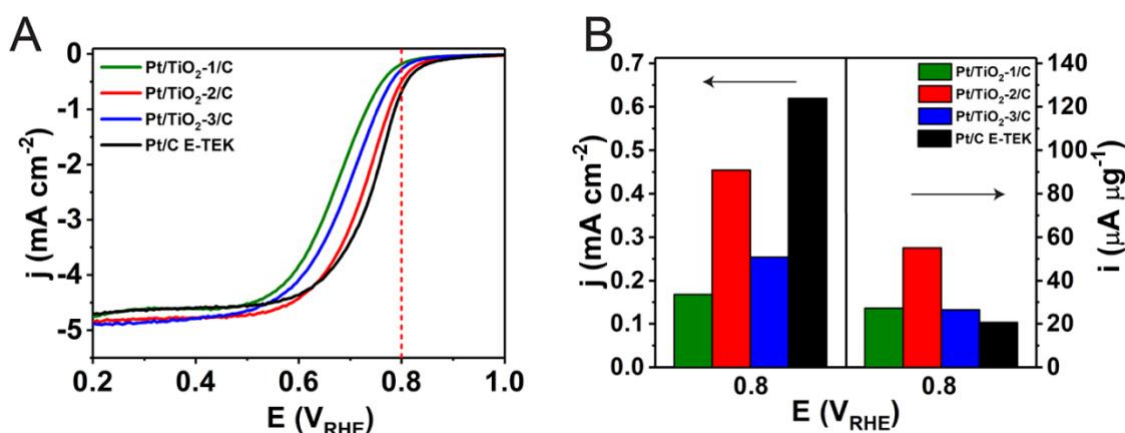


**Figure 4.10** – (A) Comparison of rotating disk linear scanning voltammetry for the ORR employing Pt/TiO<sub>2</sub>-1/C (green trace), Pt/TiO<sub>2</sub>-2/C (red trace), Pt/TiO<sub>2</sub>-3/C (blue trace) and Pt/C E-TEK (black trace) as electrocatalysts. The ORR was measured in O<sub>2</sub> saturated 0.5 mol L<sup>-1</sup> H<sub>2</sub>SO<sub>4</sub> solution at a rotation rate of 1600 rpm and T = 273 K. (B) Left panel: current densities at 0.8 V vs RHE for the materials shown in (A); Right panel: current densities divided by the Pt mass at 0.8 V vs RHE for the materials shown in (A).

Interestingly, even though the electrodes covered by Pt/TiO<sub>2</sub>/C hybrids have Pt loadings that range from threefold to fivefold lower than the one containing Pt/C E-TEK, they still present similar limiting diffusional current densities.<sup>55</sup> This led to much higher activities when the data is normalized by Pt mass in **Figure 4.10B**. Specifically, the Pt/TiO<sub>2</sub>-2/C material displayed a starting reduction potential close to Pt/C E-TEK (0.89 V and 0.88 V vs RHE, respectively). The higher activity of the Pt/TiO<sub>2</sub>-2/C material could be attributed to its lowest number of acidic oxygenated species at the surface as determined by XPS. These sites decrease the H<sub>2</sub>O<sub>2</sub> formation thus enhancing the water production and the current on the disk relative to the other materials<sup>24</sup>. This material also displays less Pt NPs aggregation at the

surface as compared to Pt/TiO<sub>2</sub>-3/C (**Figure 4.3**). It is noteworthy that the Pt/TiO<sub>2</sub>-1/C sample presented the highest H<sub>2</sub>O<sub>2</sub> production, which can also be attributed to the higher exposure of anatase TiO<sub>2</sub> at the surface as a result of lower Pt coverage.<sup>24,56</sup>

Our data indicate that the control over the Pt NPs coverage at the TiO<sub>2</sub> surface significantly influences their electrocatalytic activities towards the ORR. In this case, rather than an increase in activity with the Pt loading, a volcano-type relationship was observed, in which the sample produced by two Pt deposition steps (Pt/TiO<sub>2</sub>-2/C) displayed the highest activities due to the equilibrium between optimum Pt loading/surface coverage and the presence of surface reactive sites as enabled by metal-support interactions.

We also evaluated the stability of the Pt/TiO<sub>2</sub>-2/C material relative to Pt/C E-TEK by performing accelerated stress tests (AST) as shown in **Figure 4.11**.

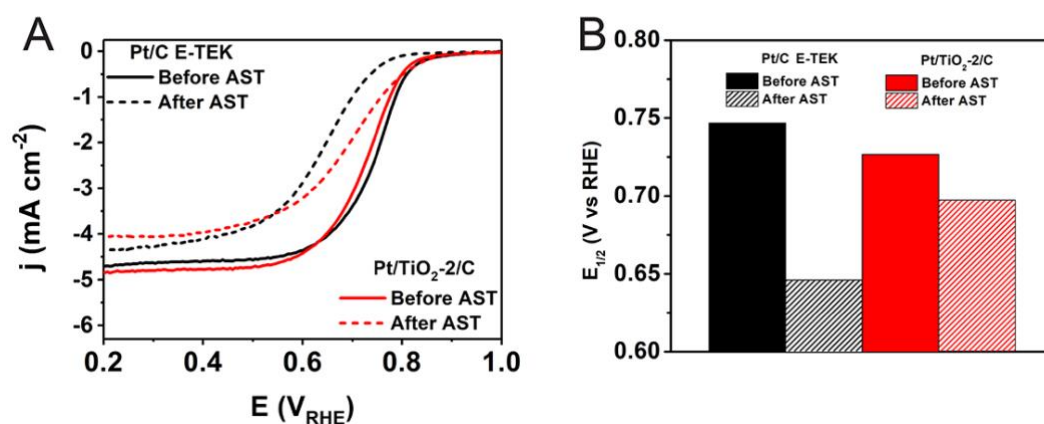


**Figure 4.11** – (A) Comparison of ORR polarization curves for Pt/TiO<sub>2</sub>-2/C (red trace) and Pt/C E-TEK (black trace) before (solid line) and after (dashed line) accelerated stress tests. The AST were performed using a 100 mV s<sup>-1</sup> scanning rate and 1000 voltammetric cycles from 0.01 to 1.01 V vs RHE. ORR was performed in O<sub>2</sub> saturated 0.5 mol L<sup>-1</sup> H<sub>2</sub>SO<sub>4</sub> solution at a rotation rate of 1600 rpm. (B) Half-wave potential for each sample before and after the accelerated stress test. T = 273K.

The initial and final ORR polarization curves are depicted as solid and dashed traces, respectively, in **Figure 4.11A**. The AST curves for the Pt/C E-TEK and Pt/TiO<sub>2</sub>-2/C are

shown in black and red, respectively. It can be observed that a decrease in activity was detected for both materials after the tests. However, when comparing their half-wave potential before and after the AST,  $E_{1/2}$ , (**Figure 4.11B**), a more significant decrease is detected for Pt/C E-TEK, from 0.747 to 0.646 V *vs* RHE compared to Pt/TiO<sub>2</sub>-2/C, which corresponded from 0.727 to 0.697 V *vs* RHE. When comparing half-wave potentials, shifts to smaller regions indicate an activity loss, thus, since for the commercial materials the shift is higher (approximately 0.31 V *vs* RHE) when compared to Pt/TiO<sub>2</sub>-2/C (approximately 0.24 V *vs* RHE). Moreover, after the AST, the number of electrons involved in the reactions and water percentages lowered for both materials, as seen in **Table 4.5**. While the mean electron number was of 3.94 and 3.92 on the Pt/TiO<sub>2</sub>-2/C and Pt/C E-TEK, they produced 97.1 and 96.1% of water, respectively. This further shows the low loss of overall activity of Pt/TiO<sub>2</sub>-2/C compared to the Pt/C E-TEK.

**Table 4.5** – Summary of the RRDE data obtained after the AST tests for the ORR employing Pt/C E-TEK and Pt/TiO<sub>2</sub>-2/C as electrocatalysts. *n* refers to the number of exchanged electrons and *p* the water proportion efficiency based on the ring and disk currents.<sup>49</sup>

E <i>vs</i> RHE	Pt/C E-TEK		Pt/TiO <sub>2</sub> -2/C	
	nRRDE	p(H <sub>2</sub> O)%	nRRDE	p(H <sub>2</sub> O)%
<b>0.60</b>	3.96	97.8	3.93	96.5
<b>0.50</b>	3.94	97.0	3.93	96.3
<b>0.40</b>	3.92	96.1	3.93	96.7
<b>0.30</b>	3.91	95.5	3.95	97.7
<b>0.20</b>	3.88	94.2	3.96	98.1
<b>Mean</b>	3.92	96.1	3.94	97.1

In addition to metal-support interactions, the utilization of TiO<sub>2</sub> as support also enables the harvesting of its photocatalytic properties to further improve activities. Therefore, the influence of UV irradiation on the electrocatalytic activity of the Pt/TiO<sub>2</sub>-2/C



electrocatalyst was also evaluated. The effect of light irradiation was probed in chronoamperometry experiments performed at 0.51 V (vs RHE) as shown in **Figure 4.12A** and the activity towards the ORR by linear scanning voltammogram as shown in **Figure 4.12B** (rotation rate of 1600 rpm in O<sub>2</sub> saturated 0.5 mol L<sup>-1</sup> H<sub>2</sub>SO<sub>4</sub> solution).

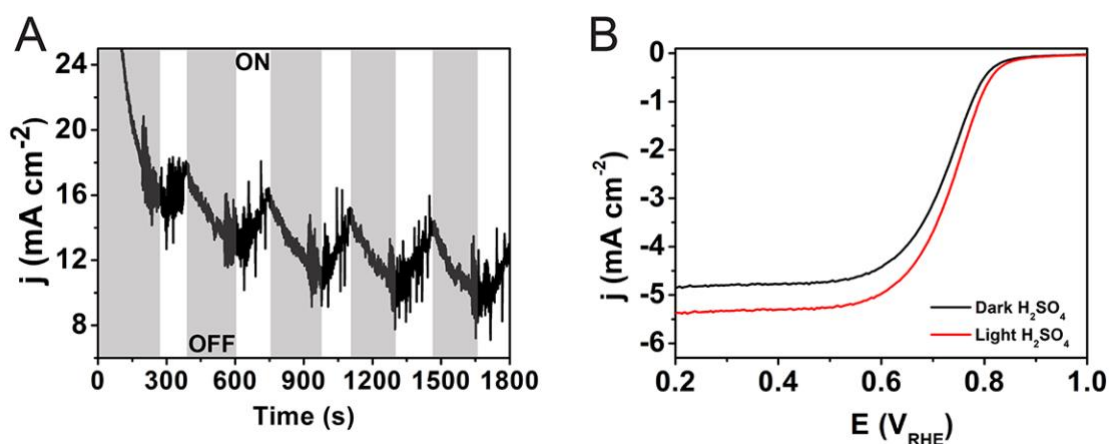


**Figure 4.12** – Photoelectrocatalytic profile of Pt/TiO<sub>2</sub>-2/C: (A) chronoamperometry at 0.51 V (vs. RHE) applying regular UV light pulses in the presence and absence of UV illumination; and (B) disk current density for the ORR measured under 1600 rpm in a 0.5 H<sub>2</sub>SO<sub>4</sub> mol L<sup>-1</sup> electrolyte in the presence and absence of UV light excitation (red and black traces, respectively).

Here, the activity under UV excitation was compared with its activity in the absence of UV excitation. **Figure 4.12A** shows a chronoamperometric assay while applying to the electrode UV light pulses of about 150 seconds. It was observed that under UV light excitation the current density increased in about 4 mA cm<sup>-2</sup> due to the light excitation. The voltammograms on **Figure 4.12B** revealed a slight shift to more positive potentials (~30 mV) and an increase of 11.3% on the limiting diffusion current density under UV-excitation. This indicates that the utilization that TiO<sub>2</sub> based electrocatalysts and UV light excitation can be employed to improve the electrocatalytic activities towards the ORR. It is anticipated that further optimizations can lead to further improvements both in the photoelectrocatalytic

activities and in the use of visible light (instead of UV) by TiO<sub>2</sub> doping or use Au NPs (harvesting of plasmonic effects).

## 4.4 – Conclusions

We investigated herein how Pt surface coverage in hybrid materials comprised of Pt NPs supported on TiO<sub>2</sub> colloidal spheres (Pt/TiO<sub>2</sub>) influence their electrocatalytic activities towards the ORR. It was demonstrated that, by employing TiO<sub>2</sub> colloidal spheres as physical templates, the uniform deposition of monodisperse and spherical Pt NPs ~3 nm could be achieved. The Pt coverage could be tuned as a function of the deposition steps. After incorporating the Pt/TiO<sub>2</sub> materials into Vulcan XC72 Carbon (to produce Pt/TiO<sub>2</sub>/C materials), the electrocatalytic activities towards the ORR as well as the reaction and enhancement mechanisms were investigated. Our results demonstrated that the control over the Pt coverage at the surface plays a pivotal role over the optimization of activities, in which a relationship among Pt content at the TiO<sub>2</sub> surface, the generation of reactive surface sites as a result of metal-support interactions, and ORR performance were unraveled. More specifically, the material produced from two Pt deposition steps displayed the highest activity, which was also superior as compared to commercial Pt/C E-TEK even at lower Pt loadings (between 2.0 and 4.0 wt.% of Pt on the final material). The variations in catalytic activity could be explained by the presence and concentration of surface reactive groups, such as adsorbed oxygenated species as a function of the Pt coverage. Moreover, the presence of TiO<sub>2</sub> as support enabled increased stability relative to Pt/C ETEK. These results illustrate that the understanding of the electrocatalytic enhancement mechanism together with the controlled synthesis of Pt-based nanomaterials can lead to tailored surface properties and electrocatalytic activities.

## 4.5 – References

- 1 Barbosa ECM, Parreira LS, de Freitas IC, Aveiro LR, de Oliveira DC, dos Santos MC *et al.* Pt-Decorated TiO<sub>2</sub> Materials Supported on Carbon: Increasing Activities and Stabilities toward the ORR by Tuning the Pt Loading. *ACS Appl Energy Mater* 2019; **2**: 5759–5768.
- 2 Estudillo-Wong LA, Luo Y, Díaz-Real JA, Alonso-Vante N. Enhanced oxygen reduction reaction stability on platinum nanoparticles photo-deposited onto oxide-carbon composites. *Appl Catal B Environ* 2016; **187**: 291–300.
- 3 ten Elshof JE, Yuan H, Gonzalez Rodriguez P. Two-Dimensional Metal Oxide and Metal Hydroxide Nanosheets: Synthesis, Controlled Assembly and Applications in Energy Conversion and Storage. *Adv Energy Mater* 2016; **6**: 1600355.
- 4 Mistry H, Varela AS, Kühl S, Strasser P, Cuenya BR. Nanostructured electrocatalysts with tunable activity and selectivity. *Nat Rev Mater* 2016; **1**.  
doi:10.1038/natrevmats.2016.9.
- 5 Kleijn SEF, Lai SCS, Koper MTM, Unwin PR. Electrochemistry of Nanoparticles. *Angew Chemie Int Ed* 2014; **53**: 3558–3586.
- 6 Cheng X, Li Y, Zheng L, Yan Y, Zhang Y, Chen G *et al.* Highly active, stable oxidized platinum clusters as electrocatalysts for the hydrogen evolution reaction. *Energy Environ Sci* 2017; **10**: 2450–2458.
- 7 Shao M, Chang Q, Dodelet J-P, Chenitz R. Recent Advances in Electrocatalysts for Oxygen Reduction Reaction. *Chem Rev* 2016; **116**: 3594–3657.
- 8 Li Y, Hart JL, Taheri ML, Snyder JD. Morphological Instability in Topologically Complex, Three-Dimensional Electrocatalytic Nanostructures. *ACS Catal* 2017; **7**: 7995–8005.
- 9 Huang Z-F, Wang J, Peng Y, Jung C-Y, Fisher A, Wang X. Design of Efficient

- Bifunctional Oxygen Reduction/Evolution Electrocatalyst: Recent Advances and Perspectives. *Adv Energy Mater* 2017; **7**: 1700544.
- 10 Liu J, Jiao M, Lu L, Barkholtz HM, Li Y, Wang Y *et al*. Erratum: High performance platinum single atom electrocatalyst for oxygen reduction reaction. *Nat Commun* 2017; **8**: 16160.
- 11 Matsubu JC, Zhang S, DeRita L, Marinkovic NS, Chen JG, Graham GW *et al*. Adsorbate-mediated strong metal–support interactions in oxide-supported Rh catalysts. *Nat Chem* 2016; **9**: 120–127.
- 12 Xu M, He S, Chen H, Cui G, Zheng L, Wang B *et al*. TiO<sub>2-x</sub>-Modified Ni Nanocatalyst with Tunable Metal–Support Interaction for Water–Gas Shift Reaction. *ACS Catal* 2017; **7**: 7600–7609.
- 13 Cao M, Tang Z, Liu Q, Xu Y, Chen M, Lin H *et al*. The Synergy between Metal Facet and Oxide Support Facet for Enhanced Catalytic Performance: The Case of Pd–TiO<sub>2</sub>. *Nano Lett* 2016; **16**: 5298–5302.
- 14 El-Sawy AM, Mosa IM, Su D, Guild CJ, Khalid S, Joesten R *et al*. Controlling the Active Sites of Sulfur-Doped Carbon Nanotube-Graphene Nanolobes for Highly Efficient Oxygen Evolution and Reduction Catalysis. *Adv Energy Mater* 2016; **6**: 1–12.
- 15 Ruiz-Camacho B, Valenzuela MA, González-Huerta RG, Suarez-Alcantara K, Canton SE, Pola-Albores F. Electrochemical and XAS investigation of oxygen reduction reaction on Pt-TiO<sub>2</sub>-C catalysts. *Int J Hydrogen Energy* 2013; **38**: 12648–12656.
- 16 Riese A, Banham D, Ye S, Sun X. Accelerated Stress Testing by Rotating Disk Electrode for Carbon Corrosion in Fuel Cell Catalyst Supports. *J Electrochem Soc* 2015; **162**: F783–F788.
- 17 Kim JH, Kwon G, Lim H, Zhu C, You H, Kim YT. Effects of transition metal doping in Pt/M-TiO<sub>2</sub> (M = V, Cr, and Nb) on oxygen reduction reaction activity. *J Power*

- Sources* 2016; **320**: 188–195.
- 18 Jia C, Yang P, Chen H-S, Wang J. Template-free Synthesis of mesoporous anatase titania hollow spheres and their enhanced photocatalysis. *CrystEngComm* 2015; **17**: 2940–2948.
  - 19 Ruiz Camacho B, Morais C, Valenzuela MA, Alonso-Vante N. Enhancing oxygen reduction reaction activity and stability of platinum via oxide-carbon composites. *Catal Today* 2013; **202**: 36–43.
  - 20 Damato TC, de Oliveira CCS, Ando RA, Camargo PHC. A Facile Approach to TiO<sub>2</sub> Colloidal Spheres Decorated with Au Nanoparticles Displaying Well-Defined Sizes and Uniform Dispersion. *Langmuir* 2013; **29**: 1642–1649.
  - 21 Jiang X, Herricks T, Xia Y. Monodispersed spherical colloids of titania: Synthesis, characterization, and crystallization. *Adv Mater* 2003; **15**: 1205–1209.
  - 22 Cheng Y, Guo J, Liu X, Sun A, Xu G, Cui P. Preparation of uniform titania microspheres with good electrorheological performance and their size effect. *J Mater Chem* 2011; **21**: 5051–5056.
  - 23 Nassr ABAA, Sinev I, Grünert W, Bron M. PtNi supported on oxygen functionalized carbon nanotubes: In depth structural characterization and activity for methanol electrooxidation. *Appl Catal B Environ* 2013; **142–143**: 849–860.
  - 24 dos Reis FVE, Antonin VS, Hammer P, Santos MC, Camargo PHC. Carbon-supported TiO<sub>2</sub>–Au hybrids as catalysts for the electrogeneration of hydrogen peroxide: Investigating the effect of TiO<sub>2</sub> shape. *J Catal* 2015; **326**: 100–106.
  - 25 Liu C, Tong R, Xu Z, Kuang Q, Xie Z, Zheng L. Efficiently enhancing the photocatalytic activity of faceted TiO<sub>2</sub> nanocrystals by selectively loading  $\alpha$ -Fe<sub>2</sub>O<sub>3</sub> and Pt co-catalysts. *RSC Adv* 2016; **6**: 29794–29801.
  - 26 Wang P, Zhan S, Xia Y, Ma S, Zhou Q, Li Y. The fundamental role and mechanism of

- reduced graphene oxide in rGO/Pt-TiO<sub>2</sub> nanocomposite for high-performance photocatalytic water splitting. *Appl Catal B Environ* 2017; **207**: 335–346.
- 27 Lian Z, Wang W, Li G, Tian F, Schanze KS, Li H. Pt-Enhanced Mesoporous Ti<sup>3+</sup>/TiO<sub>2</sub> with Rapid Bulk to Surface Electron Transfer for Photocatalytic Hydrogen Evolution. *ACS Appl Mater Interfaces* 2017; **9**: 16959–16966.
- 28 Dablemont C, Lang P, Mangeney C, Piquemal JY, Petkov V, Herbst F *et al.* FTIR and XPS study of Pt nanoparticle functionalization and interaction with alumina. *Langmuir* 2008; **24**: 5832–5841.
- 29 Kobayashi H, Teranishi M, Negishi R, Naya S, Tada H. Reaction Mechanism of the Multiple-Electron Oxygen Reduction Reaction on the Surfaces of Gold and Platinum Nanoparticles Loaded on Titanium(IV) Oxide. *J Phys Chem Lett* 2016; **7**: 5002–5007.
- 30 Bedolla-Valdez ZI, Verde-Gómez Y, Valenzuela-Muñoz AM, Gochi-Ponce Y, Oropeza-Guzmán MT, Berhault G *et al.* Sonochemical synthesis and characterization of Pt/CNT, Pt/TiO<sub>2</sub>, and Pt/CNT/TiO<sub>2</sub> electrocatalysts for methanol electro-oxidation. *Electrochim Acta* 2015; **186**: 76–84.
- 31 Xia BY, Wang B, Wu H Bin, Liu Z, Wang X, (David) Lou XW. Sandwich-structured TiO<sub>2</sub>–Pt–graphene ternary hybrid electrocatalysts with high efficiency and stability. *J Mater Chem* 2012; **22**: 16499.
- 32 Qin Y-H, Li Y, Lv R-L, Wang T-L, Wang W-G, Wang C-W. Enhanced methanol oxidation activity and stability of Pt particles anchored on carbon-doped TiO<sub>2</sub> nanocoating support. *J Power Sources* 2015; **278**: 639–644.
- 33 Wu G, Hu Y, Liu Y, Zhao J, Chen X, Whoehling V *et al.* Graphitic carbon nitride nanosheet electrode-based high-performance ionic actuator. *Nat Commun* 2015; **6**: 7258.
- 34 Zhou J-H, Sui Z-J, Zhu J, Li P, Chen D, Dai Y-C *et al.* Characterization of surface

- oxygen complexes on carbon nanofibers by TPD, XPS and FT-IR. *Carbon N Y* 2007; **45**: 785–796.
- 35 Ganguly A, Sharma S, Papakonstantinou P, Hamilton J. Probing the Thermal Deoxygenation of Graphene Oxide Using High-Resolution In Situ X-ray-Based Spectroscopies. *J Phys Chem C* 2011; **115**: 17009–17019.
- 36 Assumpção MHMT, De Souza RFB, Rascio DC, Silva JCM, Calegari ML, Gaubeur I *et al.* A comparative study of the electrogeneration of hydrogen peroxide using Vulcan and Printex carbon supports. *Carbon N Y* 2011; **49**: 2842–2851.
- 37 Assumpção MHMT, Moraes A, De Souza RFB, Calegari ML, Lanza MRV, Leite ER *et al.* Influence of the preparation method and the support on H<sub>2</sub>O<sub>2</sub> electrogeneration using cerium oxide nanoparticles. *Electrochim Acta* 2013; **111**: 339–343.
- 38 Salgado JRC, Paganin VA, Gonzalez ER, Montemor MF, Tacchini I, Ansón A *et al.* Characterization and performance evaluation of Pt-Ru electrocatalysts supported on different carbon materials for direct methanol fuel cells. *Int J Hydrogen Energy* 2013; **38**: 910–920.
- 39 Lewera A, Timperman L, Roguska A, Alonso-Vante N. Metal–Support Interactions between Nanosized Pt and Metal Oxides (WO<sub>3</sub> and TiO<sub>2</sub>) Studied Using X-ray Photoelectron Spectroscopy. *J Phys Chem C* 2011; **115**: 20153–20159.
- 40 Ma J, Habrioux A, Morais C, Lewera A, Vogel W, Verde-Gómez Y *et al.* Spectroelectrochemical Probing of the Strong Interaction between Platinum Nanoparticles and Graphitic Domains of Carbon. *ACS Catal* 2013; **3**: 1940–1950.
- 41 López-Cudero A, Solla-Gullón J, Herrero E, Aldaz A, Feliu JM. CO electrooxidation on carbon supported platinum nanoparticles: Effect of aggregation. *J Electroanal Chem* 2010; **644**: 117–126.
- 42 Zheng Y, Chen H, Dai Y, Zhang N, Zhao W, Wang S *et al.* Preparation and



characterization of Pt/TiO<sub>2</sub> nanofibers catalysts for methanol electro-oxidation.

*Electrochim Acta* 2015; **178**: 74–79.

- 43 Lima FHB, Lizcano-Valbuena WH, Teixeira-Neto E, Nart FC, Gonzalez ER, Ticianelli EA. Pt-Co/C nanoparticles as electrocatalysts for oxygen reduction in H<sub>2</sub>SO<sub>4</sub> and H<sub>2</sub>SO<sub>4</sub>/CH<sub>3</sub>OH electrolytes. *Electrochim Acta* 2006; **52**: 385–393.
- 44 Ruiz-Camacho B, Martínez-Álvarez O, Rodríguez-Santoyo HH, Granados-Alejo V. Pt/C and Pt/TiO<sub>2</sub>-C electrocatalysts prepared by chemical vapor deposition with high tolerance to alcohols in oxygen reduction reaction. *J Electroanal Chem* 2014; **725**: 19–24.
- 45 Ferrero GA, Preuss K, Marinovic A, Jorge AB, Mansor N, Brett DJL *et al.* Fe-N-Doped Carbon Capsules with Outstanding Electrochemical Performance and Stability for the Oxygen Reduction Reaction in Both Acid and Alkaline Conditions. *ACS Nano* 2016; **10**: 5922–5932.
- 46 Shih YH, Sagar GV, Lin SD. Effect of electrode Pt loading on the oxygen reduction reaction evaluated by rotating disk electrode and its implication on the reaction kinetics. *J Phys Chem C* 2008; **112**: 123–130.
- 47 Santos LGRA, Freitas KS, Ticianelli EA. Heat treatment effect of Pt-V/C and Pt/C on the kinetics of the oxygen reduction reaction in acid media. *Electrochim Acta* 2009; **54**: 5246–5251.
- 48 Demarconnay L, Coutanceau C, Léger J-M. Study of the oxygen electroreduction at nanostructured PtBi catalysts in alkaline medium. *Electrochim Acta* 2008; **53**: 3232–3241.
- 49 Zhou R, Zheng Y, Jaroniec M, Qiao SZ. Determination of the Electron Transfer Number for the Oxygen Reduction Reaction: From Theory to Experiment. *ACS Catal* 2016; **6**: 4720–4728.

- 50 Tiido K, Alexeyeva N, Couillard M, Bock C, MacDougall BR, Tammeveski K. Graphene-TiO<sub>2</sub> composite supported Pt electrocatalyst for oxygen reduction reaction. *Electrochim Acta* 2013; **107**: 509–517.
- 51 Tammeveski K. The Reduction of Oxygen on Pt-TiO<sub>2</sub> Coated Ti Electrodes in Alkaline Solution. *J Electrochem Soc* 1999; **146**: 669.
- 52 Shinagawa T, Garcia-Esparza AT, Takanabe K. Insight on Tafel slopes from a microkinetic analysis of aqueous electrocatalysis for energy conversion. *Sci Rep* 2015; **5**: 1–21.
- 53 Elezovic NR, Babic BM, Radmilovic VR, Vracar LM, Krstajic N V. Nb-TiO<sub>2</sub> supported platinum nanocatalyst for oxygen reduction reaction in alkaline solutions. *Electrochim Acta* 2011; **56**: 9020–9026.
- 54 Li L, Wei Z, Zhang Y, Qi X, Xia M, Zhang J *et al.* DFT study of difference caused by catalyst supports in Pt and Pd catalysis of oxygen reduction reaction. *Sci China Ser B Chem* 2009; **52**: 571–578.
- 55 Huang K, Sasaki K, Adzic RR, Xing Y. Increasing Pt oxygen reduction reaction activity and durability with a carbon-doped TiO<sub>2</sub> nanocoating catalyst support. *J Mater Chem* 2012; **22**: 16824.
- 56 Shanmugam S, Gedanken A. Carbon-coated anatase TiO<sub>2</sub> nanocomposite as a high-performance electrocatalyst support. *Small* 2007; **3**: 1189–1193.

## **Chapter 5 – Shape controlled Pd/Fe<sub>2</sub>O<sub>3</sub> towards the selective hydrogenation of styrene epoxide**

### **5.1 – Introduction**

The interest towards 2-phenyl ethanol for industrial applications can be attributed to its various properties, from its odor of roses to antifungal and antibacterial properties.<sup>1</sup> This alcohol has been used for the manufacture of cosmetics, food additives, as precursors for polymers, in the preparation of detergents, or even as starting material for other chemicals.<sup>2</sup> The usual production of this molecule happens through catalytic procedures such as the Friedel-Krafts alkylation of benzene.<sup>3</sup> Such reaction employs AlCl<sub>3</sub> as catalyst and 2-chloroethanol and benzene as reagents, producing 2-phenyl ethanol and hydrochloric acid, which has to be neutralized and discarded, a process that adds a step onto the production and that requires an acid-resistant reactor.<sup>3</sup> Another procedure employed to its output is via a Grignard precursor, generating as side products both MgSO<sub>4</sub> and HBr and requires another separation and purification method.<sup>4</sup>

To avoid the shortcomings of using such procedures and move towards more green conditions, the catalytic hydrogenation of styrene oxide is a promising alternative. Since this reaction may produce many side products, tailoring the catalyst to improve the selectivity is needed.<sup>5</sup> Palladium is a noble metal known for its excellent ability in hydrogenations,<sup>6</sup> in previous reports, it was shown that this metal presented the highest conversion rates of styrene oxide.<sup>7</sup> There have been reports of catalysts of Pd/C,<sup>3</sup> Pd/chitosan,<sup>1</sup> Pd/MgO and Pd/Al<sub>2</sub>O<sub>4</sub>,<sup>7</sup> or even a Pd/Hidrotalcite.<sup>8</sup> However, they still require high temperatures, pressures, or reaction time. When Pd is deposited onto an acid support, it has been shown that it tends to form isomerization products such as phenylacetaldehyde or hydrogenate styrene oxide onto 1-phenyl ethanol.<sup>9</sup> Thus, employing a basic oxide such as Fe<sub>2</sub>O<sub>3</sub> can benefit the

system to improve the selectivity towards 2-phenyl ethanol.<sup>10</sup> Aside from being the most stable phase of the iron oxide group, hematite is also inexpensive. Furthermore, by controlling its shape, it is possible to improve its interaction with certain molecular groups.<sup>11</sup>

In this chapter, we explore the use of shape-controlled Pd/Fe<sub>2</sub>O<sub>3</sub> as nanocatalyst for the selective hydrogenation of styrene oxide, aiming at improving the selectivity and understanding the reaction pathway that our catalysts provide. Our material is comprised of Palladium nanoparticles (Pd NPs) supported onto Fe<sub>2</sub>O<sub>3</sub> microcubes. We also have the objective of verifying the effect of various reaction conditions over the production of 2-phenyl ethanol.

## 5.2 – Experimental Section

### *Chemicals and instrumentation*

$\text{Fe}(\text{NO}_3)_3 \cdot 9\text{H}_2\text{O}$  (Iron(III) nitrate nonahydrate, 99.0%, Sigma-Aldrich),  $\text{Zn}(\text{CH}_3\text{COO})_2 \cdot 2\text{H}_2\text{O}$  (Zinc(II) acetate dihydrate,  $\geq 98\%$ , Sigma-Aldrich),  $\text{NH}_4\text{OH}$  (Ammonium hydroxide, Synth),  $\text{K}_2\text{PdCl}_4$  (Potassium tetrachloropalladate, 98.0%, Sigma-Aldrich), PVP (polyvinylpyrrolidone, Sigma-Aldrich, MW 55 000 g mol<sup>-1</sup>),  $\text{C}_6\text{H}_4(\text{OH})_2$  (Hydroquinone,  $\geq 99\%$ , Sigma-Aldrich),  $\text{C}_3\text{H}_6\text{O}$  (acetone, 99.5%, Synth),  $\text{C}_2\text{H}_6\text{O}$  (ethanol, 95%, Synth),  $\text{C}_8\text{H}_6$  (Phenylacetylene,  $\geq 98\%$ , Sigma-Aldrich),  $\text{C}_8\text{H}_8$  (Styrene,  $\geq 99\%$ , Sigma-Aldrich),  $\text{C}_8\text{H}_{10}$  (Ethylbenzene, 99.8%, Sigma-Aldrich),  $\text{C}_8\text{H}_8\text{O}$  (Styrene oxide, 97%, Sigma-Aldrich),  $\text{C}_8\text{H}_{10}\text{O}$  (1-Phenylethanol, 98%, Sigma-Aldrich),  $\text{C}_8\text{H}_{10}\text{O}$  (2-Phenylethanol,  $\geq 99\%$ , Sigma-Aldrich),  $\text{C}_8\text{H}_8\text{O}$  (Acetophenone, 99%, Sigma-Aldrich),  $\text{C}_8\text{H}_8\text{O}$  (Phenylacetaldehyde,  $\geq 95\%$ , Sigma-Aldrich),  $\text{C}_3\text{H}_7\text{ON}$  (N,N-Dimethylformamide, anhydrous, 99.8%, Sigma-Aldrich), and Pd/C (Palladium on carbon, 10 wt.%, Sigma-Aldrich) were used as received. All chemicals were analytical grade reagents. Deionized water (18.2 M $\Omega$ ) was used throughout the experiments.

A JEOL FEG-SEM JSM 6330F microscope operated at 5 kV was used to obtain scanning electron microscopy images. Aqueous suspensions of the samples were drop-casted on top of a silicon wafer and let dry under room temperature. A Tecnai FEI G20 microscope operated at 200 kV was used to capture transmission electron microscopy images. A suspension of each sample on isopropanol was drop-casted on a carbon-coated copper grid. The size distribution profile was determined by measuring 200 particles from our TEM images.

A Renishaw Raman System 3000 equipped with a CCD detector and coupled to a microscope was used to acquire Raman spectra. The laser beam was focused on the sample by using a 50 $\times$  lens. All spectra were acquired in a single scan with 10 seconds accumulation

time. Experiments were performed in a back-scattering geometry under ambient conditions. All samples were irradiated using a (He–Ne) 632.8 nm line with controlled laser power outputs.

A Bruker D2 Phaser equipment was employed to acquire X-ray diffraction patterns of the samples. A standard Cu K $\alpha$  source was employed ( $1\frac{1}{4}$  1.54060 Å, 30 kV, 15 mA). The integration time was set to 0.75 s and step to 0.03°, with 2 $\theta$  ranging from 20 to 80°. XRD samples were prepared by placing the samples on an acrylic sample holder. Thermogravimetric assays were performed using thermal analysis Shimadzu TGA Q500 equipment from TA Instruments. The procedure was performed by placing  $\approx$ 7.0 mg of dried sample in an open platinum crucible under a 60 mL min<sup>-1</sup> air flow and heating it from room temperature to 950 °C with a heating rate of 5 °C min<sup>-1</sup>. Pd and Fe contents were determined through flame atomic absorption spectrophotometry (FAAS) using a Shimadzu AA-6300 equipment, samples were digested using freshly prepared aqua regia.

The H<sub>2</sub> – temperature-programmed reduction assays were performed using a Quantachrome ChemBET PULSAR TPR/TPD instrument. 40 mg of sample was placed in the TPR quartz tube, sandwiched between layers of quartz wool with a thermocouple placed in contact with the sample. The TPR tube was then placed in the instrument for measurements. The material was firstly heated up to 120°C, to remove adsorbed water, and left at this temperature for 25 minutes under nitrogen flow. It was then cooled to room temperature and left stabilize with hydrogen for 15 minutes. The reduction of our catalysts (5% H<sub>2</sub> in N<sub>2</sub> flowing through the TPR tube at 20 mL·min<sup>-1</sup> at a temperature ramp of 10°C min<sup>-1</sup> from 25 to 1000°C then cooling to room temperature) was carried out to reduce the Pd<sub>2+</sub> and Fe<sub>3+</sub> within the sample. The consumption of hydrogen gas changed the conductivity of the gas stream; Thus, the change in conductivity was measured and calibrated as a function of both

temperature and time to produce the TPR profile. The instrument was calibrated using a high purity CuO.

For catalytic reactions, the experiments were performed inside a Fischer-Porter glass reactor adapted with a pressure valve to set the desired pressure. These reactors were purged with the desired gas five times before reactions. After finalizing the reactions, the pressure was relieved, and the catalysts were separated from the solution by centrifugation. Before analysis, the solutions were also filtered.

In a typical procedure, 2 mg of catalyst was weighed, placed in the reactor, then, the substrate was added based on the desired molar ratio (Pd/Styrene Oxide), followed by the addition of dimethylformamide as solvent to complete 2 mL of total volume. The mixture was sealed and quickly sonicated for better dispersion of the catalyst. Hydrogen was purged, and the desired pressure was set. The reactor was then put in an oil bath at the desired temperature. For kinetic measurements, a small sample (50  $\mu$ L) was removed from the reactor under N<sub>2</sub> flow, centrifuged and analyzed promptly.

For reuse tests, the catalysts were removed from the reaction medium using centrifugation (5000 rpm, 5 min) and washed with acetone three times, dried under vacuum and resuspended in DMF. For XPS, these samples were removed and washed inside a glovebox.

All products were quantified using a Shimadzu GC-2010 Plus gas chromatograph with a Restek RTX®-Wax column. To confirm the molecules obtained on each reaction, a Gas Chromatograph (Agilent 7890B) coupled with a Mass Spectrometer, a Thermal Conductivity Detector, and a Flame Ionization Detector was employed. In this case, an HP-INNOWax column was employed, and the sample split between detectors. The method employed consisted on a flow of 2 mL min<sup>-1</sup>, starting at 50°C with a ramp of 10°C up to 130°C and

increasing at a 15°C to 200°C which it was left for 3 minutes. The products presented definite and symmetric peaks.

#### *Synthesis of Fe<sub>2</sub>O<sub>3</sub> microcubes*<sup>12</sup>

In a typical procedure, 5.7 g of Fe(NO<sub>3</sub>)<sub>3</sub>·9H<sub>2</sub>O were added to 70 mL of deionized water and stirred until all the salt was dissolved. Then, 768 mg of Zn(CH<sub>3</sub>COO)<sub>2</sub>·2H<sub>2</sub>O were added and stirred for 10 minutes at room temperature, followed by the addition of 70 mL of concentrated NH<sub>4</sub>OH, forming a brown precipitate. This mixture was then stirred for 15 min at room temperature and transferred to a Teflon-lined steel autoclave (220 mL), heated up to 160°C, treated for 16 hours and let cool to room temperature. After cooling, it was separated using centrifugation, washed with water (5 times, 5000 rpm 5 min) and ethanol (2 times, 5000 rpm, 5 min). After the last wash, the sample was dried under vacuum, producing about 2.0 grams of Fe<sub>2</sub>O<sub>3</sub> microcubes.

#### *Synthesis of Pd NPs onto Fe<sub>2</sub>O<sub>3</sub> microcubes*<sup>13</sup>

To decorate the pre-formed microcubes, a suspension of Fe<sub>2</sub>O<sub>3</sub> cubes was prepared by adding 200 mg of the powder to 10 mL of water and leaving it under ultrasound for 10 minutes. Then, 30 mL of a 10 mmol L<sup>-1</sup> aqueous solution of hydroquinone was added to the mixture, followed by the addition of 50 mL of a 7 g L<sup>-1</sup> aqueous solution of PVP 55.000. This mixture was kept under stirring for 10 minutes at 90°C. At last, 30 mL of K<sub>2</sub>PdCl<sub>4</sub> 4 mM was added to the mixture, and left for 1 hour at 90°C under vigorous stirring, producing the Pd/Fe<sub>2</sub>O<sub>3</sub> materials, which were then washed 5 times with ethanol (4000 rpm, 5 min), and left to dry overnight in a vacuum oven at 70°C. To prepare Pd/Fe<sub>2</sub>O<sub>3</sub> ATT, the samples were placed in a furnace and heated up to 400°C for 1 hour with airflow (10 mL/min) and let cool down to room temperature.



### 5.3 – Results and Discussion

We started by synthesizing shape-controlled iron oxide quasi-cubes as supports for Pd NPs. This material was designed aiming at preparing a catalyst with enhanced selectivity to the anti-Markovnikov product on styrene oxide hydrogenation (2-phenyl ethanol).<sup>14</sup> The procedure used to prepare our support is based on the precipitation of ferrite nanocrystals ( $\text{MFe}_2\text{O}_4$ ) employing  $\text{Zn}(\text{CH}_3\text{CO}_2)_2$  as the structure-directing agent, which is efficiently removed during the hydrothermal step of the synthesis.<sup>12</sup> This support presents a very well-tailored quasi-cubic shape with sizes ranging from  $498.9 \pm 69.6$  nm (SEM on **Figure 5.1A**).

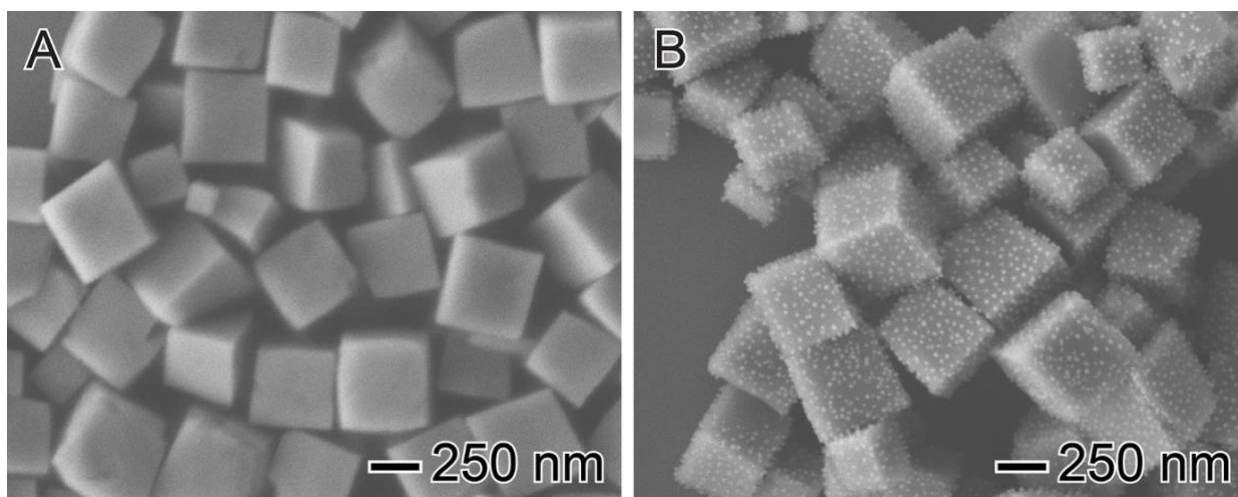


**Figure 5.1** – SEM images of  $\text{Fe}_2\text{O}_3$  microcubes as prepared (A) and decorated with Pd NPs (B). The  $\text{Fe}_2\text{O}_3$  cubes measure  $498.9 \pm 69.6$  nm while the Pd NPs measure  $34.5 \pm 2.5$

The next step was based on the deposition of Pd NPs onto the controlled support. We employed an in-situ reduction of the  $\text{K}_2\text{PdCl}_4$  precursor using hydroquinone as reducing agent and PVP as stabilizer.<sup>13</sup> This procedure granted monodisperse spherical Pd NPs with  $34.5 \pm 2.5$  nm sizes (SEM on **Figure 5.1B**, TEM on **Figure 5.2A**). This sample presented 8.6 wt.% of Pd, measured by FAAS and confirmed by ICP-OES.

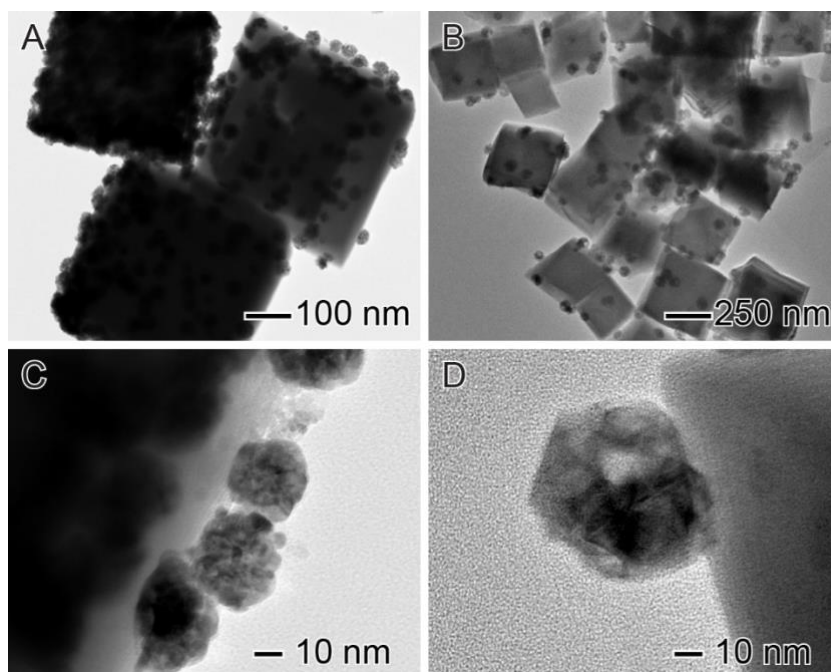


**Figure 5.2** – TEM images of Pd NPs supported onto Fe<sub>2</sub>O<sub>3</sub> microcubes before (A and C) and after (B and D) thermal treatment at 400°C. The Pd NPs measure  $34.5 \pm 2.5$  and  $64.9 \pm 7.7$  nm, respectively, in the samples before and after thermal treatment. The Fe<sub>2</sub>O<sub>3</sub> cubes measure  $498.9 \pm 69.6$  nm.

Raman spectroscopy, **Figure 5.3**, showed no significant changes in the profile of the material after depositing Pd on the Fe<sub>2</sub>O<sub>3</sub> surface,<sup>15</sup> with both samples presenting peaks at 222.7 cm<sup>-1</sup>, and 498.54 cm<sup>-1</sup> assigned to the A<sub>1g</sub> phonon modes of this oxide and peaks at 243.8 cm<sup>-1</sup>, 289.19 cm<sup>-1</sup>, 404.89 cm<sup>-1</sup>, and 606.00 cm<sup>-1</sup> assigned to its E<sub>g</sub> phonon modes.<sup>16</sup> Furthermore, the clear peak observed at 660.00 cm<sup>-1</sup> could be mistaken for the magnetite phase of this oxide, yet, several studies assign it as an infrared-active longitudinal optical (LO) E<sub>u</sub> mode of Fe<sub>2</sub>O<sub>3</sub> related to the level of disorder in its crystal lattice.<sup>17</sup>

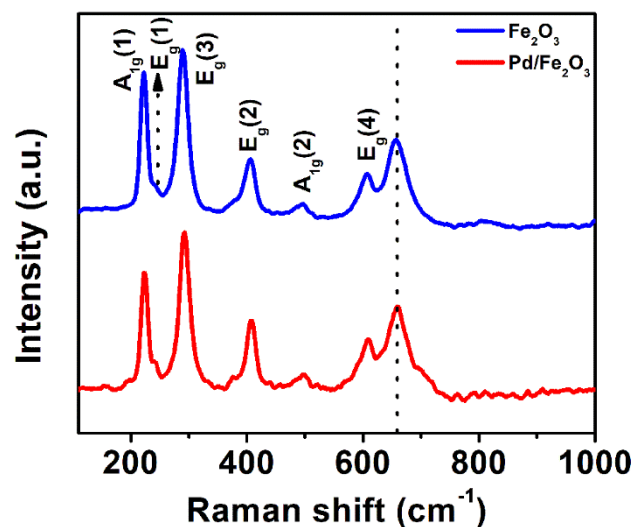


**Figure 5.3** – Raman spectroscopy analyses of  $\text{Fe}_2\text{O}_3$  microcubes (blue line) and  $\text{Pd}/\text{Fe}_2\text{O}_3$  BTT (red line). The general profile of the spectra is maintained, indicating that both materials contain the hematite phase of  $\text{Fe}_2\text{O}_3$ .

Even though the materials are thoroughly washed with both water and acetone, studies show that some PVP usually is maintained on the surface of NPs even after washed.<sup>18–20</sup> A thermogravimetric analysis of our samples, **Figure 5.4**, displayed about 0.5 wt.% water content in the sample (first mass loss from 25°C to 200°C) and close to 2.0 wt.% of organic matter (second mass loss from 200°C to 344°C) which could be assigned to the remaining PVP. The analysis reached its minimum weight at 344°C. For this reason, we employed a thermal treatment to remove any other organic molecules on the catalyst surface at a slightly higher temperature (400°C). It led to a change in the Pd morphology, which grew to about  $64.9 \pm 7.7$  nm, **Figure 5.2B**. These images also show that the number of NPs on the samples before thermal treatment ( $\text{Pd}/\text{Fe}_2\text{O}_3$  BTT) is more significant than on the sample after thermal treatment ( $\text{Pd}/\text{Fe}_2\text{O}_3$  ATT), indicating coalescence of Pd particles, yet the cubes were kept intact. Another aspect worth mentioning is the morphology change, as more closely displayed in **Figure 5.2C and 5.2D**. The Pd particles on  $\text{Pd}/\text{Fe}_2\text{O}_3$  BTT display a rounder surface,

formed by circular particles (**Figure 5.1C**), while the Pd NPs on Pd/Fe<sub>2</sub>O<sub>3</sub> ATT, presented sharper edges, with clear lines and points seen on the TEM image (**Figure 5.2C**).

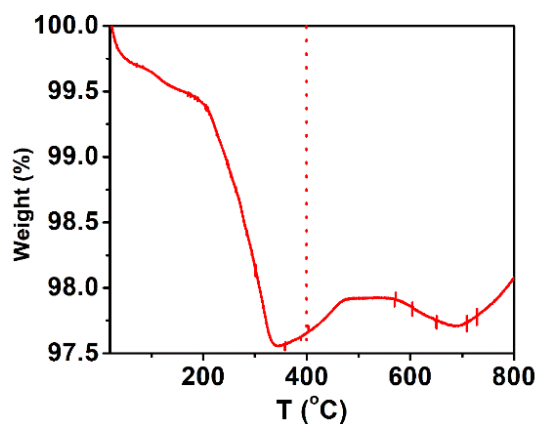


**Figure 5.4** – Thermogravimetric analysis of as-prepared Pd/Fe<sub>2</sub>O<sub>3</sub> performed under air with a heating rate of 5°C min<sup>-1</sup>. The evident decrease between 200°C and 400°C could be attributed to the combustion of organic matter adsorbed onto the material surface.

Some further differences between these materials are seen on their X-Ray diffractogram, **Figure 5.5**, which displays the iron oxide sample (blue line), and the Pd/Fe<sub>2</sub>O<sub>3</sub> samples before (red line), and after thermal treatment (black line). All samples displayed the diffraction pattern assigned to the hematite phase of Fe<sub>2</sub>O<sub>3</sub>,<sup>15,16</sup> and while the as-prepared Fe<sub>2</sub>O<sub>3</sub> sample had crystallite sizes of 53.6 nm based on Scherrer's equation.<sup>21</sup> The samples with Pd NPs presented iron oxide crystallites with lower sizes, 49.0 nm for the sample before thermal treatment, and 48.1 nm for the sample after thermal treatment, a value that is very similar to the before-mentioned, indicating no change in structure. For the Pd NPs, at 39°, the mean crystallite size for Pd/Fe<sub>2</sub>O<sub>3</sub> BTT was of 0.8 nm while for Pd/Fe<sub>2</sub>O<sub>3</sub> ATT they measured 19.5 nm, in this sample we could also obtain the value for PdO nanocrystallites from its peak at 34°, which measured 7.4 nm.<sup>22</sup> These results were expected based on the TEM images.

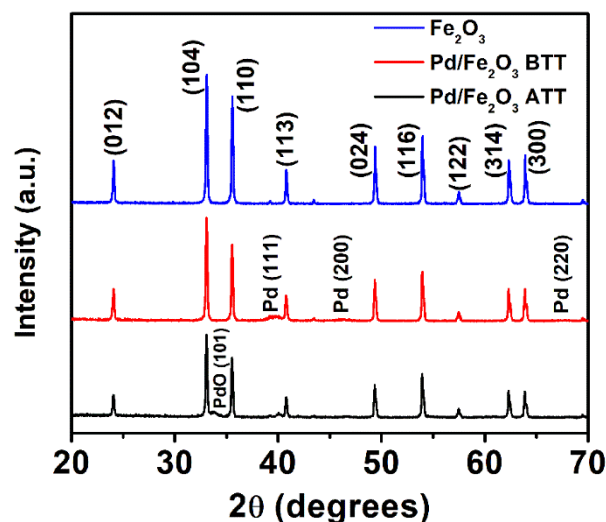


**Figure 5.5** – X-Ray diffractograms of the iron (III) oxide microcubes (blue line) and the analogous with Pd before (red line) and after thermal treatment (black line). These diffractograms confirmed the presence of 100% hematite phase with its standard peaks labeled on top of the diffractograms. One can also notice the presence of different Pd species on each material, while the material before thermal treatment displayed only Pd<sub>0</sub> peaks, the one after thermal treatment showed a clear PdO peak.

To further characterize our samples, we performed H<sub>2</sub>-Temperature Programmed Reduction (TPR), an experiment in which our sample was treated at 10°C min<sup>-1</sup> under a 20 mL min<sup>-1</sup> flow of H<sub>2</sub> 5% in N<sub>2</sub> (**Figure 5.6**). Through these results, we can have information about the average oxidation state of our materials. The TPR profile of Fe<sub>2</sub>O<sub>3</sub> is typically characterized by three peaks, the initial one, due to the reduction of Fe<sup>3+</sup> to Fe<sup>2+</sup>, generating Fe<sub>3</sub>O<sub>4</sub>. As seen on **Figure 5.6A**, this peak suffered a shift, while for the iron oxide sample it was located at 443°C, for the Pd/Fe<sub>2</sub>O<sub>3</sub> samples they were found at 364°C for the sample before thermal treatment and at 320°C for the sample after thermal treatment. As for the next peak, indicating the reduction of Fe<sub>3</sub>O<sub>4</sub> to FeO, it is seen as a small shoulder between 600°C and 625°C for all three samples. The last peak, the broad one, indicates the reduction of FeO

to Fe<sub>0</sub>, and we can see that for all samples they finished in different temperatures 907°C for Fe<sub>2</sub>O<sub>3</sub>, 782°C for Pd/Fe<sub>2</sub>O<sub>3</sub> BTT and 850°C for Pd/Fe<sub>2</sub>O<sub>3</sub> ATT.

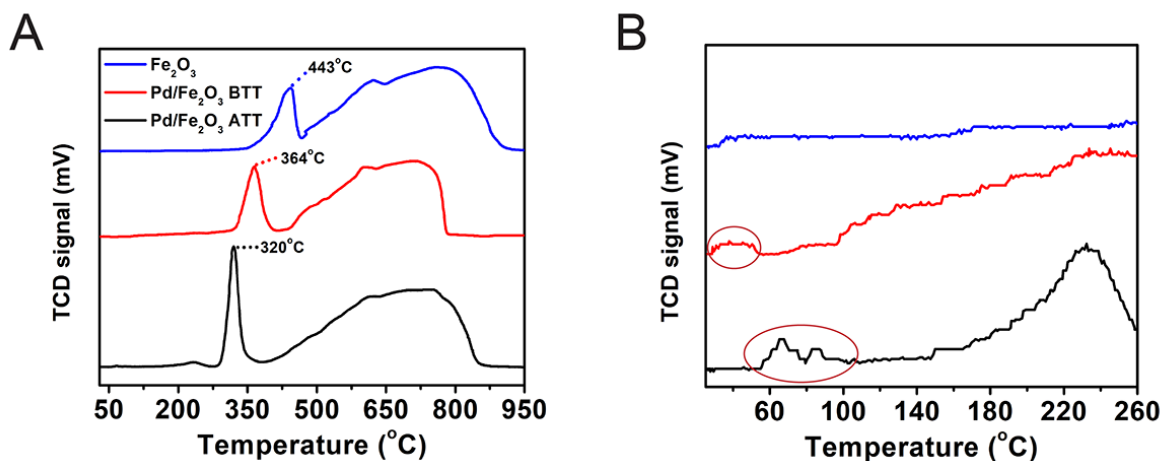


**Figure 5.6** – (A) Temperature programmed reduction of Fe<sub>2</sub>O<sub>3</sub> materials using a 5% H<sub>2</sub>/N<sub>2</sub> flow (20 mL min<sup>-1</sup>), as prepared Fe<sub>2</sub>O<sub>3</sub> sample (blue line), Pd/Fe<sub>2</sub>O<sub>3</sub> sample before thermal treatment (red line), and after thermal treatment (black line), we notice shifts throughout the entire graph, which indicates modifications on the surface of these materials. (B) zoom of the temperatures between 25°C and 260°C to display smaller peaks that may have appeared.

A small broad peak can also be seen at on the sample Pd/Fe<sub>2</sub>O<sub>3</sub> ATT, located at 232°C, based on the literature, Pd NPs are known to reduce at temperatures lower than 200°C.<sup>23,24</sup> Thus, this reduction peak could either be associated to the PdO on the interface,<sup>25,26</sup> or with the reduction of iron oxide, as there are reports on the literature showing the reduction of Fe<sub>2</sub>O<sub>3</sub> between 200°C and 300°C.<sup>25</sup> To verify the presence of reduction peaks at lower temperatures, we zoomed-in at the TPR profiles between 25°C and 260°C, **Figure 5.6B**. We can see some small peaks on the Pd-decorated samples, circled on the figure, which could be associated with the reduction of PdO, and since the Pd/Fe<sub>2</sub>O<sub>3</sub> BTT sample has smaller NPs, it makes sense that the peaks are shifted to lower temperatures.<sup>26</sup>

After characterizing the samples, our catalytic assays were performed for the room temperature, low-pressure hydrogenation of styrene oxide (**Figure 5.7**), this reaction is known for its many products and side products, yet the dimers and polymers originated from side

reactions were not illustrated, it is also known that they could appear depending on the conditions applied.<sup>27,28</sup> Styrene oxide, the reagent, could suffer isomerization in the presence of a Lewis acid, to form phenylacetaldehyde (A),<sup>29,30</sup> which is known to polymerize at room temperature.<sup>27,28</sup> This product could also be hydrogenated to 2-phenyl ethanol (B), which is a direct product of the hydrogenation of our reagent. As a second product, our reagent can produce 1-phenyl ethanol (C), and if a deoxygenation reaction occurs, styrene (D) appears and can be further hydrogenated to ethylbenzene.<sup>31</sup>

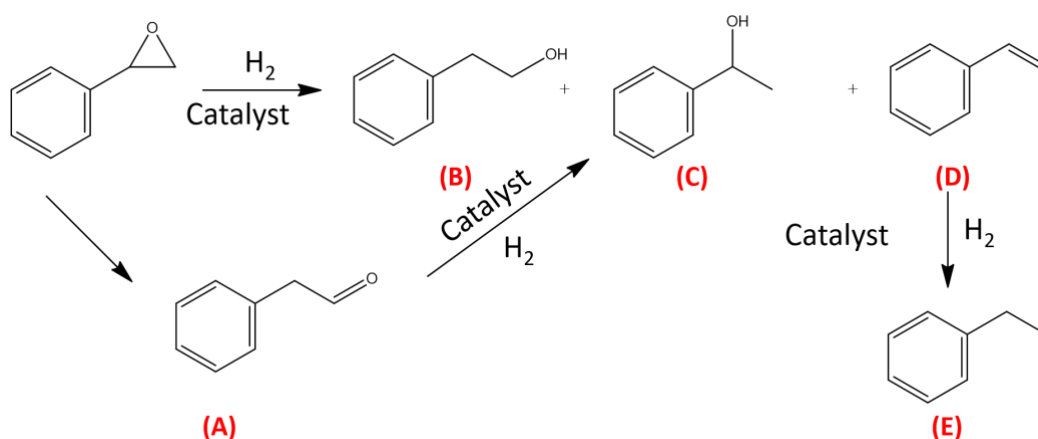


**Figure 5.7** – Styrene oxide catalytic hydrogenation reaction. The reagent, styrene oxide, can undergo an isomerization forming phenylacetaldehyde (A), while at the same time it can be hydrogenated to 2-phenyl ethanol (B), 1-phenyl ethanol (C), or suffer a deoxygenation producing styrene (D), which could get further hydrogenated to ethylbenzene (E).

Pd catalysts usually tend to over-hydrogenate molecules under high pressure,<sup>32</sup> for this reason, we performed our reactions employing 1 bar of hydrogen and 30°C as temperature, and due to a better dispersion of our catalyst, dimethylformamide was used as solvent. For the molar ratio (Pd/Styrene oxide), we performed tests employing the Pd/Fe<sub>2</sub>O<sub>3</sub> material before thermal treatment, obtaining the results illustrated in **Table 5.1**. Since the 60 molar ratio (Pd/Styrene Oxide) for 1 hour of reaction produced a high conversion but not 100%, we decided to employ these conditions to allow the conversion to go either up or down for any other changes in conditions.

**Table 5.1** – Tests of molar ratio (Pd/Styrene Oxide) employed to choose the correct molar ratio for the catalytic hydrogenation of Styrene oxide. Selectivity (%) towards phenylacetaldehyde (A), 2-phenyl ethanol (B), 1-phenyl ethanol (C), styrene (D), and ethylbenzene (E).

Molar Ratio	Conversion	(A)	(B)	(C)	(D)	(E)
<b>20 (1h)</b>	100%	4.6%	95.4%	0%	0%	0%
<b>20 (2h)</b>	100%	1.3%	98.7%	0%	0%	0%
<b>30 (1h)</b>	98.8%	5.6%	94.4%	0%	0%	0%
<b>60 (1h)</b>	86.8%	8.2%	91.8%	0%	0%	0%

Through these tests, we anticipated that phenylacetaldehyde was being converted into 2-phenyl ethanol since when the reaction time changed from 1 to 2 hours, the concentration of phenylacetaldehyde dropped. And when the concentration of styrene oxide in the mixture was higher, there was a higher production of phenylacetaldehyde. Thus, we decided to study the kinetics of hydrogenation for both catalysts, **Figure 5.8**. For the catalyst after thermal treatment, the molar ratio (Pd/Styrene Oxide) had to be increased three times (180) due to the higher conversion of the catalyst, which can be justified by the fact that organic matter on its surface was probably blocking catalytic sites, thus, when it was calcinated under air, this layer was removed exposing the sites. Another interesting fact was that while the catalyst Pd/Fe<sub>2</sub>O<sub>3</sub> BTT (**Figure 5.8A**) displayed a high selectivity towards 2-phenyl ethanol, the Pd/Fe<sub>2</sub>O<sub>3</sub> ATT (**Figure 5.8B**) displayed a mixed profile with phenylacetaldehyde being the dominant product in the beginning and getting converted into 2-phenyl ethanol and other products after the reaction reached 100% of conversion.



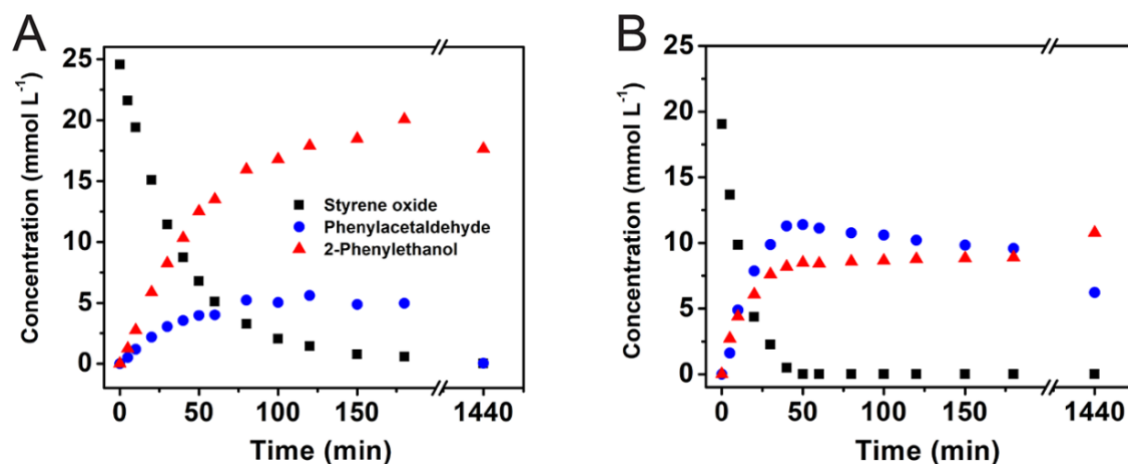


**Figure 5.8** – Kinetics of styrene oxide (black squares) hydrogenation to 2-Phenylethanol (red triangles) and Phenylacetaldehyde (blue spheres) using the Pd/Fe<sub>2</sub>O<sub>3</sub> catalyst as prepared (A) and after thermal treatment at 400°C (B). Here, differences in the selectivity of both catalysts are seen, indicating that the treatment significantly changed the catalytic sites exposed on the material.

As for the kinetic constants for each reaction, while the Pd/Fe<sub>2</sub>O<sub>3</sub> BTT produced a first-order kinetic constant of  $25.43 \times 10^{-3} \text{ min}^{-1}$ , the Pd/Fe<sub>2</sub>O<sub>3</sub> ATT displayed a constant of  $70.74 \times 10^{-3} \text{ min}^{-1}$ , even at a higher molar ratio (Pd/Styrene Oxide). Which further shows that although the NPs are twice as big as the ones before treatment, their activity is a lot higher. For comparison, we employed 6 bar as the hydrogen pressure with the Pd/Fe<sub>2</sub>O<sub>3</sub> BTT catalyst. Results can be seen in **Figure 5.9**. This test showed that at a higher hydrogen pressure, the selectivity towards 2-phenyl ethanol increased, as well as the kinetic constant, reaching a value of  $49.35 \times 10^{-3} \text{ min}^{-1}$ , which was twice the value of the same reaction at 1 bar. This was expected, since once the pressure is increased, the number of effective collisions between gases and the catalyst is higher than before, and the internal energy of the system also increases, leading to a higher yield.<sup>33</sup>

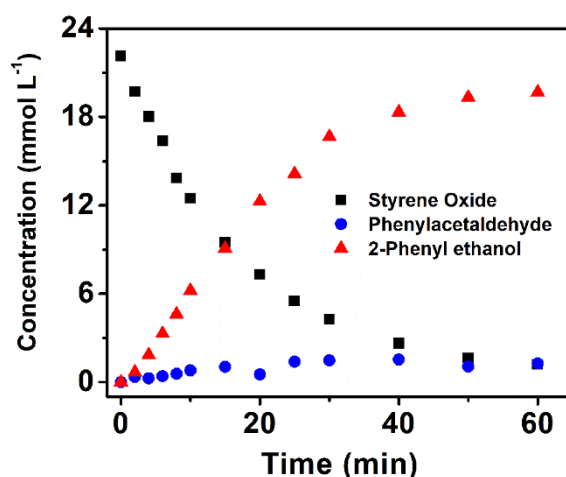


**Figure 5.9** – Pd/Fe<sub>2</sub>O<sub>3</sub> BTT sample employed in the hydrogenation of styrene oxide under 6 bar of hydrogen pressure as a comparison for the 1 bar test. Here we can verify that the reaction went faster than the one at lower pressure, and the selectivity towards 2-phenyl ethanol was higher.

It is worth mentioning that all samples were collected under nitrogen and the catalyst was immediately removed from the mixture after collection (through centrifugation and filtration), the sample was then diluted in acetone to the desired concentration range for injection in the chromatograph. To verify the conversion rates of phenylacetaldehyde onto 2-phenyl ethanol under the same conditions of reaction, we repeated the experiments exchanging styrene oxide by phenylacetaldehyde. Results can be seen in **Figure 5.10**. Through these graphs we can notice that the conversion of Phenylacetaldehyde onto 2-phenyl ethanol happens very slowly in both cases, producing a slightly higher concentration for the Pd/Fe<sub>2</sub>O<sub>3</sub> ATT sample (**Figure 5.10B**) than on Pd/Fe<sub>2</sub>O<sub>3</sub> BTT (**Figure 5.10A**). This could be explained once again by the cleaner surface, allowing more catalytic sites to efficiently hydrogenate the aldehyde to the alcohol product on the sample after thermal treatment. On the other hand, after 24 hours of reaction, we can see that the concentration of phenylacetaldehyde drops more intensely on the sample before thermal treatment, while this

is contradictory based on the explanation mentioned above, this catalyst must present different catalytic sites that are responsible for the side reactions that are occurring.

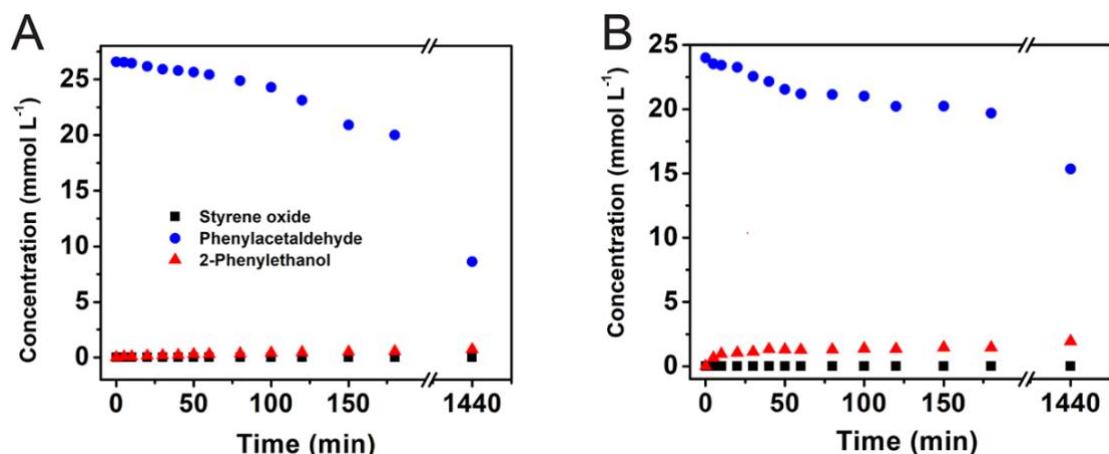


**Figure 5.10** – Kinetics Phenylacetaldehyde (blue spheres) hydrogenation to 2-Phenylethanol (red triangles) using the Pd/Fe<sub>2</sub>O<sub>3</sub> BTT (A) and Pd/Fe<sub>2</sub>O<sub>3</sub> ATT (B). Here, we can notice that while the Phenylacetaldehyde concentration suffers a significant decrease in the 24 hours of reaction, the 2-Phenylethanol is barely increased, indicating the formation of other side products.

Since phenylacetaldehyde is a highly unstable molecule and can be polymerized,<sup>27,28</sup> we maintained the reaction at 1 hour to minimize the generation of secondary products. (identified as Benzaldehyde, 2-phenylpropenal, and acetophenone on GC-MS)

To understand where these secondary products could be coming from, we decided to employ dry DMF as solvent ( $\approx 10$  ppm of water), which was also degassed through 3 cycles of freeze-drying and vacuum. The catalysts were placed in the reactor under argon flow, and the sample was removed inside a glovebox to avoid any contact with oxygen. The side products disappeared, and only phenylacetaldehyde, styrene oxide, and 2-phenyl ethanol could be seen, indicating that the low percentage of water present in the commercially available solvent played a role in the generation of side products. Next, we decided to study the reusability of our materials in the catalytic hydrogenation of styrene oxide. The catalysts were placed in the

reactor using the same conditions mentioned before, and after every reaction cycle, they were washed three times with acetone and dried under vacuum before use. Results can be seen in **Figure 5.11**.

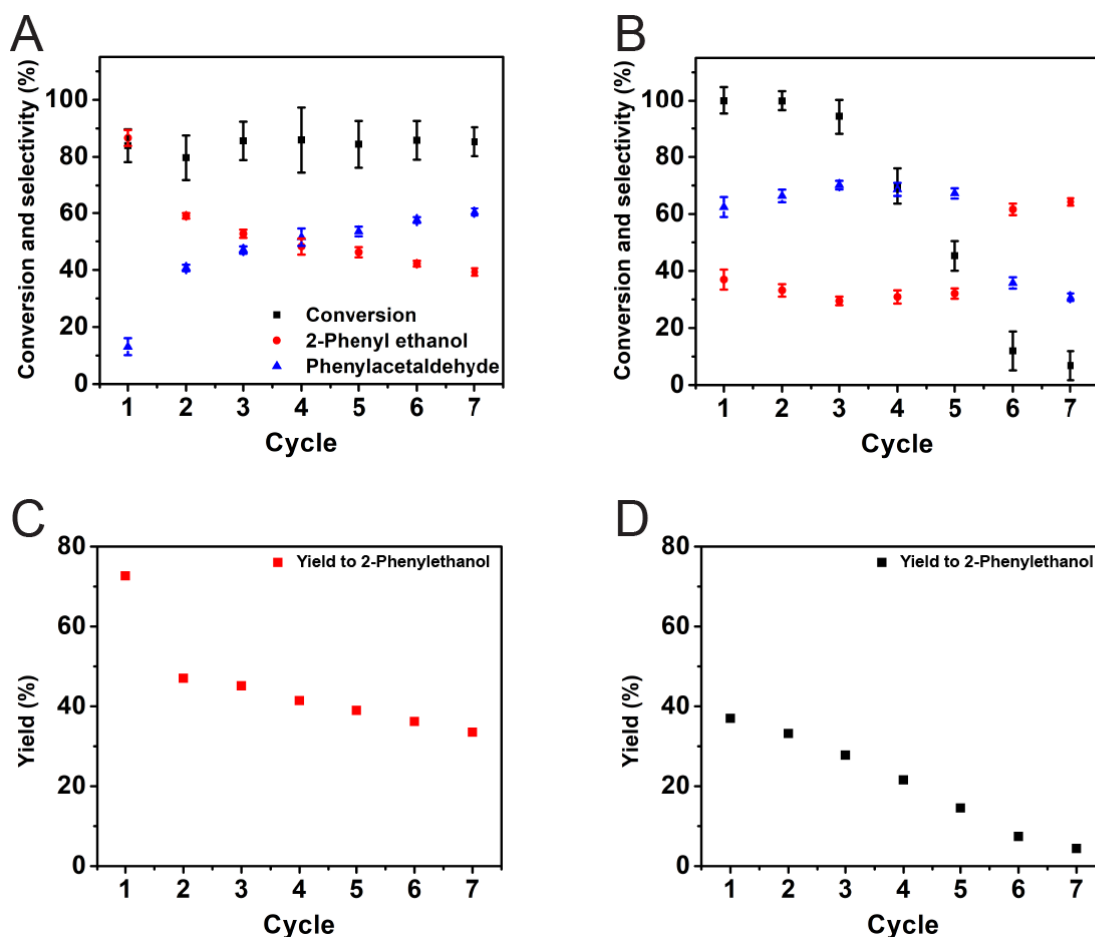


**Figure 5.11** – Recycling reactions of styrene oxide hydrogenation employing the synthesized Pd-decorated shape-controlled Fe<sub>2</sub>O<sub>3</sub>, as prepared (A), and after thermal treatment (B), and their respective yields for all seven cycles (C and D). Reactions were performed under 1 bar of hydrogen pressure in DMF, for 1 hour each, and the catalysts were removed and washed using acetone, dried under vacuum for 1 hour, and re-suspended.

For the Pd/Fe<sub>2</sub>O<sub>3</sub> BTT material, **Figure 5.11A**, the reaction presented a relatively constant conversion even after seven cycles, although, the selectivity suffered an apparent inversion after the third cycle. This indicates changes on the surface of the catalyst that could be related to 1) aggregation of NPs or 2) removal of organic matter during the

washing/reaction cycles. **Figure 5.11B** shows the Pd/Fe<sub>2</sub>O<sub>3</sub> ATT material under recycling. As it can be seen, the conversion drops after the third cycle, indicating either that the Pd NPs are being removed during the procedure, or that they are aggregating even further. The selectivity of this material also displayed an inversion after the sixth cycle, which could also be due to structural changes in catalytic sites. When plotting both cases in terms of 2-phenyl ethanol yield percentage, **Figure 5.11C** (Pd/Fe<sub>2</sub>O<sub>3</sub> BTT), and **Figure 5.11D** (Pd/Fe<sub>2</sub>O<sub>3</sub> ATT), the profile shows that the yield lowers drastically after the first cycle on the catalyst before thermal treatment, getting to a value that is close to the material without any PVP on the surface. This could indicate that recycling the catalyst removed the stabilizer that was blocking some catalytic sites and managing the selectivity of this catalyst.

To observe the catalyst after one cycle of reaction, we employed TEM, **Figure 5.12**. Here, we can see that the NPs on the material before thermal treatment, **Figure 5.12A**, already suffered a drastic change from the material before the reaction. While the NPs still present the rounder characteristics, seemingly formed by smaller particles, they already grew in size, measuring  $61.7 \pm 3.3$  nm in diameter, which is about twice the size of the initial particles. On the other hand, the material after thermal treatment did not present a clear difference after one cycle, with particles measuring  $58.5 \pm 1.7$  nm in diameter, which is similar to the initial value. To compare with a benchmark material, we employed the commercially available 20% wt. Pd/C with a molar ratio of 60 (Pd/Styrene oxide). After one hour of reaction, the commercial catalyst showed a conversion of 100% with a selectivity of 63.9% towards 2-phenyl ethanol, indicating that even though the conversion was high, the selectivity was lower than our materials.

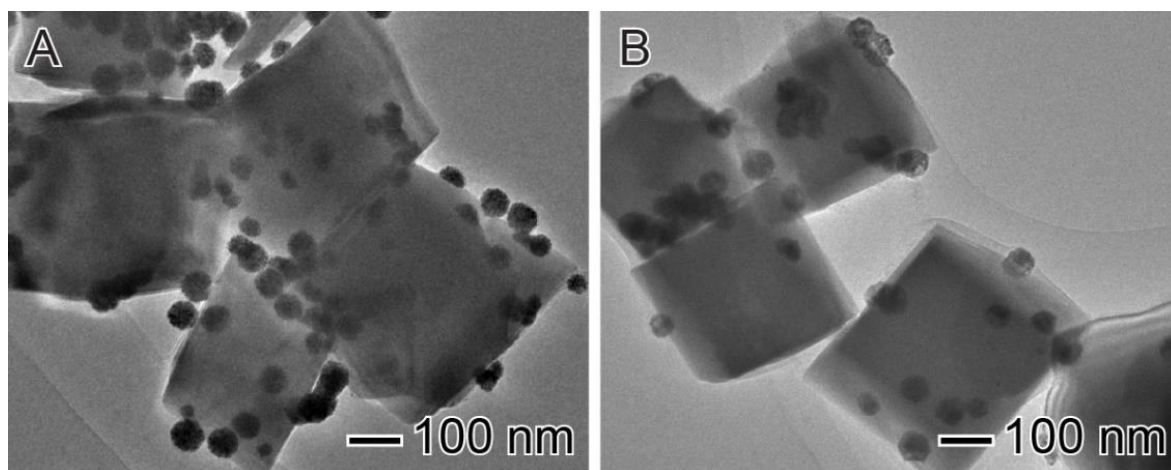


**Figure 5.12** – Pd/Fe<sub>2</sub>O<sub>3</sub> samples before thermal treatment (A), and after thermal treatment (B), after employed in the hydrogenation of styrene oxide. The particles are seen as more aggregated in both cases, yet for the sample without thermal treatment, we can notice a significant growth on their size.

Pre-treatment tests were performed on Pd/Fe<sub>2</sub>O<sub>3</sub> BTT to verify if by reducing any oxidized Pd would cause an enhancement on the reaction conversion or selectivity. For this, we pressurized the reactor with 1 bar of hydrogen for 14 hours without adding styrene oxide and degassed the solvent with nitrogen and ultrasound to remove any dissolved hydrogen before starting the reaction. These treatments were performed both at 30°C and 50°C. Results can be seen in **Table 5.2**.

**Table 5.2** – Effect of pretreating the sample with hydrogen for 14 hours before performing the reaction.

<b>Treatment Temperature</b>	<b>Conversion</b>	<b>Phenylacetaldehyde</b>	<b>2-Phenyl ethanol</b>
<b>30 °C</b>	75.6%	12.2%	87.8%
<b>50 °C</b>	91.5%	2.2%	98.8%

These results show that the oxidized Pd species on the surface of our catalyst were responsible for lowering the selectivity towards 2-phenyl ethanol, and since

phenylacetaldehyde is known to be formed in the presence of a Lewis acid, this is expected to happen in the presence of a  $\text{Pd}_{x+}$  species. These samples were analyzed by XPS, though, due to some errors, we cannot display these results at the moment.

To understand whether the selectivity of our catalyst towards 2-phenyl ethanol was due to the support, we also synthesized a Pd/C material through the same method used for Pd/Fe<sub>2</sub>O<sub>3</sub> BTT, substituting the Fe<sub>2</sub>O<sub>3</sub> by Vulcan Carbon. The product can be seen in **Figure 5.13**. This material presented smaller Pd particles as in our materials, which could be attributed to the higher surface area of the carbon support, yet a lot of NPs were not successfully deposited onto the carbon support.

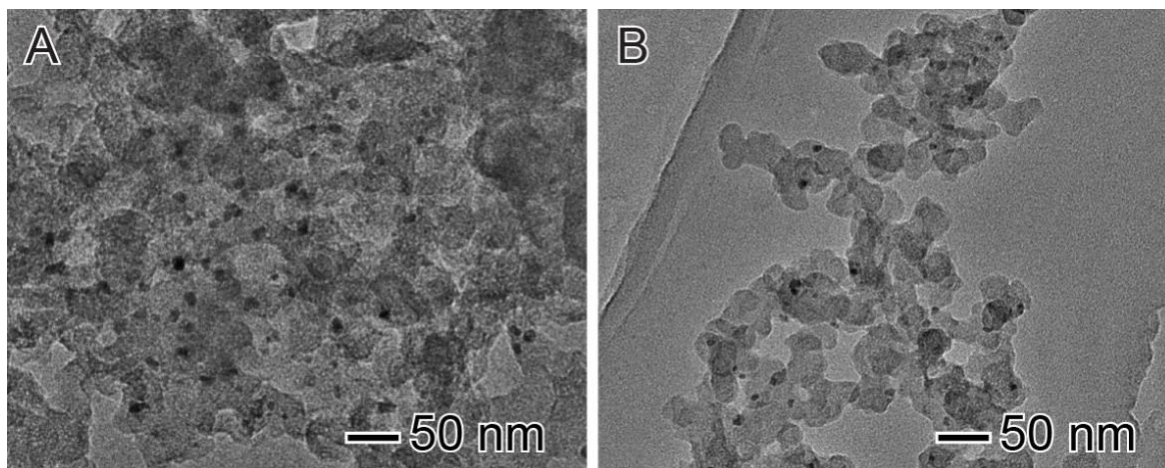


**Figure 5.13** – Pd/C samples synthesized employing the same method as for the Pd/Fe<sub>2</sub>O<sub>3</sub> method (A), and the same material after styrene oxide hydrogenation. This sample was prepared to verify the effect of Fe<sub>2</sub>O<sub>3</sub> onto the reaction in question.

The NPs range from  $11.5 \pm 1.7$  nm and are well distributed on the support with 1.27 wt.% of Pd. After 1 hour of reaction employing this nanomaterial at a 60 molar ratio (Pd/Styrene Oxide), the conversion achieved 100% with a selectivity of 95.3% to 2-phenyl ethanol, and at a 180 molar ratio (Pd/Styrene Oxide), it reached a 45.2% conversion with a selectivity of 96.8% to 2-phenyl ethanol. It indicates that our method produces NPs with high selectivity to the less substituted alcohol. Although this method granted smaller particles and higher activity, when the material was centrifuged and separated from the mixture, a lot of

NPs were still present in the liquid phase. This could also be seen on TEM, **Figure 5.13B**, the material has fewer NPs, and they were not as easily found. To confirm that, we employed FAAS on the catalyst after reaction, which displayed a loss of 44.3 wt.% of Pd.

Our last experiment was performed to verify whether our catalyst was active due to complexes that were formed if Pd was dissolved during the reaction. This experiment is based on adding mercury to the system while the reaction is happening, Hg<sub>0</sub> forms an amalgam with Pd,<sup>34</sup> hindering its activity. All results can be seen in **Table 5.3**. Initially (entry 1), we tested only PdCl<sub>4</sub><sup>2-</sup> as the catalyst, with a 60 molar ratio (Pd/styrene oxide), while the reaction was happening the solution changed color to black, indicating that Pd was reduced, which was probably the reason for its high activity.

**Table 5.3** – Tests performed to explore the Pd precursor as the catalyst and poisoning with mercury.

Entry	Catalyst	Additive	Conversion	Selectivity to 2-Phenyl Ethanol
1	PdCl <sub>4</sub> <sup>2-</sup>	-	99.9%	38.3%
2	PdCl <sub>4</sub> <sup>2-</sup>	Fe <sub>2</sub> O <sub>3</sub>	85.8%	35.8%
3	PdCl <sub>4</sub> <sup>2-</sup>	Hg <sub>0</sub>	1.7%	26.5%
4	PdCl <sub>4</sub> <sup>2-</sup>	Fe <sub>2</sub> O <sub>3</sub> + Hg <sub>0</sub>	1.5%	20.1%
5	Pd/Fe <sub>2</sub> O <sub>3</sub>	Hg <sub>0</sub>	3.9%	69.9%
6	Pd/Fe <sub>2</sub> O <sub>3</sub>	Hg <sub>0</sub> added after 30 min	t <sub>30</sub> = 64.5% t <sub>60</sub> = 65.2%	t <sub>30</sub> = 85.3% t <sub>60</sub> = 85.6%

As a second test (entry 2) we performed the same reaction in the presence of Fe<sub>2</sub>O<sub>3</sub> to verify whether the support played any roles in this system, our conversion was lower than in the absence of support, indicating that the Pd<sub>0</sub> could have been reduced on top of the Fe<sub>2</sub>O<sub>3</sub>, which lowered the surface area, compared to the first sample. After that, we performed the same reactions in the presence of mercury (Entries 3 and 4), to verify whether the catalyst was the complex species or the metallic one. In both cases the conversion was very low, indicating that the metallic species was responsible for the conversion. Lastly, we performed the reaction



using our Pd/Fe<sub>2</sub>O<sub>3</sub> BTT catalyst in the presence of mercury (Entries 5 and 6), and also tested the same reaction by adding mercury after 30 minutes, and results showed that after the addition of mercury, the reaction stops, which further indicates that Pd<sup>0</sup> is responsible for the reaction.

## 5.4 – Conclusions

We described in this chapter the successful synthesis of a catalyst based on Pd NPs and iron oxide in the hematite phase, with high activity and selectivity towards 2-phenyl ethanol. Our catalyst under 6 bar of pressure and 30°C converted 94.6% styrene oxide with 1.7 mol% of catalyst to the selectivity of 94.0%. This selectivity was investigated and attributed to the blockage of some catalytic sites on the NPs that were responsible for the isomerization of the reagent. To show this, we calcined the sample under air to remove organic matter from its surface, and we were able to obtain materials with a cleaner surface producing a lower selectivity towards the desired product. Recycling the catalyst also caused a lower selectivity, which led us to believe that the stabilizers were removed during the reaction, and we could also see an evident growth on the nanoparticle sizes after recycling. Such results show us that stabilizers may have a beneficial role towards a higher selectivity, as long as they stay on the surface of the catalyst throughout the process.

## 5.5 – References

- 1 Dabbawala AA, Sudheesh N, Bajaj HC. Palladium supported on chitosan as a recyclable and selective catalyst for the synthesis of 2-phenyl ethanol. *Dalt Trans* 2012; **41**: 2910.
- 2 Sasu A, Dragoi B, Ungureanu A, Royer S, Dumitriu E, Hulea V. Selective conversion of styrene oxide to 2-phenylethanol in cascade reactions over non-noble metal catalysts. *Catal Sci Technol* 2016; **6**: 468–478.
- 3 Chandalia SB. Synthesis of Phenethyl Alcohol by Catalytic Hydrogenation of Styrene Oxide. *Org Process Res Dev* 1998; **2**: 294–297.
- 4 Kirm I, Medina F, Sueiras JE, Salagre P, Cesteros Y. Hydrogenation of styrene oxide in the presence of supported platinum catalysts to produce 2-phenylethanol. *J Mol Catal A Chem* 2007; **261**: 98–103.
- 5 Zaccheria F, Psaro R, Ravasio N, Sordelli L, Santoro F. Mono and Bifunctional Catalysts for Styrene Oxide Isomerization or Hydrogenation. *Catal Letters* 2011; **141**: 587–591.
- 6 Lim B, Jiang M, Tao J, Camargo PHC, Zhu Y, Xia Y. Shape-Controlled Synthesis of Pd Nanocrystals in Aqueous Solutions. *Adv Funct Mater* 2009; **19**: 189–200.
- 7 Kirm I, Medina F, Rodríguez X, Cesteros Y, Salagre P, Sueiras JE. Preparation of 2-phenylethanol by catalytic selective hydrogenation of styrene oxide using palladium catalysts. *J Mol Catal A Chem* 2005; **239**: 215–221.
- 8 Nougima A, Mitsudome T, Mizugaki T, Jitsukawa K, Kaneda K. Selective Deoxygenation of Epoxides to Alkenes with Molecular Hydrogen Using a Hydrotalcite-Supported Gold Catalyst: A Concerted Effect between Gold Nanoparticles and Basic Sites on a Support. *Angew Chemie Int Ed* 2011; **50**: 2986–2989.

- 9 Costa V V, Kelly A, Rocha S, Kozhevnikov I V, Gusevskaya E V. Isomerization of styrene oxide to phenylacetaldehyde over supported phosphotungstic heteropoly acid. *Appl Catal A Gen* 2010; **383**: 217–220.
- 10 Rode CV, Nehete UN, Dongare MK. Alkali promoted selective epoxidation of styrene to styrene oxide using TS-1 catalyst. *Catal Commun* 2003; **4**: 365–369.
- 11 Ouyang J, Pei J, Kuang Q, Xie Z, Zheng L. Supersaturation-Controlled Shape Evolution of  $\alpha$ -Fe<sub>2</sub>O<sub>3</sub> Nanocrystals and Their Facet-Dependent Catalytic and Sensing Properties. *ACS Appl Mater Interfaces* 2014; **6**: 12505–12514.
- 12 Gao F, Liu R, Yin J, Lu Q. Synthesis of polyhedral iron oxide nanocrystals bound by high-index facets. *Sci China Chem* 2014; **57**: 114–121.
- 13 Barbosa ECM, Fiorio JL, Mou T, Wang B, Rossi LM, Camargo PHC. Reaction Pathway Dependence in Plasmonic Catalysis: Hydrogenation as a Model Molecular Transformation. *Chem - A Eur J* 2018. doi:10.1002/chem.201705749.
- 14 Yao C, Dahmen T, Gansäuer A, Norton J. Anti-Markovnikov alcohols via epoxide hydrogenation through cooperative catalysis. *Science (80- )* 2019; **364**: 764–767.
- 15 Patra AK, Kundu SK, Bhaumik A, Kim D. Morphology evolution of single-crystalline hematite nanocrystals: magnetically recoverable nanocatalysts for enhanced facet-driven photoredox activity. *Nanoscale* 2016; **8**: 365–377.
- 16 Ahmmad B, Leonard K, Shariful Islam M, Kurawaki J, Muruganandham M, Ohkubo T *et al.* Green synthesis of mesoporous hematite ( $\alpha$ -Fe<sub>2</sub>O<sub>3</sub>) nanoparticles and their photocatalytic activity. *Adv Powder Technol* 2013; **24**: 160–167.
- 17 Jubb AM, Allen HC. Vibrational Spectroscopic Characterization of Hematite, Maghemite, and Magnetite Thin Films Produced by Vapor Deposition. *ACS Appl Mater Interfaces* 2010; **2**: 2804–2812.
- 18 Monzö J, Koper MTM, Rodriguez P. Removing polyvinylpyrrolidone from catalytic Pt

- nanoparticles without modification of superficial order. *ChemPhysChem* 2012; **13**: 709–715.
- 19 Ansar SM, Ameer FS, Hu W, Zou S, Pittman CU, Zhang D *et al.* Removal of molecular adsorbates on gold nanoparticles using sodium borohydride in water. *Nano Lett* 2013; **13**: 1–11.
  - 20 Crespo-Quesada M, Andanson JM, Yarulin A, Lim B, Xia Y, Kiwi-Minsker L. UV-ozone cleaning of supported poly(vinylpyrrolidone)-stabilized palladium nanocubes: Effect of stabilizer removal on morphology and catalytic behavior. *Langmuir* 2011; **27**: 7909–7916.
  - 21 Cannas C, Ardu A, Musinu A, Peddis D, Piccaluga G. Spherical Nanoporous Assemblies of Iso-Oriented Cobalt Ferrite Nanoparticles: Synthesis, Microstructure, and Magnetic Properties. *Chem Mater* 2008; **20**: 6364–6371.
  - 22 Lupan O, Postica V, Hoppe M, Wolff N, Polonskyi O, Pauporté T *et al.* PdO/PdO<sub>2</sub> functionalized ZnO : Pd films for lower operating temperature H<sub>2</sub> gas sensing. *Nanoscale* 2018; **10**: 14107–14127.
  - 23 Su W-B, Chen W-R, Chang J-R. Impact of Iron Deposition on Pd/ $\delta$ -Al<sub>2</sub>O<sub>3</sub> in Selective Hydrogenation of Pyrolysis Gasoline. *Ind Eng Chem Res* 2000; **39**: 4063–4069.
  - 24 Hensley AJR, Hong Y, Zhang R, Zhang H, Sun J, Wang Y *et al.* Enhanced Fe<sub>2</sub>O<sub>3</sub> Reducibility via Surface Modification with Pd: Characterizing the Synergy within Pd/Fe Catalysts for Hydrodeoxygenation Reactions. *ACS Catal* 2014; **4**: 3381–3392.
  - 25 Wang L, Pu C, Xu L, Cai Y, Guo Y, Guo Y *et al.* Effect of supports over Pd/Fe<sub>2</sub>O<sub>3</sub> on CO oxidation at low temperature. *Fuel Process Technol* 2017; **160**: 152–157.
  - 26 Duan H, Xu D, Li W, Xu H. Study of the Redox Properties of Noble Metal/Co<sub>3</sub>O<sub>4</sub> by Electrical Conductivity Measurements. *Catal Letters* 2008; **124**: 318–323.

- 27 Erickson JLE, Grammer GN. The Spontaneous Polymerization of Phenylacetaldehyde. *J Am Chem Soc* 1958; **80**: 5466–5469.
- 28 Cataldo F. A new method of synthesizing polyphenylacetylene. *Polym Int* 1996; **39**: 91–99.
- 29 Zhang XF, Yao J, Yang X. Isomerization of Styrene Oxide to Phenyl Acetaldehyde over Different Modified Beta Zeolites. *Catal Letters* 2017; **147**: 1523–1532.
- 30 Vyas DJ, Larionov E, Besnard C, Guénée L, Mazet C. Isomerization of Terminal Epoxides by a [Pd–H] Catalyst: A Combined Experimental and Theoretical Mechanistic Study. *J Am Chem Soc* 2013; **135**: 6177–6183.
- 31 Kominami H, Yamamoto S, Imamura K, Tanaka A, Hashimoto K, Corey EJ *et al.* Photocatalytic chemoselective reduction of epoxides to alkenes along with formation of ketones in alcoholic suspensions of silver-loaded titanium(iv) oxide at room temperature without the use of reducing gases. *Chem Commun* 2014; **50**: 4558.
- 32 Mitsudome T, Urayama T, Yamazaki K, Maehara Y, Yamasaki J, Gohara K *et al.* Design of Core-Pd/Shell-Ag Nanocomposite Catalyst for Selective Semihydrogenation of Alkynes. *ACS Catal* 2016; **6**: 666–670.
- 33 Yadav GD, Lawate YS. Hydrogenation of Styrene Oxide to 2 - Phenyl Ethanol over Polyurea Microencapsulated Mono- and Bimetallic Nanocatalysts : Activity , Selectivity , and Kinetic Modeling. *Ind Eng Chem Res* 2013; **52**: 4027–4039.
- 34 Hagen CM, Widegren JA, Maitlis PM, Finke RG. Is It Homogeneous or Heterogeneous Catalysis? Compelling Evidence for Both Types of Catalysts Derived from [Rh( $\eta^5$ -C<sub>5</sub>Me<sub>5</sub>)Cl<sub>2</sub>]<sub>2</sub> as a Function of Temperature and Hydrogen Pressure. *J Am Chem Soc* 2005; **127**: 4423–4432.

## **Section 3 – Conclusions and perspectives**

## Chapter 6 – Final remarks

This dissertation showed three different materials with similarities when it comes to their overall composition: presenting noble metal NPs as active phases supported on semiconductors. While in Au/TiO<sub>2</sub> it was demonstrated that the reaction pathway was dependent on the nature of the reducing agent, the control over Pt coverage and metal-support interactions was fundamental to optimize performances in Pt/TiO<sub>2</sub>. Interestingly, we observed that the selectivity of a hydrogenation reaction over Pd/Fe<sub>2</sub>O<sub>3</sub> was strongly dependent on the presence of surfactants at the NPs surface. The results clearly demonstrate the use of controlled NPs is important to establish structure-performance relationships in nanocatalysis and also optimize performances and selectivities. We believe that the results describe herein may inspire the development of catalysts towards hydrogenation reactions.

As for perspectives, this field has several factors to be explored to understand the chemistry and physics of nanomaterials, from *in-situ* studies to *operando* reactions, these techniques tend to give numerous insights into the improvement of catalyst design. For plasmonic nanomaterials, it is a fairly new area that needs a lot of development to a better understanding of their role in the activity and selectivity of catalytic reactions. Most results show evidences of charge transfer phenomena in plasmonic catalysis combined with theoretical studies, although proving the mechanism is a hard task that is still under thorough research.

As for the oxygen reduction reaction, one of the most important reactions for fuel-cell applications, the development of materials of lower cost than platinum is a field that has been and that will still be thoroughly researched for years since green energy production brings great benefits to the environment. And since surface groups can cause a significant change in the activity of the catalyst, the next step would be to vary the surfactants to insert different

groups to verify whether this activity could be further enhanced. These materials could also be employed in *in situ* studies for a mechanistic verification that supports our hypothesis.

Finally, catalytic reactions employing shape-controlled materials have allowed us to make a clearer correlation between structure and activity of materials. In nanocatalysis, these nanomaterials tend to be employed in several reactions to improve factors such as the nanomaterial's stability, its reactivity, adsorption properties, and especially to understand the relationship between surface, crystal structure, electronic structure, and activity. On the other hand, maintaining surface groups during the reaction is still a task that needs further work. Our material presented a better selectivity at a low pressure and temperature, however, as soon as the surfactant leaves the surface, the nanoparticles suffer aggregation. In order to improve these materials, a systematic study has to be performed to maintain the capping agents on the surface, while not hindering their activities.



## **Academic curriculum vitae**

### **PERSONAL INFORMATION**

Name: Eduardo Cesar Melo Barbosa

Place and date of birth: Engenheiro Beltrão – Paraná – Brazil – 07/01/1992

### **1) EDUCATION BACKGROUND**

#### **Visiting Ph.D. in Inorganic Chemistry (2018 – 2019)**

Inorganic Chemistry Laboratory, University of Oxford, Oxford, United Kingdom

Advisor in the United Kingdom: Prof. Dr. Shik Chi Edman Tsang

Advisor in Brazil: Prof. Dr. Pedro Henrique Cury Camargo

Project: Shape-controlled TiO<sub>2</sub> materials decorated with metal nanoparticles: structure-performance relationships and mechanistic investigations towards the CO<sub>2</sub> hydrogenation reaction. Grant #2018/00393-6, Sao Paulo Research Foundation (FAPESP).

#### **Ph.D. in Chemistry (2015 - 2019)**

Department of Chemistry, Universidade de São Paulo, São Paulo, Brazil

Advisor: Prof. Dr. Pedro Henrique Cury Camargo

Thesis: Hybrid materials composed of oxides and metallic nanoparticles for catalytic and photocatalytic applications. Grant #2015/11452-5, Sao Paulo Research Foundation (FAPESP).

#### **B.S. in Chemistry (2012 - 2013)**

Department of Chemistry, Clark University, Worcester, MA – USA

Advisor: Prof. Dr. Sergio Granados-Focil

Science without Borders Program, sponsored by Institute of International Education (IIE) and the Government of Brazil – Coordination for the Improvement of Higher Level Personnel (CAPES).

**B.S. in Chemistry (2010 - 2014) with technological chemistry attribution**

Department of Chemistry, Universidade Estadual de Londrina, Londrina, PR – Brazil

Advisor: Prof. Dr. Luiz Henrique Dall’Antonia

Dissertation: Synthesis, application and photoelectrocatalytic properties of hematite thin films.

**Hudson High School (2008 - 2009)**

Completed a year as an exchange student, Hudson, OH – USA

**2) PROFESSIONAL EXPERIENCE**

**Visiting Ph.D. period in CO<sub>2</sub> hydrogenation advised by Professor Dr. Shik Chi Edman Tsang – Wolfson Catalysis Centre, Oxford, Oxfordshire, United Kingdom – June 2018 to August 2019**

During this year we conducted a research on the catalytic activity of different metals on the hydrogenation of carbon dioxide through heterogeneous catalysis. This research is directly related to our research project in Brazil and counted as a part of my Ph.D. thesis. Our main focus was to understand the effects of different conditions onto the hydrogenation of CO<sub>2</sub> using the same Pd/Fe<sub>2</sub>O<sub>3</sub> catalyst.

**Ph.D. in nanomaterials design advised by Professor Dr. Pedro Henrique Cury Camargo**  
**– Group for Advancing in Nanomaterial Design (GrAND), São Paulo, São Paulo, Brazil**  
**– February 2015 to October 2019**

Our research focused on designing nanomaterials with controlled shape, morphology, and composition for desired photocatalytic and electrocatalytic applications, with emphasis on the characterization and application towards different reactions, through green, environmentally friendly routes. Several materials have been synthesized, such as shape controlled Au/TiO<sub>2</sub>, Pt/TiO<sub>2</sub>, Pd/TiO<sub>2</sub>, Pt/Fe<sub>2</sub>O<sub>3</sub>, Pd/Fe<sub>2</sub>O<sub>3</sub>, aside from Ag, Au, Pd and Pt nanoparticles with different morphologies.

**Supervised research in electrochemistry/materials laboratory advised by Professor Dr. Luiz Henrique Dall’Antonia – Electrochemistry and materials laboratory (LEMA), Londrina, Paraná, Brazil – September 2013 to February 2015**

During this time, our study focused on the development of Fe<sub>2</sub>O<sub>3</sub> (hematite) electrodes for photoelectrocatalytic applications, studying their electrochemical, photoelectrochemical and morphological properties.

**Custom Solutions Engineer intern / Chemistry intern – Swagelok, Solon, Ohio, USA – May 2013 to July 2013**

This short-term internship was based on testing properties of tube fittings, tubes, lubricants, leak detectors, as well as on the development of methods for treating their residual waste. Another task developed during this period was the translation of their standard work to Portuguese for their unit in Brazil.

**Supervised research in polymer science advised by Professor Dr. Sergio Granados-Focil – Clark University, Worcester, MA – August 2012 to May 2013**

This directed study based on the synthesis of monomers of brominated aromatic compounds in order to produce conductive polymers, all characterizations were done via  $^1\text{H}$  NMR and the syntheses of the monomers were optimized during that period.

**Supervised research in environmental/atmospheric chemistry laboratory with Professor Dr. Maria Cristina Solci – Atmospheric Compounds Analysis Laboratory (LACA) – Londrina, Paraná, Brazil – September 2011 to August 2012**

Study based on Stir Bar Sorption Extraction (SBSE) of the aromatic compound phenanthrene from aqueous solutions, aiming at water purification, all analyses were done by UV-Vis Spectroscopy.

### **3) SCIENTIFIC RESULTS**

1. **Barbosa, E. C. M.**; Fiorio, J. L.; Mou, T.; Wang, B.; Rossi, L. M.; Camargo, P. H. C.. Reaction Pathway Dependence in Plasmonic Catalysis: Hydrogenation as a Model Molecular Transformation. *Chem. Eur. J.* **2018**. 24. 12330. Chosen by the reviewers as a *HOT PAPER* (among the 10% best papers in that issue), and also earned a Poster Prize awarded by the journal “*Catalysis Science & Technology*” from the Royal Society of Chemistry at the international GOLD 2018 conference in Paris, France.
2. Scremin, J.; **Barbosa, E. C. M.**; Salamanca-Neto, C. A. R.; Camargo, P. H. C.; Sartori, E. R. Design of a sensing platform based on  $\text{TiO}_2$ -Au NPs integrated with carbon nanotubes for the amperometric determination of ascorbic acid. *Microchim Acta*. **2018**. 185: 251.

3. Teixeira, I.; **Barbosa, E. C. M.**; Tsang, S. C. E.; Camargo, P. H. C.; Carbon Nitrides and Metal Nanoparticles: From Controlled Synthesis to Design Principles for Improved Photocatalysis. *Chem. Soc. Rev.* **2018**, *47*, 7783-7817.
4. Wang, J.; **Barbosa, E. C. M.**; Parussulo, A. L. A.; Reis, F. L. E.; Ando, R. A.; Araki, K.; Toma, H. E.; Camargo, P. H. C.. On the Effect of TiO<sub>2</sub> Nanocrystallites over the Plasmonic Photodegradation by Au Nanoparticles. *J Raman Spectrosc.* **2018**, *49*, 1953–1960.
5. Quiroz, J.; **Barbosa, E. C. M.**; Araujo, T. P.; Fiorio, J. L.; Wang, Y.; Zou, Y.; Mou, T.; Alves, T. V.; de Oliveira, D. C.; Wang, B.; Haigh, S. J.; Rossi, L. M.; Camargo, P. H. C. Controlling Reaction Selectivity over Hybrid Plasmonic Nanocatalysts. *Nano Letters*, **2018**, *18*, 7289.
6. Araújo, T. P.; Quiroz, J.; **Barbosa, E. C. M.**; Camargo, P. H. C.. Understanding Plasmonic Catalysis with Controlled Nanomaterials based on Catalytic and Plasmonic Metals. *Current Opinion in Colloid & Interface Science*. **2019**, *39*, 110.
7. Mattos, G.; Moraes, J. T.; **Barbosa, E. C. M.**; Dekker, R.; Camargo, P.H.C.; Dekker, A. M. B.; Sartori, E. R.. Laccase stabilized on  $\beta$ -D-glucan film on the surface of carbon black/gold nanomaterials: A new platform for electrochemical biosensing. *Bioelectrochemistry*. **2019**, *129*, 116.
8. Saire-Saire, S.; **Barbosa, E. C. M.**; Garcia, D.; Andrade, L. H.; Garcia-Segura, S.; Camargo, P. H. C.; Alarcon, H. Green synthesis of Au decorated CoFe<sub>2</sub>O<sub>4</sub> nanoparticles for

catalytic reduction of 4-nitrophenol and dimethylphenylsilane oxidation. *RSC Advances*, **2019**, 9, 22116.

9. **Barbosa, E. C. M.**; Parreira, L. S.; de Freitas, I. C.; Aveiro, L. R.; de Oliveira, D. C.; dos Santos, M. C.; Camargo, P. H. C.. Pt-Decorated TiO<sub>2</sub> Materials Supported on Carbon: Increasing Activities and Stabilities toward the ORR by Tuning the Pt Loading. *ACS Appl. Energy Mater*; **2019**, 2, 5759-5768.

10. Freitas, I. C.; Parreira, L. S.; **Barbosa, E. C. M.**; Novaes, B. A.; Mou, T.; Alves, T. V.; Quiroz, J.; Thomas, A.; Wang, B.; Haigh, S.; Camargo, P. H.C. Addressing the oxygen evolution reaction with plasmonic electrocatalysis. Submitted.

11. Salamanca-Neto, C. A. R.; Marcheafave, G. G.; Scremin, J.; **Barbosa, E. C. M.**; Camargo, P. H. C.; Dekker, R. F. H.; Scarmínio, I. S.; Barbosa, A. M.; Sartori, E. R. Application of design of experiments in a biosensor device manufacturing to the determination of chlorogenic acid content in brewed coffee beverages for quality control. Submitted.

12. Fiorio, J. L.; Araújo, T. P.; **Barbosa, E. C. M.**; Quiroz, J.; Rudolph, M.; Hashmi, A. S. K.; Camargo, P. H. C.; Rossi, L. M. Bio-renewable formic acid as a hydrogen source in selective reduction reactions over heterogeneous gold catalyst. Submitted.

13. Fiorio, J. L.; **Barbosa, E. C. M.**; Kikuchi, D. K.; Lopez, N.; Camargo, P. H. C.; Rossi, L. M. Capping ligands effect in the formation of surface frustrated Lewis pairs. Submitted.

14. **Barbosa, E. C. M.**; Wang, J.; Parussulo, A. L. A.; Reis, F. L. E.; Ando, R. A.; Araki, K.; Toma, H. E.; Camargo, P. H. C.. On the effect of TiO<sub>2</sub> over the SPR-mediated photodegradation of methylene blue by Au nanoparticles under visible light. Oral presentation In: European Materials Research Society Fall Meeting – E-MRS, 2016, Warsaw, Poland.
15. Scremin, J.; **Barbosa, E. C. M.**; Salamanca-Neto, C. A. R.; Moraes, J. T.; Camargo, P. H. C.; Sartori, E. R. Desenvolvimento de sensor eletroquímico empregando material híbrido TiO<sub>2</sub>-NPsAu e nanotubos de carbono. Poster presentation In: XXI Simpósio Brasileiro de Eletroquímica e Eletroanalítica, 2017, Natal, Brazil.
16. Parreira, L. S.; **Barbosa, E. C. M.**; de Freitas, I. C.; Reis, F. E.; Aveiro, L. R.; de Oliveira, D. C.; dos Santos, M. C.; Camargo, P. H. C. Eletrocatalisadores TiO<sub>2</sub>-Pt/C para Reações de Conversão de Energia. Poster presentation In: Marco Inicial da SBEE, 2017. São Bernardo do Campo, Brazil.
17. Freitas, I. G.; **Barbosa, E. C. M.**; Camargo, P. H. C.. Catalytic activity of shape-controlled iron (III) oxide decorated with Pd and Pt nanoparticles. Poster presentation In: 46th World Chemistry Congress, 40a Reunião Anual da Sociedade Brasileira de Química, and IUPAC 49th General Assembly, 2017, São Paulo, Brazil.
18. Scremin, J.; **Barbosa, E. C. M.**; Salamanca-Neto, C. A. R.; Moraes, J. T.; Camargo, P. H. C.; Sartori, E. R. Evaluation of TiO<sub>2</sub> colloidal spheres decorated with Au nanoparticles for ascorbic acid determination. Poster presentation In: 46th World Chemistry Congress, 40a Reunião Anual da Sociedade Brasileira de Química, and IUPAC 49th General Assembly, 2017, São Paulo, Brazil.

19. **Barbosa, E. C. M.**; Parreira, L. S.; de Freitas, I. C.; Reis, F. E.; Aveiro, L. R.; dos Santos, M. C.; Camargo, P. H. C. Pt decorated TiO<sub>2</sub> microspheres for oxygen reduction reaction. Poster presentation In: 46th World Chemistry Congress, 40a Reunião Anual da Sociedade Brasileira de Química, and IUPAC 49th General Assembly, 2017, São Paulo, Brazil.
20. Novaes, B. A.; de Freitas, I. C.; **Barbosa, E. C. M.**; Camargo, P. H. C. Water-based synthesis of Au-Ir nanodendrites by a co-reduction approach. Poster presentation In: 46th World Chemistry Congress, 40a Reunião Anual da Sociedade Brasileira de Química, and IUPAC 49th General Assembly, 2017, São Paulo, Brazil.
21. **Barbosa, E. C. M.**; Fiorio, J. L.; Mou, T.; Wang, B.; Rossi, L. M.; Camargo, P. H. C. Reaction Pathway Dependence in Plasmonic Catalysis: Hydrogenation as a Model Molecular Transformation. Poster presentation In: GOLD2018, 2018, Paris, France. Earned the best poster prize.
22. **Barbosa, E. C. M.**; Quiroz, J.; Camargo, P. H. C. Harvesting Gold Plasmonic Properties to Achieve Selective Hydrogenations Under Visible-Light in Au@AgPt Nanorattles. Oral presentation In: GOLD2018, 2018, Paris, France.
23. Mattos, G. J.; **Barbosa, E. C. M.**; Dekker, R.; Dekker, A. M. B.; Camargo, P. H. C.; Sartori, E. R. Electrochemical laccase-biosensor based on  $\alpha$ -Fe<sub>2</sub>O<sub>3</sub> decorated with palladium nanoparticles for the determination of rutin. Poster presentation In: 6th. Bioanalytical School, 2018, Londrina, Brazil.



## 5) TECHNOLOGICAL PRODUCTION

1. Sartori, E. R.; Mattos, G.; Moraes, J. T.; Dekker, A. M. B.; Camargo, P.H.C.; **Barbosa, E. C. M.**. Processo de construção de um eletrodo de trabalho, biossensor eletroquímico baseado em materiais nanoestruturados e *Botryosphaeria Rhodina*, arquitetura e aplicação. **Patent deposited in the INPI in Brazil.** 2019.

## 6) GRANT ACTIVITIES

1. Coordination for the improvement of higher level personnel (CAPES)  
“Science without Borders” Fellowship
2. Sao Paulo Research Foundation (FAPESP)  
Ph.D. grant  
Research Abroad Ph.D. grant

## 7) OTHER INFORMATION

- Participated in a Vibrational Spectroscopy Course - VIBROS III. São Paulo, Brazil. 2015.
- Participated in the 11th PTA School of electrochemistry. São Paulo, Brazil. 2016.